

Interaction of Light and Matter  
in Metal-Semiconductor Hybrid Nanostructures

**Dissertation**

zur Erlangung des akademischen Grades “Doctor rerum naturalium” (Dr. rer. nat.)

vorgelegt von

Dipl.-Ing. David Leipold  
geboren am 29.04.1983 in Erfurt

Technische Universität Ilmenau  
Fakultät für Mathematik und Naturwissenschaften  
Institut für Physik  
Fachgebiet Theoretische Physik I

Betreuer: Prof. Dr. Erich Runge

Datum der Einreichung: 04.12.2014

Datum der Verteidigung: 18.05.2015



# Contents

<b>1</b>	<b>Introduction</b>	<b>5</b>
1.1	Scope and Overview . . . . .	7
<b>2</b>	<b>Plasmons in arrays of symmetry-breaking nano-dots</b>	<b>9</b>
2.1	Introduction . . . . .	9
2.2	Experiment . . . . .	11
2.3	Modeling . . . . .	14
2.3.1	Methods . . . . .	14
2.3.2	Geometry . . . . .	16
2.4	Data collection and far-field decomposition . . . . .	17
2.5	Results . . . . .	20
<b>3</b>	<b>Plexcitons/Excimons: coupled SPP – Dye-exciton modes</b>	<b>27</b>
3.1	Experimental findings . . . . .	29
3.2	Theoretical modeling . . . . .	32
3.3	Results with alternative geometries . . . . .	37
<b>4</b>	<b>Localization of light</b>	<b>41</b>
4.1	Localization in wave physics . . . . .	41
4.1.1	Interference . . . . .	41
4.1.2	Focusing light: common and uncommon ways . . . . .	42
4.1.3	Examples of localization of classical waves . . . . .	44
4.2	Localization of light in ZnO nano-needle arrays . . . . .	48
4.3	Calculations . . . . .	52
4.3.1	Challenges . . . . .	54
4.3.2	2D Mode-Expansion . . . . .	57
4.3.3	Results . . . . .	60
4.4	3D FDTD calculations . . . . .	63
4.5	Results . . . . .	65
4.5.1	Dynamics . . . . .	69

4.6	Ultrafast dynamics of localized 2D light modes . . . . .	72
<b>5</b>	<b>Summary and Outlook</b>	<b>77</b>
	<b>Appendix</b>	<b>83</b>
<b>A</b>	<b>Derivations</b>	<b>83</b>
A.1	Effective Permittivity for Nano-Needle – Vacuum Mixtures . . . . .	83
A.2	Intensity Distributions . . . . .	84
A.3	Surface Plasmon Polaritons . . . . .	86
A.3.1	Basics . . . . .	86
A.3.2	Excitation of SPPs with gratings . . . . .	89
<b>B</b>	<b>Bibliography</b>	<b>90</b>
B.1	References - own publications . . . . .	90
B.2	References - other publications . . . . .	91
<b>C</b>	<b>Acknowledgements</b>	<b>98</b>

# Chapter 1

## Introduction

Ultrafast nano-optics is a branch of physics that studies light on femtosecond time-scales and nanometer length-scales[VRPL09]. The knowledge about the processes governing the behavior of light at these scales is the groundwork of a new technology: photonic microprocessors that may be the next seminal breakthrough in computing. The key ingredient to such future devices are hybrid nano-structures of metal and (organic or inorganic) semiconductors that guide the light and offer light-matter interaction to allow for signal switching.

The installed computing power on earth grew approximately exponentially in the last half century[HL11]. This was possible thanks to rapid advances in microelectronics which is (at least from a physicists point of view) equivalent to advances in solid-state physics and craftsmanship in producing micro-structured semiconductor-metal-insulator devices. However, the basic working principle has not changed – modern microprocessors are still circuits of field-effect transistors as their ancestors.

Today, it is foreseeable that the growth in computing power cannot be maintained with traditional microelectronic technology. The global growth rate in computing power has supposedly already peaked in 1998[HL11]. The speed of computation for serial tasks in single processors has almost saturated around 2005. Since then, processor manufacturers concentrate on parallelization which keeps the growth of nominal computing power alive. Unfortunately, parallelization alone can not sustain the growth in computing power over the next 50 years since some tasks are inherently serial and parallelization needs scarce communication bandwidth among the sub-tasks.

A major reason for the problems with microelectronics is that electrons in high-frequency microscopic circuits radiate such that parasitic inductivities and capacities become a problem that is hard to overcome. Another reason is that quantum effects such as tunneling and confinement are complicated effects that become more important with smaller structure size.

However, a high demand for even more powerful computers continues. For example,

every researcher in scientific computing could instantly name a problem that he would eagerly solve if he had an, e.g., 1000 times faster computer. Of course, there are also commercial applications with growing computational demand such as the emerging cloud computing where data is collected by small devices but calculations are outsourced to massive data centers.

It is very attractive to replace electrons as information carrier by photons. Photons move at the highest possible speed and do not interact among each other. A light-wave is an ideal information carrier – its extremely high frequency allows to modulate it at very high sampling rates. The problem is that traditional optical devices are heavy and bulky. To bring optical computing into desktop computers or smart-phones, the step to integrated optical micro-circuitry has to be taken. The ambition of ultrafast nano-optics[VRPL09] is to provide the experimental tools and theoretical understanding that are necessary to do this step.

One tool to manipulate and guide light in nano-structured materials are photonic crystals[Yab87, JJWM08]. They interact with light in a way which is very similar to the way atomic crystals in solid state physics interact with electrons. As solids, they can be “doped” by lattice defects to form wave-guides[Yab93, JVF97] to transport light with low loss or cavities[YSH<sup>+</sup>] providing strong standing wave fields at a predefined position.

Plasmons[BDE03, Mai07] are another key player in nano-optics. Plasmon-polaritons are collective excitations of electrons in solids interacting with electromagnetic waves and vice versa[Rit57]. The name plasmon-polariton indicates their character of combined plasmon – fluctuations of the electron density in an electron gas, e.g., in a metal – and polariton – electromagnetic waves coupled to polarizable media – excitations. In the contemporary optics community and the present work they are often called plasmons and must not be confused with volume plasmons in solid state physics. Plasmons are particularly important for future micro-optic application since they provide a way to confine and guide electromagnetic fields to spacial extensions below the diffraction limit.

Recently, localization of light in disordered media[WBLR97] underwent a revival in ultrafast nano-optics. Visible light can localize, i.e., give strong field enhancements at certain points, in disordered dielectric media[3]. It was also found that SPPs can localize at rough metal surfaces as well[ABC<sup>+</sup>12]. In both cases it was pointed out that the strongly enhanced fields can be used to interact with nonlinear materials. Moreover, the nonlinear interaction of the electromagnetic field with the surrounding material allowed for the experimental observation of the localized fields in both cases.

Nonlinear light-matter interaction is the key to allow for the interaction among photons in ultrafast nano-optics. In semiconductors processes such as stimulated emission or saturable absorption allow for amplification and switching of optical signals. They can also act as couplers of electronic and nano-optic signals in hybrid devices.

And so the wheel is come full circle. Wave-guides, plasmonic or photonic, can easily be tuned to support light of a particular energy and nonlinear devices can switch light to travel along one part or the other. Having plasmonic and photonic wave-guides guiding the light along tight lanes, structures to localize light fields at certain positions and nonlinear materials completes the toolbox needed for ultrafast nano-optical integrated circuitry.

## 1.1 Scope and Overview

This work summarizes my research in the past years. I worked in the project “Exciton-plasmon interaction in metal-semiconductor hybrid nano-structures” in the DFG priority program 1391 “Ultrafast Nanooptics”, in the group of Prof. Erich Runge at the Technische Universität Ilmenau. The focus of this work are theoretical and computational aspects of the physics governing ultrafast nano-optics.

The results presented here were achieved in close collaboration with various partners doing state-of-the-art experiments. Within the priority program, we worked with the group of Prof. Christoph Lienau in Oldenburg. International collaborators are Prof. Dominic Zerulla from the University College Dublin and Profs. Takashi Yatsui, Kokoro Kitamura and Motoichi Ohtsu from the University of Tokyo.

First, this work discusses the excitation and propagation of SPPs at nano-structured lattices of elaborately shaped metal nano-scatterers[1, 4]. Coupling of visible, far-field light to SPPs is an important part of nano-photonic devices since the signals have to be brought into or out of any useful device at some point. Here, we focus on the question how polarization and symmetry of a complex structure influence the coupling of far-field light to SPPs.

Another part of this work concerns the coupling of SPPs excited at a metal grating with a dye layer. In particular, the formation of strongly coupled SPP – dye-exciton modes (also called Plexcitons/Excimons) is observed in such systems[5, 6]. Reflection spectra showing the typical avoided crossing behavior of coupled oscillators are calculated and compared to experiments. This mechanism combined with the strong non-linearities of the dye provides a way to switch far-field light with far-field light of another frequency with high efficiency at 1 *ps* timescales. The possibility to compensate plasmon-damping with gain materials is also discussed.

The last part of this work also describes how visible light localizes in a system where ZnO (zinc-oxide) nano-needles are vertically aligned but randomly distributed on a sapphire substrate. Here we see strong field enhancements[3] at certain positions in the needle array. These field enhancements give rise to strong nonlinear effects at very small length-scales. Such random structures can prospectively be grown at very low cost com-

pared to usual, deterministic nano-structuring. This research is important for future nano-phonic applications like chemical detectors and random lasing.

For all these topics, the actual experiments and samples are described in a brief manner. Then, the theoretical modeling the choice of the computational tools is discussed. The actual implementation of each model is described and results are presented and compared to the experiment.



# Chapter 2

## Plasmons in arrays of symmetry-breaking nano-dots

### 2.1 Introduction

In order to excite a surface plasmon polariton (SPP) that travels along a metal surface with visible light, the momentum mismatch has to be overcome (see appendix A.3). In general, momentum is conserved where translation invariance holds. A way to obtain additional momentum is to break the translation invariance. In principle, every translation invariant structure can be used. One example is a step in the refractive index of a dielectric coating on a metal[RSE<sup>+</sup>09]. By illuminating the step with a laser, SPPs are generated that propagate along the metal surface (see Fig. 2.1a). In order to be radiated into far-field light, the SPPs again have to be scattered by an (momentum providing) obstacle. Since the metal is flat, these radiative losses are suppressed and only OHmic losses remain in such experiments.

A very different way to excite SPPs are so called corrugated metal surfaces[ABC<sup>+</sup>12].

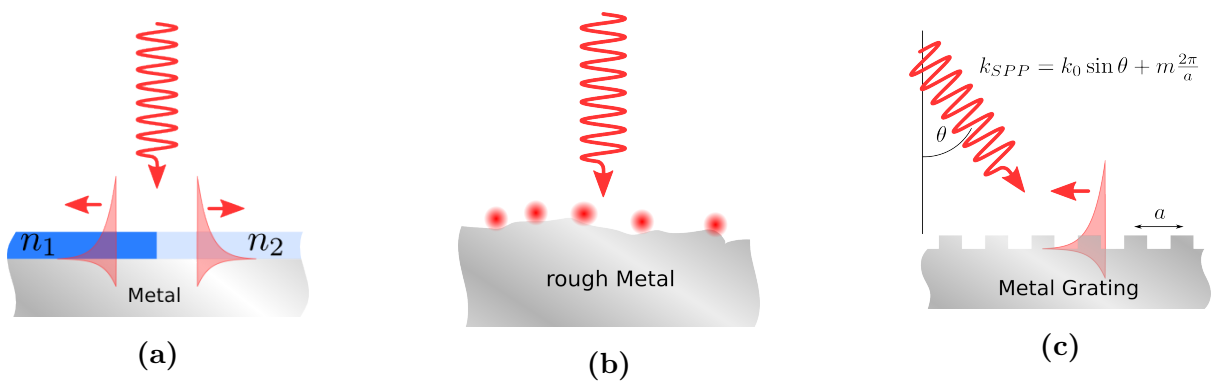


Figure 2.1: Excitation of SPPs at metal-dielectric interfaces by (a) structured dielectric coating, (b) rough metal surfaces and (c) and metal gratings.

Here, a very rough metal surface breaks the translational invariance in all directions as shown schematically in Fig. 2.1b. If such a surface is illuminated, SPPs can be started into all directions along the surface. The interference of many waves traveling in different directions give rise to complicated standing wave patterns. These patterns can be observed by photo-emission electron microscopy (PEEM) which sensitively measures the near-field intensity with the high spatial resolution of an electron-microscope. Albeit the fact that these modes have very strong radiative losses, it is found that the near-field patterns are stable and show properties typical for localized wave fields (see Chap. 4).

Another way right in between random rough surfaces and single obstacles are gratings as shown in Fig. 2.1c. Here, the individual scatterers are placed periodically onto the surface. The limit of an almost flat, one dimensional grating can be handled analytically and shows the major features of SPPs living on a grating. In particular there occur distinct SPP modes having different in-plane momenta (see Fig. A.1 in the appendix). They can be selectively excited by choosing frequency – angle of incidence pairs. As for a rough surface, the SPPs can easily couple back to radiative modes such that radiative losses are strong. For this reason, the lifetime of SPPs is very short on gratings.

Even more modes can be brought into the game when two-dimensional gratings are considered. The degrees of freedom are the relative angle between the two lattice vectors and the angle of incidence with respect to the surface normal. As a result, the SPP resonances occur on a two dimensional band-structure in reciprocal space. Such structures allow for optical experiments with waves in exotic band-structure regions such as DIRAC points in honeycomb lattices of metal-particles[WWB<sup>+</sup>13].

The type of modes that are supported by the grating are exclusively given by the periodicity but the coupling efficiencies between the different modes depend on the FOURIER components of the grating structure. This is particularly simple for a sinusoidal grating which obviously has only one such component. The fraction of light that is scattered into the different propagating and SPP modes sensitively depends on the shape of the individual scatterers.

The interplay of the lattice and the individual scatterers is very similar to solid state physics. Basic features such as points of high symmetry in the plasmonic/electronic band-structure are given by the structure of the lattice. The details, e.g., level splittings, are governed by the resonances/orbitals of the individual scatterers/atoms.

In solid state physics, the band-structure tells us which modes exist for a given momentum. What one measures are transitions, e.g., electrons that are emitted into the vacuum in a photo-emission experiment. Transitions from band to band are called inter-band transitions and are found as absorption edges in optical spectra. The probability of such transitions depends not only on the bare existence or energy difference of the bands involved. Instead, FERMIS golden rule states that the transition probability is

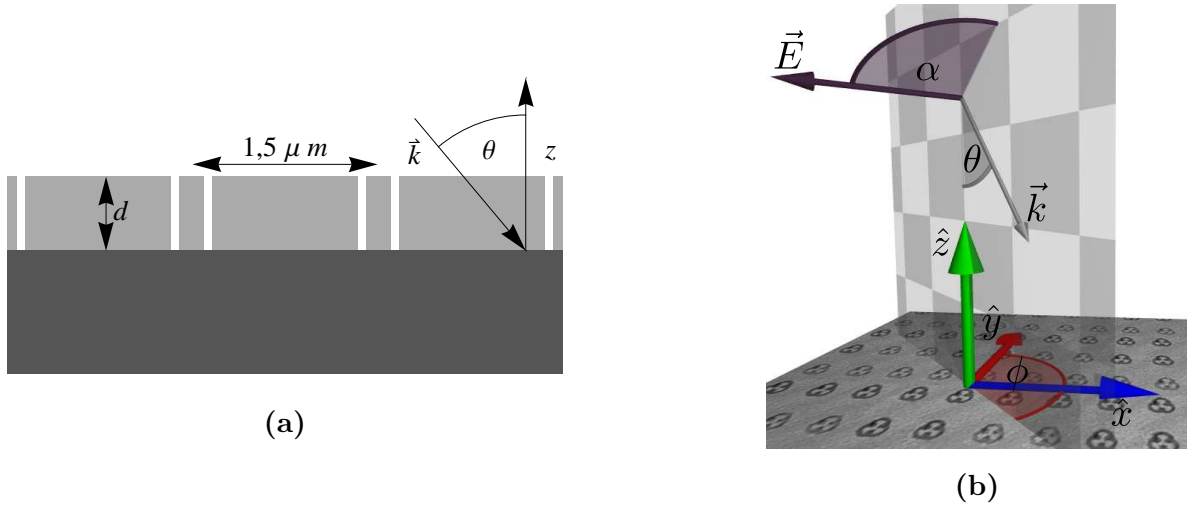


Figure 2.2: Panel (a) shows a section along the  $\hat{x} - \hat{z}$  plane showing the silicon substrate (dark gray), the nano-structured silver film (light gray) and air (white). Panel (b) is a schematic overview of the geometry of the incident electromagnetic wave. The structured surface lies in the  $\hat{x} - \hat{y}$  plane. The plane of incidence (checkered) is defined by the  $\hat{z}$ -axis and the wave vector  $\mathbf{k}$ . The polar angle  $\theta$  and the azimuthal angle  $\phi$  define the direction of incidence. The polarization angle  $\alpha$  defines the direction of the electric-field vector  $\mathbf{E}$ ; from Ref. [1]

proportional to the squared dipole matrix elements[GM12, Sec. 11.3.2]. The dipole matrix elements sensitively depend on the relative symmetry properties of the involved eigenfunctions. As a consequence, there are *dipole forbidden* transitions which cannot be observed because their dipole matrix elements vanish for symmetry reasons.

Similarly, the coupling among several optical modes strongly depends on the symmetry of the individual eigenfunctions. In contrast to electronics, the polarization enters the scene as an additional degree of freedom due to the vector nature of electromagnetics. The far-field properties of a plasmonic system strongly depend on the polarization even in the simplest cases. As shown in appendix A.3, there is a polarization where no SPPs can be excited at all.

## 2.2 Experiment

Based on the innovative experiments in the Zerulla group[ABZ07, AVBZ09], we study the possibility of shifts in the polarization angle at which SPPs are excited on gratings with individual scatterers that break the global symmetry of the grating. For this purpose, rotor-shaped scatterers are etched into a silver surface as a square lattice (see Fig. 2.2b). Thanks to the 2-dimensional structuring, the incident light can be scattered into several far-field diffraction orders in both, the  $\hat{x}$  and  $\hat{y}$  directions. In addition, SPPs can be

excited that travel along the surface and are eventually scattered into one of the far-field modes. The incident light can either be directly diffracted or coupled into SPPs. Light that is radiatively coupled out again from the plasmonic modes will also contribute to the far-field.

In Ref. [ABZ07], circular and three-fold symmetric dot shapes are compared. While the first are compatible with the global  $C_4$  symmetry of the square lattice, the latter reduce the global symmetry since they belong to the  $C_3$  group. The size and consequently the scattering efficiencies of both types are comparable.

The structures were fabricated by first etching the dots into a silicon wafer using electron beam lithography. Since plasmon polaritons can be best excited at interfaces of a good conductor and a dielectric, a 80 nm silver layer was deposited on top. An additional 5 nm platinum adhesion layer between silicon and silver should have no influence on the optical properties but is only needed for fabrication.

In the present study, only the silver-air plasmon is excited. In otherwise very similar studies, it is found that coupling of light through a metal slab with a lattice of holes is surprisingly large[ELG<sup>+</sup>98, GE07]. In other experiments, the metal-air and the metal-semiconductor SPPs of a semiconductor-metal-air hetero-structure were brought into resonance[VPS<sup>+</sup>08].

In the experiments, a red laser ( $\lambda = 632.8$  nm) served as a light source[ABZ07, AVBZ09]. Since the source is continuous wave, the energy was constant in all experiments and not used as an additional degree of freedom. Instead, various angles and polarizations were varied to observe the polarization-resolved reflectivities in reciprocal space.

The reflectivity was measured with a photo-detector. Detector, sample and light source were placed in a goniometer. With this setup, the angle of incidence could be varied and the reflected light could be measured for each diffraction order. A schematic overview of the setup is given in Fig. 2.2b.

First, the polar angle of incidence was scanned while observing the specular (0th diffraction order) reflection. The excitation of SPPs gives a characteristic dip in the reflectivity at the SPP resonance (see Fig. 2.3). The position of the dip is found at a point where the in-plane momentum  $\hbar\mathbf{k}_{\parallel}$  matches the SPP resonance condition[Rae88]. The dip comes from the fact that light which is coupled into the SPP mode is damped in the metal due to OHmic losses. While the position of the resonance is fixed by the lattice parameters, the depth and the width of the resonance depend on details of the structure.

It was the original objective of the work[ABZ07] to investigate this shape dependence. As an additional aspect, the trefoil-shaped structures give an interesting polarization-dependent effect. Following Ref. [ABZ07], we use compass notation (N, S, E, and W) to indicate  $\phi = 0^\circ$ ,  $\phi = 180^\circ$ ,  $\phi = 90^\circ$ , and  $\phi = -90^\circ$ , respectively. Taking a look at Fig. 2.4, it is an obvious prediction that every quantity should be perfectly symmetric

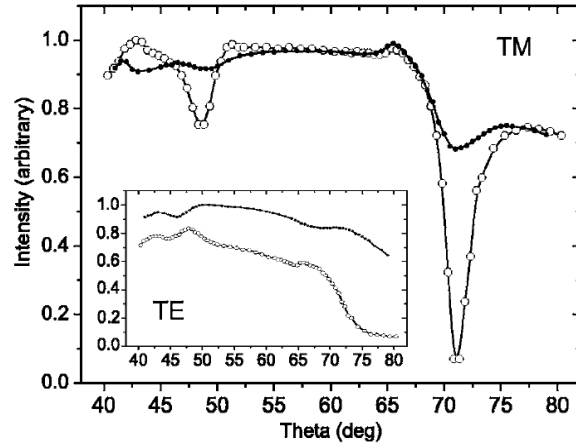


Figure 2.3: Normalized far-field intensity (proportional to specular reflectivity) for circular scatterers (unfilled dots) and rotors (filled dots) as function of the angle of incidence. The characteristic dip in p-polarization (TM) around  $70^\circ$  is the SPP resonance concerned in this study. Such a dip is not found in s-polarization (TE, inset); from Ref. [ABZ07]

around  $\alpha = 0$  and  $\alpha = \pi$  for the N and S direction. This can easily be justified by observing that around  $\alpha = 0$  the system is mirror symmetric with respect to the plane of incidence. Note that this symmetry also implies that there is an extremum at  $\alpha = 0, \pi$  in all measured quantities.

For the E and W cases, the mirror symmetry is broken due to the shape of the individual scatterers. In this case, measured quantities have some periodicity in the sense that a shift of  $\alpha$  by  $\pi$  does not change the results, but minima and maxima of reflectivities can be somewhere else than  $\alpha = 0$  and  $\alpha = \pi$ .

The position of the minima and maxima with respect to  $\alpha$  were investigated in the next part of the experiment. The polarization angle was scanned at the plasmon resonance polar angle  $\theta_{res}$ . It is found that, e.g., the SPP related extrema in the second order reflectivity  $R_2(\alpha)$  are found at  $\alpha \approx \pm 30^\circ$  [ABZ07]. It was speculated that the value of  $30^\circ$  might be a direct consequence of the  $C_3$  symmetry where this particular angle is omnipresent. It was emphasized that such shifts do not imply that the maximum of SPP excitation is also shifted from  $\alpha = 0$ . In control experiments with ring shaped nano-dots no shifts of these maxima were found.

Reference [AVBZ09] points out that the reflected far-field light undergoes a polarization twist between the in-coupling of the incident light to the SPP, the propagation of the SPP along the surface and the out-coupling to diffraction orders. Further experiments were performed to confirm that the polarization of incoming and outgoing light is different. In particular, the incident light was polarized to  $\alpha = 0$  and an analyzer was placed between sample and detector. Here, it is also seen that the maxima in reflected

light are not at the polarization of the incident light but slightly shifted for the E and W configurations.

## 2.3 Modeling

The experimental finding of a polarization twist in square arrays of threefold symmetric nano-dots leads to the question how the actual near-fields look like and how they interact with the far-field. To answer these questions, the fields were calculated by solving MAXWELL's equations by means of numerical methods.

One important complication is that the system is inherently 3D meaning that the material properties strongly depend on all three CARTESIAN coordinates. Also, there is no fancy coordinate transform in which one of the dimensions would appear flat. The experiment involves fine metal structures which are problematic in two ways: fine structures are always a problem, because the computational grid has to be small enough to satisfactorily resolve the geometry of the model. Even worse, strong antenna-like field enhancements accompanied by high field gradients are to be expected near sharp metal edges. This also means that high spatial resolutions are necessary in numerical calculations involving nano-structured metal.

### 2.3.1 Methods

In finite-differences time-domain (FDTD) calculations, one is inherently restricted to a cubic spatial grid, the so called YEE lattice[Yee66]. At each point of the grid, one of the six field components is stored. The components are distributed in a clever way such that there is just enough information to calculate the discretized  $\nabla \times$  operators in the two MAXWELL equations  $\nabla \times \mathbf{E} = -\partial_t \mathbf{B}$  and  $\nabla \times \mathbf{H} = \partial_t \mathbf{D} + \mathbf{j}$ . In particular, in a time stepping scheme, the new value of each  $\mathbf{H}/\mathbf{E}$  component depends only on its own old value and the old values of the surrounding  $\mathbf{E}/\mathbf{H}$  components.

As a consequence of the restriction to *cubic* grids, enhanced resolution in a particular region, namely near the metal-structure, cannot easily be achieved. Instead, the resolution has to be increased everywhere, even in the far-field region, where the field undergoes only weak spatial variations. An in-homogeneous grid (i.e., some cubes become cuboids) is possible but a fine grid in one point still implies a fine grid in regions far from this point. This is due to the fact that in electrodynamics, reflection occurs at *all* interfaces between regions with different properties. This is not only true for material interfaces but also for the coarse grid – fine grid interface. Thus, the coarse-to-fine transition has to be as slow as possible or complicated tricks must be played in order to suppress artifacts.

The FDTD method was still chosen over a finite element method (FEM) for several reasons. For a given amount of main memory (e.g. 16 GB on a 2009 Workstation) one

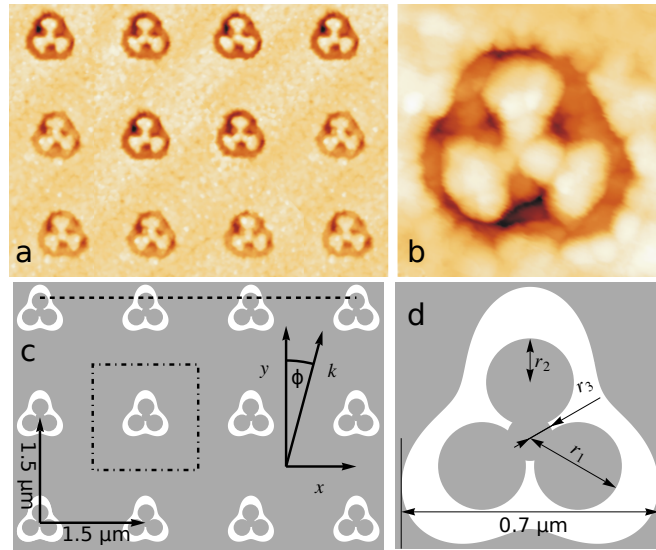


Figure 2.4: Atomic force microscopy image of the array (a) of silver structures used in Refs. [ABZ07] and [AVBZ09]. The total diameter of a single structure (b) is  $0.7 \mu\text{m}$ . Panel (c) and (d) show the model system used in the calculations. The dash-dotted square in (c) marks the computational unit cell. The dashed line in (c) marks the section plane for Fig.2.2a; from Ref. [1]

is limited to a maximum number of mesh nodes since all field components and possibly tensor-valued material properties have to be stored at each node. The FDTD time-stepping runs with negligible memory overhead, such that basically all memory can be used for physically relevant quantities.

The result of a FEM calculation are coefficients of an expansion of the solution into a set of orthogonal functions in each cell. However, the number of degrees of freedom needed to obtain the same information is on the same order of magnitude in FEM and FDTD. In classical frequency domain FEM, the solution is obtained as solution of a sparse linear system of equations with the dimensionality being the number of degrees of freedom. Thus, for a FEM solver, memory is not only needed for the solution itself. One also has to store the sparse system matrix of size  $\mathcal{O}(N)$  and, in the case of a direct solver, the LU decomposition (not sparse in general) of size  $\mathcal{O}(N^2)$ . Iterative solvers are less memory intensive but often converge slowly or not at all[EMR90].

Finally we used the commercial software Lumerical FDTD Solutions[lum08]. The experience with this software allowed for quick implementation of problems in later projects, e.g., research of the influence of metal gratings in organic solar cells[7].

The calculations were performed in one unit cell (dash-dotted line in Fig. 2.4c) with dimensions of  $1.5 \times 1.5 \mu\text{m}^2$ . BLOCH-periodic boundary conditions were used in the  $\hat{x}$ - and  $\hat{y}$ -directions to enforce periodicity of the fields. The BLOCH boundaries also allow for the application of plane-wave sources with oblique incidence. In contrast to periodic

boundary conditions, they take into care that there may be a phase shift in the fields from one boundary to the other.

As discussed in Sec. 4.4 below, angle of incidence and pulse-length can not be chosen independently in FDTD calculations with BLOCH boundary conditions. In the present case, we are lucky that the experiment uses a continuous wave laser. The modeling is perfectly fine with temporally long pulses where all relevant angles of incidence can be chosen. In general, the angle-of-incidence – bandwidth relation has to be kept in mind and reconsidered for each model.

### 2.3.2 Geometry

Right in the middle of the unit cell, one nano-scatterer as shown in Fig. 2.4d was centered. The shape of an individual nano-dot consists of 4 overlapping circles. The radii as indicated in Fig. 2.4d were chosen to be  $r_1 = 0.27 \mu\text{m}$ ,  $r_2 = 0.119 \mu\text{m}$  and  $r_3 = 0.063 \mu\text{m}$ . For the outer shape, two models were implemented. The first uses a single circle of radius  $r_0 = 0.35 \mu\text{m}$ . The second shape is described by the function  $r(\phi) = 1 + \frac{1}{4} \sin(3\phi + \pi)$  in polar coordinates. It is scaled such that it fits into a circumscribed circle of radius  $r_0$ . It was drawn to a pixel graphic with Mathematica[mat10] and as such imported into FDTD solutions.

Having both shapes, one can investigate whether the broken symmetry of the inner or outer shape has more influence on polarization-dependent effects. The AFM pictures in Fig. 2.4 clearly show that the experimental realization has the three-fold symmetry in both: the inner and the outer shape.

A sketch of the layer system in the  $\hat{\mathbf{z}}$  direction is shown in Fig. 2.2a. In the  $\hat{\mathbf{z}}$ -direction, there is a substrate layer of  $0.25 \mu\text{m}$  dielectric material with silicon parameters. It follows  $80 \text{ nm}$  of metal with silver parameters (see Fig. 2.5) containing holes of vacuum, which form the actual structure. In Lumerical FDTD, materials are chosen from a built in material database. Internally, multi LORENTZian fits to experimental data-sets are calculated. This is necessary since the FDTD method needs so called auxiliary differential equations to model the response of dispersive materials. The automatic procedure worked quite well most of the time. However, the quality of the fits was manually checked for plausibility because sometimes artifacts occurred. In particular, at the points where data from different experiments are stitched together, unnaturally sharp LORENTZians were fitted in unfavorable circumstances. In such cases, manual intervention is possible within the graphical user interface.

Finally  $1.18 \mu\text{m}$  of vacuum cover the structure. The thick vacuum layer was necessary since we want to compare our calculated results to measured far-field diffraction orders. Near the metal structures, most of the electromagnetic field is contributed by evanescent near-fields which decay exponentially into the vacuum. Thus, to obtain far-field proper-



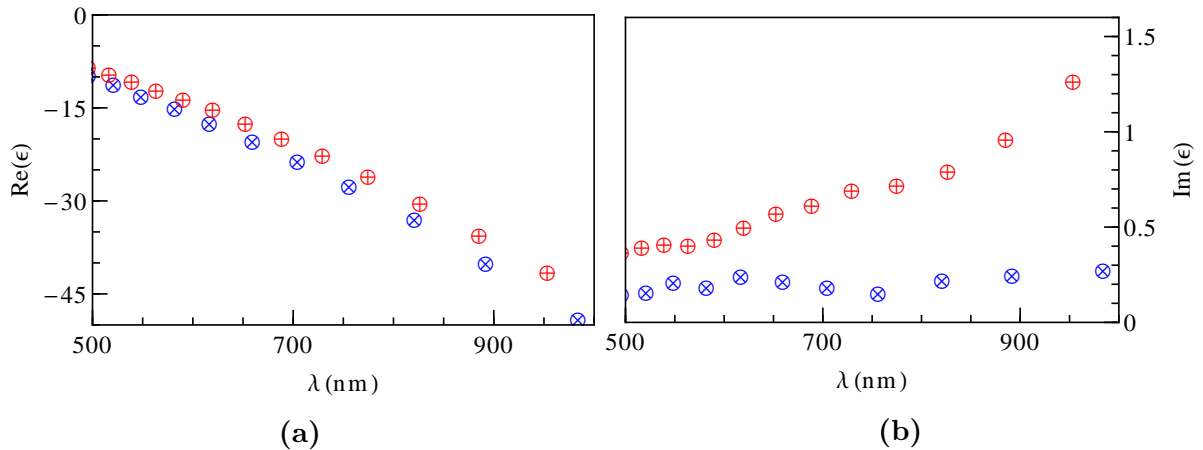


Figure 2.5: Experimental values for the dispersion of silver. The real part of  $\epsilon$  is shown in (a) and the imaginary part in (b). Data from JOHNSON & CHRISTY [JC72] are shown as blue  $\oplus$  and those from PALIK [Pal85] are shown as red  $\otimes$ . The actual values differ depending on the preparation method of the silver. We chose to take the values JOHNSON & CHRISTY.

ties, one has to calculate with a vacuum layer thick enough for the far-field contribution to become predominant over the near-field contribution.

Additionally, several strongly absorptive perfectly matched layer (PML) areas [Ber94] are used as non-reflective boundaries on the top and bottom of the simulation area. The PMLs are good in absorbing traveling far-field light and bad in absorbing evanescent fields [TH05]. This gives additional reasoning for a thick vacuum layer.

A plane-wave source was used to excite the electromagnetic fields. In particular, a long GAUSSIAN pulse was used to avoid switch-on and switch-off artifacts. In Lumerical FDTD, plane-wave sources can easily be configured to emit light at predefined polar, azimuthal and polarization angles.

As typical for FDTD calculations, a cubic computational mesh was used [TH05]. As a special feature of Lumerical FDTD, a mesh refinement could be applied to the region around the nano-scatterer. In this region, the mesh is still cubic but has a higher density. The resolution was 8 nm around the nano-scatterers and gradually smaller in distant areas. Note that FDTD solutions method does not allow for total freedom in placing refined areas at will. Rather, enforcing a fine mesh in some region has global influence. Consequently, the variation in mesh resolution is limited.

## 2.4 Data collection and far-field decomposition

An FDTD calculation gives, in principle, the electric and magnetic fields at all mesh nodes and for all time steps. A short calculation shall visualize the amount of data

available. Having mesh cells with edge length 10 nm in a cube with edge length 5  $\mu\text{m}$  gives  $500^3 = 1.25e8$  mesh cells. If one stores 6 (3 electric and 3 magnetic) components in complex double precision numbers ( $6 \cdot (8+8)$  bytes), one ends up at about 11 Gigabytes of data content. In addition, (complex, tensor-valued) fields describing the material properties have to be stored for each cell. From this very rough estimation, one draws the conclusion that one needs huge amounts of main memory and thus, powerful computers for 3D FDTD calculations.

If one does the calculation for a reasonable time span (e.g., 150 fs) with steps of 0.05 fs, the resulting amount of data in  $\mathbf{E}(\mathbf{r}, t)$  and  $\mathbf{H}(\mathbf{r}, t)$  is multiplied accordingly. To compare our calculations with the experiments, it is also necessary to perform calculations for 4 values of  $\phi$  and ranges of  $\theta$  and  $\alpha$ . Concluding this point, it is not feasible to store all the data for later post-processing.

In this particular project, the data collection can be highly simplified by exploiting the fact that we only want to compare data to an experiment with a continuous wave laser stably working at 632.8 nm wavelength. Also, we do not need information everywhere in the unit cell. Instead, we are interested in the near-field distribution and the far-field reflectivity. For this reason, data was only collected in two  $\hat{\mathbf{z}}$ -normal planes, namely one 20 nm and another 1120 nm above the metal. To obtain the fields for given frequency instead of given time, a FOURIER transform has to be calculated.

The FOURIER transformed field  $\tilde{f}(\omega)$  for a given frequency  $\omega$  can easily be obtained from an FDTD calculation with the simple formula

$$\tilde{f}(\mathbf{r}, \omega) \approx \sum_{i=0}^{\text{fields decayed}} f_{FDTD}(\mathbf{r}, t_i) e^{i\omega t_i \Delta t} \quad (2.1)$$

meaning that the field just has to be multiplied by a factor and to be accumulated. This happens on the fly at each time step without wasting memory during the simulation. A dedicated window function is not necessary since the source field already has a GAUSSIAN envelope. Of course, it is important to run the calculation for some time before the pulse starts and long enough for all fields to have decayed.

From the FOURIER transformed field, a dynamic expansion  $f_{\text{harm}}(\mathbf{r}, \omega, t)$  can be calculated from the simple equation

$$f_{\text{harm}}(\mathbf{r}, \omega, t) = \Re[\tilde{f}(\mathbf{r}, \omega) e^{-i\omega t}] \quad (2.2)$$

It can be used to visualize the field over an optical cycle as a movie. It is suggestive to play it in infinite loops as it is periodic in  $t$ . The time averaged intensity of the time harmonic field proportional to the square modulus of  $\tilde{f}$ . This quantity is often used in plots of FDTD calculated fields.

While the tools up to here already give all the interesting information about the near-field, the far-field still has to be decomposed into diffraction orders (remember that we

are interested in reflectivities in various diffraction orders).

On this purpose, we followed two paths. First, there is a decomposition into grating orders readily available in FDTD solutions. With this, our tests gave results comparable to the experiment for some orders and wrong results for others. This is supposedly not due to the algorithm but due to incomplete documentation of the black-boxed tool. In particular, it is hard to assign the numbers to grating orders in the scripting environment of Lumerical FDTD while everything worked in the graphical user interface. We had to rely on the scripting environment since the large calculations (angular scans) were performed on a cluster as batch jobs and it is highly convenient to perform the necessary post-processing on the fly (in contrast to opening a huge file and clicking through menus for lots of data-sets).

On this reason, a quick and simple decomposition method was implemented as an external program. It solves the following problem: For given  $\mathbf{H}(x, y)$ , find  $\mathbf{h}_{nm}$  such that

$$\mathbf{H}(x, y) = \sum_{nm} \mathbf{h}_{nm} \exp(i(k_{nmx}x + k_{nmy}y)) . \quad (2.3)$$

The  $\mathbf{k}_{nm}$  are the wave vectors of the grating orders and known in before since

$$\mathbf{k}_{nm} = \mathbf{k}_{inc} + n\mathbf{G}_x + m\mathbf{G}_y , \quad (2.4)$$

where  $\mathbf{G}_x$  and  $\mathbf{G}_y$  are the reciprocal lattice vectors only determined by the lattice parameters (i.e., the periodicity) and  $n, m \in \mathbb{Z}$ . The number of far-field orders (i.e., the highest positive and smallest negative  $n$  and  $m$ ) is known from the condition that all  $\mathbf{k}$ -components have to be real while the dispersion relation is fulfilled. Note that this is not true for near-fields, where  $\mathbf{k}$  can be complex.

Given a set of sampling points  $(x_i, y_i)$  the problem is of type

$$\mathbf{b} = \mathcal{M}\mathbf{a} , \quad (2.5)$$

i.e., a linear system of equations where  $\mathbf{b} = (H_x(x_1, y_1), H_y(x_1, y_1), \dots, H_z(x_N, y_N))$ ,  $\mathbf{a} = (k_{11x}, \dots, k_{NMz})$  and  $\mathcal{M}_{ij} = e^{i(k_{n_j, m_j} x_i + k_{n_j, m_j} y_i)}$ . The sampling points are chosen such that the system is over-determined and that there is no rank deficiency in  $\mathcal{M}$ . We found that the latter point is vitally important to achieve good results. In particular sampling points arranged regularly on lines along  $\hat{\mathbf{x}}$  or  $\hat{\mathbf{y}}$  or other highly symmetric directions should be avoided. Instead, randomly chosen sampling points are a safe and convenient alternative.

The program was written in C++ and reads the field in the HDF5[hdf10] format using the freely available libhdf5 library. The diffraction orders are calculated given the frequency and the lattice parameters from Eq. 2.4. Then the matrix  $\mathcal{M}$  is assembled and the problem is solved using the `zge1sd` routine from the LAPACK[ABB<sup>+</sup>99] package.

Since the decomposition assumed that the field consists of traveling far-field modes, it only works reliably if near-fields have already decayed. As mentioned in the modeling section, this is ensured by a vacuum layer with a thickness of more than 1  $\mu\text{m}$ .

To assure that the decomposition went well, the field is reconstructed from the expansion coefficients  $\mathbf{h}_{\text{mn}}$  by a matrix multiplication using the LAPACK routine `zgemm` and compared to the input field. In all data presented in this work the program worked reliably. We reliably obtained error messages due to bad reconstruction quality in cases where we provoked errors by constructing fields and trying to decompose into non-matching  $\mathbf{k}_{\text{nm}}$ .

## 2.5 Results

In first calculations, scans along the angle  $\theta$  were performed at fixed polarization  $\alpha = 0$ . In this polarization, the excitation of SPPs can be expected. As already mentioned, there are no SPP excitations at  $\alpha = \pi/2$ . An SPP-related dip in the reflectivity was found at  $\theta = \theta_{\text{SPP}} = 65^\circ$ .

At a first glance, this value is in slight disagreement with the value of  $71.3^\circ$  reported in[ABZ07] and the value of  $70^\circ$  reported in[AVBZ09]. The first value addresses only the ring-shaped structures and one can clearly see from Fig. 2.3, that the SPP related features are much weaker in rotor-shaped structures. Thus, it is hard to give an exact minimum position for the rotor-shapes in general.

Secondly, the lattice constants in the  $\hat{\mathbf{x}}$  and  $\hat{\mathbf{y}}$  directions are slightly different in the experiment. Reported values are  $d_x = 1.45 \mu\text{m}$  and  $d_y = 1.5 \mu\text{m}$  in[ABZ07]. In the calculation, we use  $d_x = d_y = 1.5 \mu\text{m}$  which is closer to the desired square lattice, in contrast to a rectangular lattice corresponding to lower symmetry. In addition, experimental values for silver dispersion show differences that may depend on the chemical environment and the silver deposition technique (see Fig. 2.5). Such deviations can easily explain the mismatch to our findings. I should mention that our value is also not exact since we had to choose a particular dispersion for the silver and obtained only very few values (remember that each data-point costs some CPU-days) around the minimum. We can say for sure that the minimum is in the interval  $\theta_{\text{SPP}} = 65^\circ \pm 3^\circ$ .

As in the experiment, we now performed calculations at  $\theta_{\text{SPP}}$  with varying polarization angle  $\alpha$ . It is quite obvious that one expects an  $\alpha$  dependence since one switches the SPP excitation on and off going from p- to s-polarization. Another point of view is the well known property of MAXWELL's equations that they can be split into 2 uncoupled sets of equations describing waves of perpendicular polarizations. Thus, the incident field is a linear combination of the two polarizations, and thus, the physics should behave as linear combinations of two polarizations.

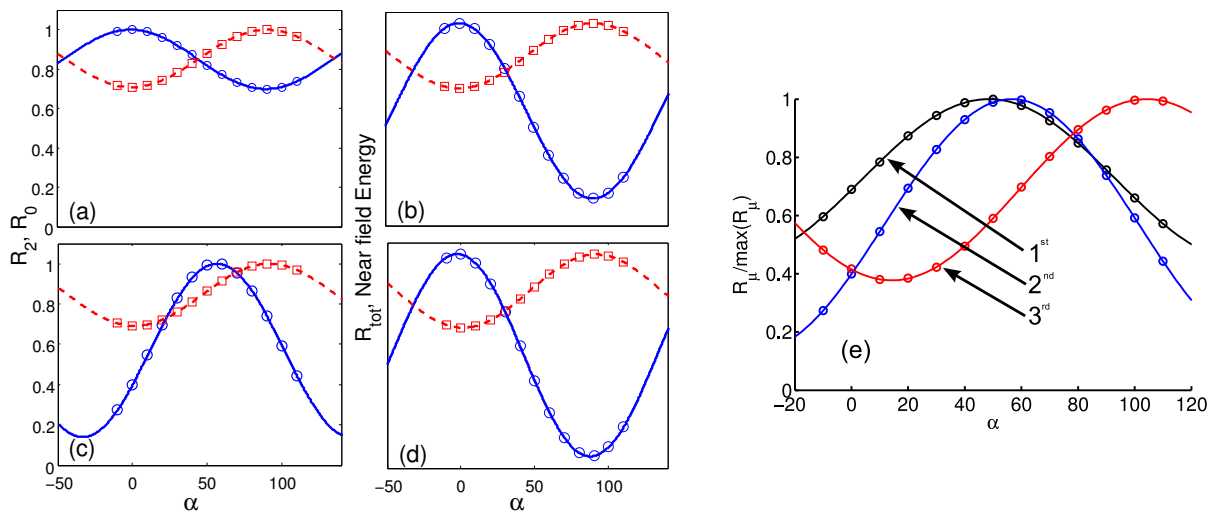


Figure 2.6: Polarization-dependent reflectivity in zeroth (red squares) and second (blue circles) reflection orders are shown in panel (a) for the north- and (c) for the west-configuration. The near-field energy (blue circles) and the total reflectivity (red squares) are shown in panels (b) (north) and (d) (west). Panel (e) shows reflectivities for several reflection orders in west configuration. Lines are fits to  $\cos^2 \alpha$  functions. All quantities are normalized such that their maximum is unity; from Ref. [1]

The polarization of a wave traveling in  $\hat{z}$  direction can be described as

$$\begin{pmatrix} E_x \\ E_y \end{pmatrix} = E \begin{pmatrix} \cos(\alpha) \\ \sin(\alpha) \end{pmatrix}. \quad (2.6)$$

If the physics is such that only, e.g., the  $E_x$  part can excite SPPs, one expects the intensity of SPP related far-field observations to have a  $\cos^2 \alpha$  dependence. To test this prediction, fits of  $F(\alpha) = a_0 + a_2 \cos(2(\alpha - \alpha_0))$  are plotted along with the data-points, e.g., in Fig. 2.6. It is found that this expectation is very well matched by the calculation results.

Taking into account that a quantity like  $R_2$  is very small, i.e., only a very small portion of the incident intensity is diffracted into that direction, the absence of scattering of the data points around the  $\cos^2 \alpha$  behavior is a hint for small numerical errors. Note that each data-point represents an individual solution of time-dependent MAXWELL's Equations by FDTD.

In Fig. 2.6a, far-field reflectivities as function of polarization  $\alpha$  in two different diffraction orders are plotted for the north configuration. As expected, symmetry around  $\alpha = 0$  is found in both quantities. In contrast, the west configuration is shown in Fig. 2.6c. Here  $R_0$  has its minimum at  $\alpha = 0$  whereas the minimum of  $R_2$  is shifted to  $\approx \alpha = -30^\circ$ .

This finding is in good agreement with[ABZ07].

Figures 2.6b and 2.6d show the total reflectivity along with the near-field energy for north and west configurations respectively. The time-averaged, electric, near-field energy is the energy contained in a volume in the region above the metal. Since we have vacuum in this region, the density of this energy can be defined as

$$W_e = \epsilon_0 \mathbf{E}(x, y, \omega) \cdot \mathbf{E}^*(x, y, \omega) [\text{Jac06, Chap.6.9}]. \quad (2.7)$$

In our case, this density is integrated along the near-field detector plane (20nm above the metal) in a post-processing step from the FOURIER-transformed electric field from the FDTD calculation. This quantity is approximately proportional to the total near field energy. In the presence of a resonantly excited SPP, it is particularly high due to the SPP-related near-field enhancement.

Both quantities are symmetric around  $\alpha = 0$  in both, north and west configurations. In particular, the near-field energy has its maximum at p-polarization. Thus, the field enhancement is still strongest at the point where the discussion in Sec. A.3 predicts the excitation of SPPs. Thus, the broken symmetry in the west configuration does not shift the polarization for optimal SPP excitation from p-polarization ( $\alpha = 0$ ). Along with this, the minimum in the total reflectivity which is due to the OHmic losses of the SPP is found at  $\alpha = 0$  giving further evidence that the SPP resonance is not shifted.

Instead, only the SPP-mediated coupling for incident far-field light to far-field diffraction orders is affected by the broken symmetry[1, 4]. Figure 2.6e shows reflectivities in the first, second and third diffraction orders for the west configuration. One can see that the shift, as well as the magnitude of the modulation are quite different for the different orders. In particular, the value of  $\alpha \approx 30^\circ$  is not common to all reflection orders, which one would expect if the value of  $30^\circ$  would directly be related to the  $30^\circ$  by which the north and west configurations differ from an individual scatterers view.

In further studies, we investigated the shape and size dependence of the shifts in the diffraction orders. To reiterate the core message, the strength of the coupling between far-field light and SPP should strongly depend on both quantities. With this in mind, one expects larger structures to mediate stronger interaction. The effect of the structure size can clearly be seen in Fig. 2.7a. Here the nano-scatterers were scaled up or down by the given percentage.

The modulation is strongest for 100% whereas it is smaller for 50% and 150%. This is in contradiction with the expectation of stronger interaction for bigger structures. In fact, a perfect cosine bump or dip in each unit-cell would allow for the best coupling among diffraction orders since the coupling at gratings is governed by the FOURIER series expansion coefficients of the shape. The FWHM of such a cosine-bump is exactly half the size of the unit cell. Having this in mind, a conclusive interpretation is that a dot of

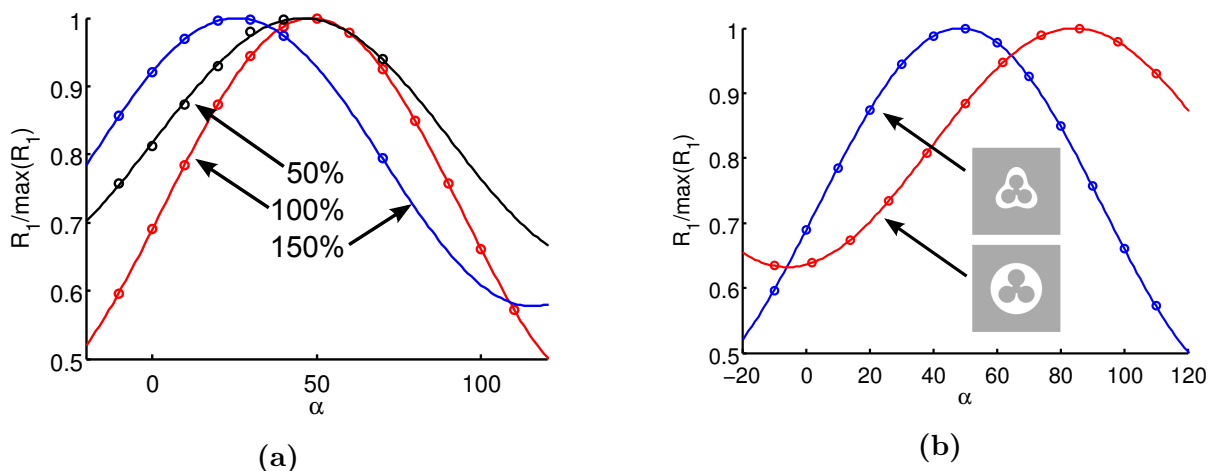


Figure 2.7: Normalized reflectivity as function of the polarization  $\alpha$  into the 1<sup>st</sup> order for **(a)** differing sizes of the nano-scatterers and **(b)** a comparison to an alternative model of the outer shape of the structure; from Ref. [1]

size 100% (= 700 nm) has 0.47 times the size of a unit cell and is closer to the optimal cosine-bump than the smaller or bigger dots.

It can also be seen in Fig. 2.7a that the shift of the curve away from symmetry around  $\alpha = 0$  is strongest for the 100% size and smaller for the others. The shifting is a non-constant function of the structure size. This gives further evidence that the value of  $\alpha \approx 30^\circ$  found in previous experiments[ABZ07] is only coincidentally near the value of  $30^\circ$  which plays an important role in the geometry of the lattice.

In addition, to the size dependence, the dependence of the shift and interaction strength on the shape of the nano-dots was investigated. As mentioned in Sec. 2.3, nano-dots with a circular outer shape were also implemented as an alternative. The resulting polarization dependence is shown in Fig. 2.7b. It can clearly be seen that the circular outer shape results in much less shift compared to the symmetry broken geometry. From this, one can conclude that the symmetry of the outer shape plays a more important role on the shifts than the inner shape. If the inner shape would be the more important part, one would not expect the curves in Fig. 2.7b to be so dramatically different.

From the FDTD calculations, the field distributions in the detection planes are readily available. Near-field results for the N- and W-configuration are shown for three relevant polarizations in Fig. 2.8. In the upper panel,  $\alpha = 0$ , i.e., p-polarization is shown. As expected, one can see the SPPs traveling along the surface. They manifest themselves as areas high of high intensity which extend over the size of the unit cell. In contrast, a standing wave pattern would look periodically structured on a length scale given by the wavelength in this sort of picture.

We found that the SPP travels mostly in between the nano-scatterers, which can clearly be seen from the fact that the near-field intensity is highest at the left and right

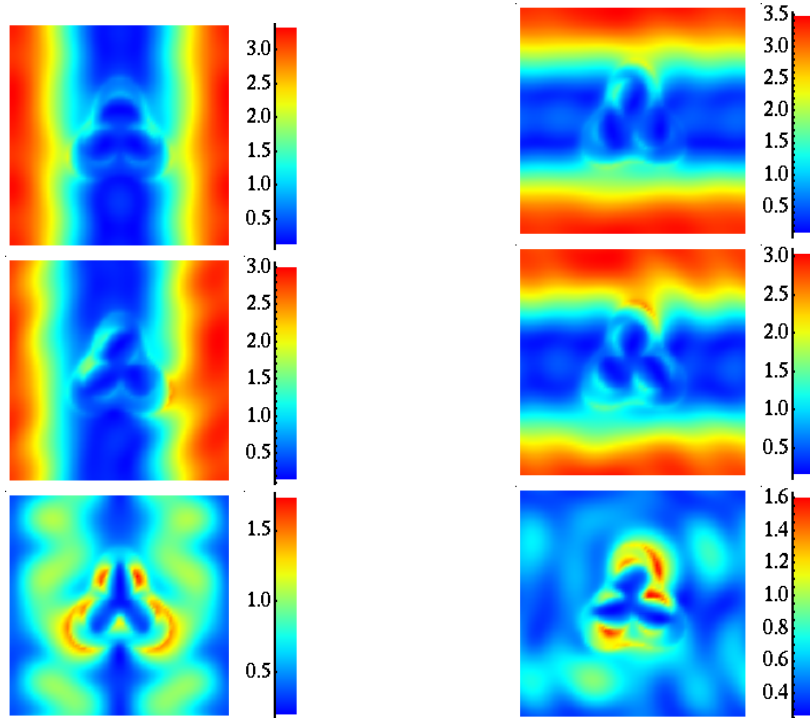


Figure 2.8: Near-field intensity distributions 20nm above the metal surface for N-(left) and W-(right) orientation. The polarization angles are  $\alpha = 0^\circ$  (top),  $\alpha = 30^\circ$  (middle) and  $\alpha = 90^\circ$  (bottom). Each panel shows an area of  $(1.5\mu\text{m})^2$ ; from Ref. [1]

respectively upper and lower border of the top panels in Fig. 2.8. In the color-coded picture, the SPP appears as red stripes along their traveling direction. The fact that the near-field close to the scatterers is comparably weak provides further evidence that we are dealing with a traveling SPP and not with a resonance of the individual scatterers. Such resonances would give strong near-fields at edges of the scatterers.

Not surprisingly, the near-field for the N-configuration is perfectly symmetric with respect to a plane spanned by a line through the center of the scatterer along the  $\hat{y}$  direction and the  $\hat{z}$  axis. Obviously, there is no such symmetry with respect to the  $\hat{x} - \hat{z}$  plane in the W-configuration shown in the upper right panel. Of course, this is due to the broken symmetry of the individual scatterers.

In the center of Fig. 2.8, the near-fields are shown for mixed s-p polarization ( $\alpha = 30^\circ$ ). In contrast to the p-case, the near-field intensity is also high at certain points right at the border of the scatterers: the fields also have a localized character while the SPP is still dominating the intensity distribution. No obvious symmetry is found in the field distributions of both configurations since the skew polarization breaks the overall symmetry of the system.

In the lower panel, the symmetry of the near-field for the N-configuration is found again, following the symmetry of the scatterer and the polarization of the incident fields.



As in the upper panels this is not found in the W-configuration. In both configurations, the contribution of a traveling SPP is completely switched off. This was expected since there are no SPPs in s-polarization.

The absence of a traveling near-field wave manifests itself in the absence of high intensity areas extending over the whole unit-cell and, in particular, over the unit-cell boundary. Instead some localized excitations are found near the nano-scatterers.

One may ask whether the polarization shifts are due to localized excitations instead of the SPPs<sup>1</sup>. This led us to calculations with a single nano-scatterer and without periodic boundary conditions. Here the excitation of SPPs is suppressed since the coupling strength of a grating is much higher than that of a point-like perturbation. We found localized modes which look like those in the lower panels of Fig. 2.8. These modes are spectrally broad and quite weak. This allows for the interpretation that they have no or only weak influence in general.

In future experiments, it can still be highly interesting to investigate the interplay of localized excitations with SPPs. In particular, individual structures with strong and sharp localized modes, such as bow-tie nano-antennas, can be arranged as a lattice, in order to couple localized and SPP modes, both having polarization-dependent excitation and radiation characteristics. It is very interesting whether one can find avoided-crossing behavior or excite SPPs with incident light which would usually have the “wrong” polarization.

---

<sup>1</sup>We thank the reviewer of Ref. [1] who pointed this out.



# Chapter 3

## Plexcitons/Excimons: coupled SPP – Dye-exciton modes

The study of subtleties involving different symmetries of lattice and individual scatterers in the last chapter is an example of ongoing research on details of SPP excitation. While some properties of SPP – far-field interaction are exclusively determined by the periodicity of the grating, other properties sensitively depend on the shape of the scatterers.

Another stepping-stone on the way to build plasmonic devices is the control of SPP propagation. The SPPs have a limited propagation length (see, e.g., App. A.3). This limitation has two main reasons. One is the OHmic damping of the plasmonic excitation in the metal. Another are the radiative losses. The out-coupling of SPPs to propagating light follows the same rules as their excitation. In particular, every structure which allows to overcome the momentum mismatch leads to radiative losses. Such structures are not only gratings but also surface roughness or adsorbates.

Radiative losses are comparably easy to prevent: just take a perfectly clean and flat metal surface. On the contrary, the OHmic losses are an intrinsic effect at metal surfaces and therefore hard to overcome. Various groups play various tricks to enhance the propagation length. Typically, a structure of various different dielectrics is combined with metal layers in order to reduce the spatial overlap of the enhanced electric near-field with the metal (see review Ref. [Ber09]). This reduces the OHmic losses and eventually increases the SPP propagation length. These methods have in common that the propagation length is enhanced by some small factor but not by orders of magnitude.

Another idea to significantly overcome the damping is to use gain media in order to amplify the SPPs *during* their propagation. A gain material is a material with negative absorbency. Such a situation is possible in few-level quantum systems such as dyes and semiconductors. One level can be pumped at an energy different from the energy of the SPP. This excitation could then be transferred into the SPP by stimulated emission[GMDL10]. Due to the characteristics of stimulated emission, such a mechanism

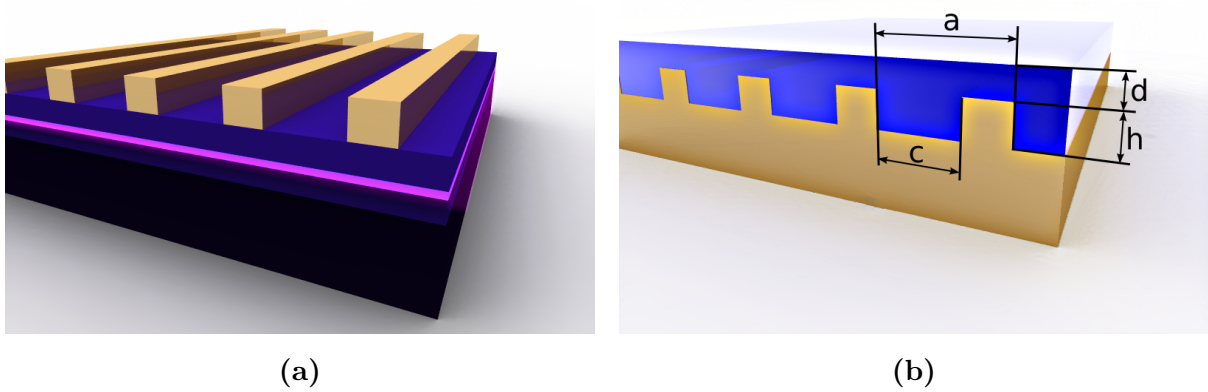


Figure 3.1: **(a)** Schematic view of a system with a gold-wire grating on top of a semiconductor quantum well. The whole structure is grown on a gallium arsenide wafer. **(b)** Gold grating with a layer of a j-aggregated dye in a polymer matrix which was spin-coated onto the grating.

would amplify the SPP while conserving coherence.

First, one has to answer the question whether there is coherent energy transfer from SPPs to quantum systems at all. On this purpose, two model systems as first step towards gain-compensated SPP propagation were investigated in the group of Prof. Lienau in Oldenburg. In the first, a semiconductor quantum well was placed beneath the lattice where the SPPs were excited. A schematic image of the system is given in Fig. 3.1a.

Indeed, strong coupling of the exciton in the quantum well and the SPP (both at the vacuum-side and substrate-side) could be shown. It manifests itself as avoided crossing behavior of the SPP related reflectivity dip and the reflectivity dip due to the absorption of the quantum well exciton[VPS<sup>+</sup>08]. The avoided crossing can clearly be seen in the differential reflectivity[VPS<sup>+</sup>08, Fig. 2] but the effect is extremely small ( $\approx 10^{-4}$ ). The avoided crossing proves the fact that there is strong coupling of the SPP and the exciton. This means that there is in fact coherent energy transfer.

A quite complicated excitation scheme was chosen in the semiconductor case. An vacuum-metal SPP (AM) was brought into resonance with an metal-semiconductor SPP (SM) by the choice of grating parameters, source energy and angle of incidence. In such a situation, energy can be coupled from the upper side through the metal slits surprisingly effective[GE07]. At this point where AM and SM are in resonance, the semiconductor exciton was brought into resonance with both of them. This scheme was necessary to obtain high near-field intensities at the quantum well position.

A drawback of the semiconductor system is the fact that it is not easy to produce a heterostructures as shown in Fig. 3.1a where the quantum well is very close to the metal.

In particular, a buffer layer is necessary which results in a non-negligible distance between the metal interface and the active layer (quantum well). This is a serious problem since the SPP decays exponentially and fast in the direction normal to the interface. Consequently, the active layer is placed in a position where the field enhancement is comparably weak.

The named problems inspired the closely related approach that was followed in a later experiment[5, 6] and is discussed in the present chapter. In contrast to the earlier experiments, the active material was chosen to be placed on top of the grating. This is hard to achieve by growing inorganic semiconductors but easily possible with organic materials that can be dissolved and spin coated onto a surface. In order to show strong coupling to the SPP, the organic material needs to have a sharp optical response and high quantum yield at the same time. This is the case for  $\pi$ -aggregated dyes[WKSM11] such as 2,2'-dimethyl-8-phenyl-5,6,5',6'-dibenzothiacarbocyanine chloride which was used in the present study. While drying from a solution, the planar molecules tend to form stacks. This can be seen in their optical response where the absorption peak red-shifts and becomes stronger compared to the monomer.

To fabricate the desired structure, the monomer is solved in a polyvinyl alcohol (PVA) solution and spin coated onto the metallic grating in order to produce a very thin dye in polymer-matrix film. The complete system is shown schematically in Figure 3.1b. With this setup, the dye can couple to the SPP on the vacuum-metal interface on the side where the external source is located. The active layer sits directly on top of the metal and, in particular in the slits. Thus, it can couple to the SPP where the near-field intensity is strongest.

## 3.1 Experimental findings

In the experiments with the dye-metal system as shown schematically in Fig. 3.1b, reflectivity spectra were collected in dependence of the angle of incidence. Ultrashort laser-pulses were utilized in order to obtain a broad spectrum per shot. After averaging the spectrum over many shots, the setup was changed to another angle of incidence and a spectrum for that angle was collected and so forth. All spectra were taken in the far-field in a reflectivity setup. Thus, the intensities in the spectrometer are proportional to the reflectivity.

The resulting bare spectroscopic data is shown in Fig. 3.2a. The method described in the last paragraph can clearly be seen to result in vertical stripes of which the image is assembled. Each stripe corresponds to a single spectrum taken at a particular angle of incidence.

The most prominent feature in Fig. 3.2a is a horizontal ridge of high intensities between 630 nm and 750 nm wavelengths. This is the spectrum of the laser which does not

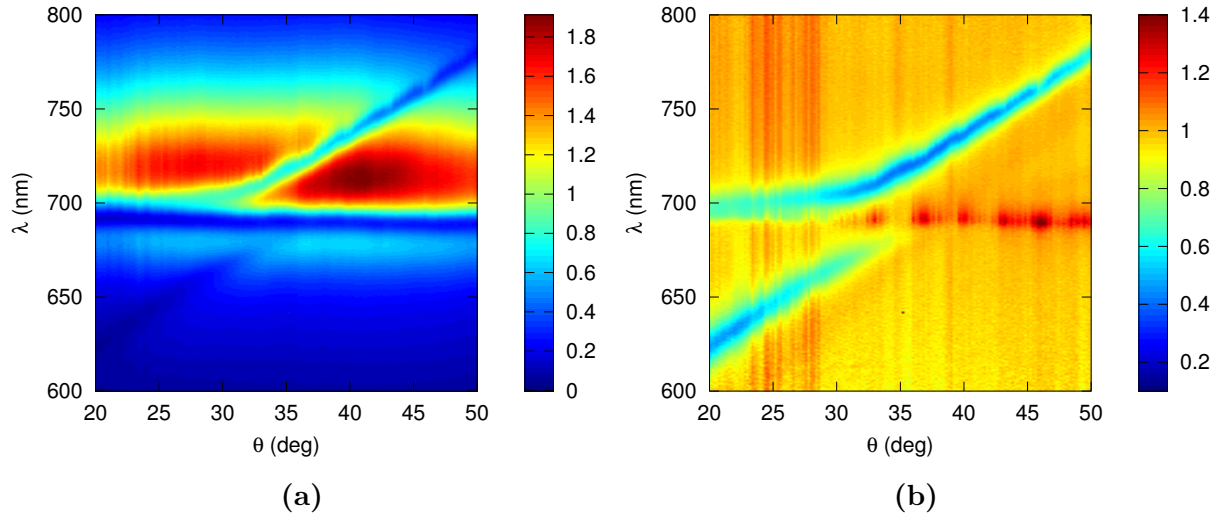


Figure 3.2: Panel (a) shows spectra of reflected light from the sample with metal grating and dye-layer  $R_{dye+SPP}(\theta, \lambda)$ . The color-map is proportional to the number of counts in the detector. One can see the spectral envelope of an ultra-short pulse centered at  $\lambda_{cen} = 725$  nm. The pulse-shape is overlaid with reflection minima that are the topic of this chapter. In Panel (b), a corrected spectrum  $R_{dye+SPP}/R_{dye}$  is color-coded.  $R_{dye}$  is the spectrum taken from a control experiment with the dye on plain flat metal.

depend on the angle of incidence. In order to get this background out of our view, relative spectra were created and usually published, e.g., in Reference [5, 6] and in Fig. 3.2b. In order to obtain such relative spectra, the spectrum of the dye and grating system  $R_{dye+SPP}(\lambda, \theta)$  was divided by the spectrum of the dye on a flat metal surface  $R_{dye}(\lambda, \theta)$  taken with the same laser.

In the bare spectrum Fig. 3.2a we find a horizontal reflectivity dip at 693 nm. The dip has a nearly constant width of  $\approx 25$  nm. In the figure it is found just below the maximum. This dip is due to the absorption maximum of the dye-molecules. Not surprisingly, the position of the dip does not depend on the angle. Its strength might increase with increasing angles of incidence since the optical path length through the absorbing material becomes longer.

Another important feature in the spectrum 3.2a is a diagonal reflectivity dip going from the lower left to the upper right of the image. It can clearly be seen as it cuts the maximum of the pulse spectrum above the dye-related dip. Below the dye-related dip, it is very weak but still visible. This dip is the SPP related absorption. At the SPP-resonance, light is coupled into the SPP which travels along the surface and is re-radiated to the far-field and OHMICALLY damped on its way. Consequently, the total reflectivity is reduced at the SPP-resonance.

Most interesting for the present chapter and the related research is the region where the two reflectivity minima intersect. Here, the question arises whether or not the two

modes couple, i.e., there is avoided crossing behavior.

Coupled oscillators occur in many branches of physics. Results are very similar for classical, quantum and electrodynamic oscillators. Quite generally, coupling phenomena of two coupled resonators can be describes by a HAMILTONIAN  $H$  as

$$H = \begin{pmatrix} \hbar\omega_x & 0 \\ 0 & \hbar\omega_{\text{SPP}}(\theta) \end{pmatrix} + \begin{pmatrix} 0 & V \\ V & 0 \end{pmatrix}. \quad (3.1)$$

Here, we assume one oscillator with the uncoupled energy  $\hbar\omega_x$  and another oscillator  $\hbar\omega_{\text{SPP}}(\theta)$  whose uncoupled energy depends on a real parameter  $\theta$ . In addition to the free system that is described by the first matrix, the coupling is introduced by coupling constants  $V$  in the second matrix. The coupling is symmetric: the action of oscillator  $X$  on oscillator  $SPP$  is the same as in the opposite direction.

The notation already implies the claim that SPP is a surface plasmon,  $X$  is an exciton and  $\theta$  is an angle of incidence. The SPP resonance depends on the angle of incidence as given by its dispersion relation while the exciton is angle-independent. I want to emphasize that this coupled oscillator model is also valid for a manifold of coupling problems in physics. Examples are coupled pendulums where one of the pendulums has a variable mass or electronic bands in a crystal where the free parameter is the wave-vector.

In all cases, the eigenvalues and thus the eigenenergies of the coupled system are

$$\epsilon_{\pm} = \frac{1}{2} \left( \hbar\omega_x + \hbar\omega_{\text{SPP}}(\theta) \pm \sqrt{(\hbar\omega_x - \hbar\omega_{\text{SPP}}(\theta))^2 + 4V^2} \right). \quad (3.2)$$

In a case where  $\omega_{\text{SPP}}(\theta)$  is a linear function (this is at least approximately true in the neighborhood of the crossing) the energies are on two hyperbolic branches in the  $\epsilon - \theta$  plane with the uncoupled energies as asymptotes. The closest distance (the splitting) of the two branches is easily calculated from Eq. 3.2 to be  $2V$ . On this reason, *coupling energy* and *splitting* are often used as synonyms. The two branches seem to avoid each other which motivates to name the whole situation *avoided crossing*.

Far from the crossing parameters, the eigenfunction of the coupled system has the character of either of the resonators. An example for this case are two pendulums of very different mass. If only the big one is excited, the small one does not have independent dynamics but just follows the motion of the big one. If only the small one is excited, the big one will just stay still due to its high inertia.

At the crossing, two types of movement are found on the two branches. In the pendulum case, there is a low-energy solution where both swing in phase, and the high energy solution where they are phase shifted by  $\pi$ . Similarly, in a molecule we have a bonding and an anti-bonding state. In our case of coupled SPP- $X$  systems, one usually speaks of upper- and lower polariton (UP and LP) branches. Note that the UP is actually under the LP in wavelength – angle of incidence diagrams which are preferentially used in the present work.

A finite lifetime of the modes enters the scene as a broadening of the modes. One distinguishes strong and weak coupling depending on whether one can observe two distinct peaks at the crossing point or whether they are washed out to a single peak[RSL<sup>+</sup>04].

In Fig. 3.2b one can clearly see that the avoided crossing is exactly what happens in the experiment. From this experimental data and with Eq. 3.2, one can easily find the coupling strength  $2V$ , which determines the minimal distance of the two branches in the  $\epsilon - \theta$  plane. This coupling strength, which is also called Rabi energy was determined to  $\approx 55$  meV[5].

The findings up to here proof the interesting fact that there is actually strong coupling between the SPP and the dye-exciton. The author finds it remarkable that we observe the formation of collective modes consisting of SPPs that are a special solution of the (classical) MAXWELL's equations while the dye-exciton is a purely quantum mechanical phenomenon.

In addition to the linear optical experiments described up to here, nonlinear pump-probe experiments were also performed. In such an experiment, the dye is saturated by the pump pulse. Thus, for the probe pulse, the dye absorption is decreased. In addition, the coupling strength becomes lower because less dye molecules are unexcited and able to take part in the coupling. This leads to a narrowing gap and eventually, in the limit of very strong pumping, the gap vanishes.

In all cases, the SPP related reflectivity dip remains but its shape changes from the two bent branches to a single line with increasing pump strength. It is emphasized in Ref. [5] that even a slight shift of a deep dip results in a strong change of absolute reflectivity for wavelengths in the slope of the dip. In the present case, the pump induced change in reflectivity is up to 40% for a probe pulse 150 fs after the pump.

Even more exciting is the fact that this pump induced effect is very short-lived, i.e., the bleaching is reversible and the recovery happens very fast. It is reported that the exciton and thus the pump-induced reflectivity has a lifetime of only 0.9 ps.

Consequently, such a system can serve as a mirror which can be switched off by an off-resonant pump pulse and recovers after a very short lifetime. In electronic circuitry, such a device is known as mono-stable multi-vibrator, a fundamental building block of logic gates.

## 3.2 Theoretical modeling

In order to calculate the electromagnetic near-fields of the dye-metal system shown in Fig. 3.1b, a calculation in COMSOL multi-physics[com08] was set up. In contrast to the rotor system presented in chapter 2, this system can be described in an effective 2D coordinate system. This is due to the invariance in the direction along the grating wires.



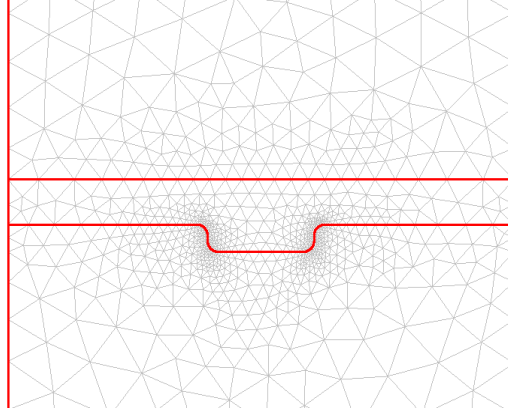


Figure 3.3: Computational mesh for the FEM calculation for the dye-grating system. The thick red lines mark the material interfaces: vacuum–polymer+dye–metal from top to bottom. The gray lines mark the actual mesh.

Such an invariance leads to momentum conservation in this direction. In particular, the geometry of the incident laser was chosen such that there is no  $\mathbf{k}$  contribution in that direction at all.

The choice fell to a FEM calculation since we found in earlier FDTD calculations that a very high spatial resolution is necessary near the metal boundaries. Here, the near-fields have strong spatial variations. In particular, the cubic mesh in FDTD calculations leads to artifacts on a length-scale of a single cube at the unavoidable staircases. The edges of the cubes act as antennas and, as such, enhance the near-field.

These effects are not a very big problem in cases where one is mostly interested in far-field properties of a system. In this case, the FDTD calculation eventually converges with finer meshes. In contrast, the very near-fields directly at the staircase do not converge at all since the artifacts remain no matter how fine the mesh is chosen.

Strong artificial field enhancements in the mesh cells very close to the interface are particularly problematic in a case like ours, where light-matter interaction is most interesting in exactly the same region. Similar problems occurred in our group with FDTD were found in a system of a sharp metal nano-tip, where the field induced electron emission from the tip was calculated. There, the fields were calculated with FDTD and then used as input to the time-dependent SCHRÖDINGER equation. The electron emission tended to appear preferably from the FDTD staircase artifact, which is obviously wrong.

One could argue that a real system has a surface roughness where one also expects near-field enhancements at the summits of the surface and that this could well be approximated by the FDTD staircases. This argument is invalid. First, we talk about experiments with surfaces carefully prepared with state-of-the-art methods. AFM and SEM images of such surfaces proof that they are almost atomically flat. A mesh-size of atomic length-scale is numerically impossible for real world applications. Second, a

real surface roughness is random, whereas the staircases are periodic. In general, the coupling strength between diffraction orders is governed by the FOURIER coefficients of the scatterer shape. In a staircase situation, there are few very large coefficients due to the periodicity. Thus, coupling tends to be strong and selective which is not the case for a random surface.

In a FEM calculation, space is discretized in terms of tetrahedra (triangles in 2D). In addition, a so-called unstructured mesh can be used. This means that the tetrahedra may have different sizes and orientations. This allows us to have a fine spatial resolution in exactly those positions where we expect the fields to vary fast. In other areas, e.g., the vacuum layer the mesh can gradually be coarsened. In consequence, we obtain a mesh that nicely describes the desired shape of the structure and is just as fine as necessary in the vacuum layer (see Fig. 3.3). Another advantage of FEM calculations is that they calculate expansion coefficients of a polynomial basis. In contrast, FDTD calculates a value (zeroth order expansion coefficient) at each point. Higher-order polynomials allow to correctly describe rapidly changing solutions with surprisingly few grid-points.

In contrast to the finite-differences time-domain calculations presented in the former chapter, the FEM calculations presented here were performed in frequency domain. It should be mentioned that this is just a choice and not a restriction of the method. FEM calculations can also be performed in the time domain. In particular, discontinuous GALERKIN time-domain (DGTD) methods which recently attract lots of popularity are time-domain FEM calculations[HW08, BKN11].

In our particular dye-metal system, we are interested in spectra to compare with the experiment. Also, the material properties like the dispersion of the metal and absorption spectra of the dye are given as experimental tables in frequency domain. These parameters can easily be put into a frequency domain FEM solver.

The actual structure consist of three blocks (rectangles in the quasi 2D calculation) of metal. On top there is the dye-polymer material filling the gap and giving a smooth surface. It is constructed by a BOOLEAN operation of a rectangle and the shape of the metal. The whole system is covered by a vacuum layer, which is thick enough to obtain far-field information. The vacuum layer is followed by a source plane, where oblique plane waves are excited. Then follows a thick PML layer and a perfect electric conductor (PEC) boundary condition. To the left and right, there are BLOCH-periodic boundary conditions matched with the angle of incidence of the source. They care for the phase difference of the oblique incoming wave at the left and right border. At the very bottom of the system, i.e., in the metal, there is another PEC boundary condition. This should be a good approximation since the fields do only enter the metal as far as the skin depth. For the weak remaining fields, a perfect metal boundary is a very good approximation to a thick real metal layer.

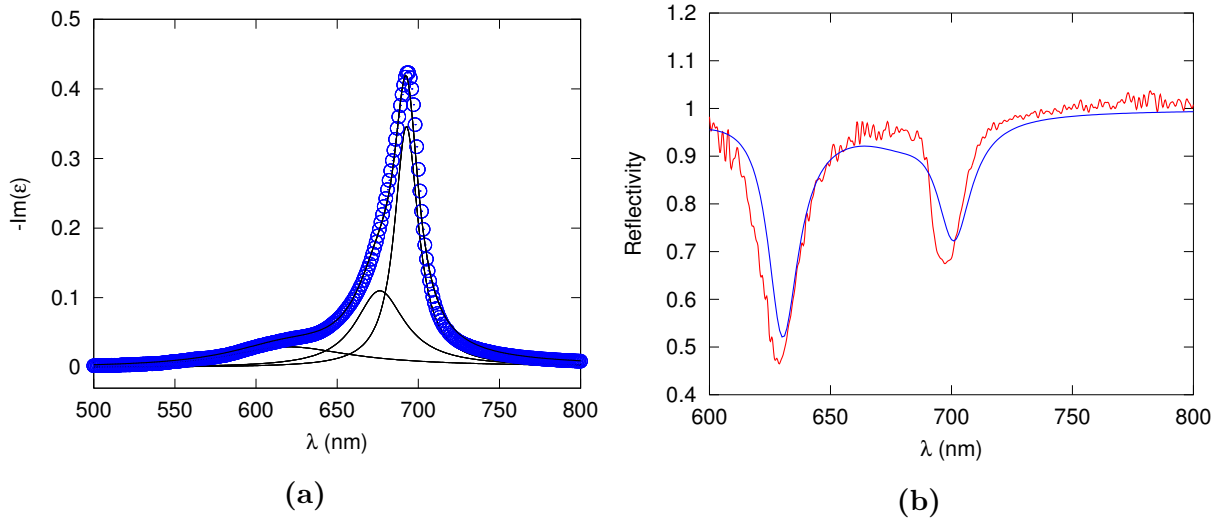


Figure 3.4: **(a)** Fit of three LORENTZian resonance curves (solid lines) to the experimental values of the extinction of the dye. **(b)** Experimental (red) and calculated (blue) spectra for the grating – dye system at an angle of incidence of  $\theta = 21^\circ$ . The thickness of the dye layer, and a global factor in the dye resonances were the free parameters that were varied in order to get the right positions and relative heights of the two resonance dips.

For the dispersion of the gold, we chose a standard fit[VGM<sup>+</sup>05] to the experimental values of JOHNSON & CHRISTY[JC72]. For the dye, we use an absorption spectrum taken from a reference experiment where the dye+polymer solution was spin-coated onto a bare flat gold surface. All the other parameters were as in the actual experiment. In fact, we did not directly use the experimental values but fitted them with three LORENTZian resonance curves and took values from these.

The absorption experiment only gives us the shape of  $\epsilon(\omega)$  while the magnitude remains undetermined. In her bachelor thesis, Sabine Auer pointed out that the possible values of this magnitude are restricted by demanding the KRAMERS-KRONIG-relations to be fulfilled[Aue11]. We chose this magnitude to be a free parameter in the model, which was later determined by comparison with the experiment. This has several reasons. First, the magnitude is related to the concentration of active dye-molecules in the matrix. This number is unknown since, among other reasons, some molecules in the experiment become inactive because a part of them is irreversibly destructed by the laser. In addition, the thickness of the layer was not known exactly. It could only be approximated by an AFM profile of a scratch down to the metal. Unsurprisingly, a scratch in this soft sticky material only allows for a rough estimate of 10 nm.

Both, the film thickness and the magnitude of  $\epsilon(\omega)$  have a strong influence on the strength of the effects in the far-field reflectivity (small factor in  $\epsilon \rightarrow$  few excitonic absorption). Also both shift the relation of excitonic and plasmonic contributions to re-

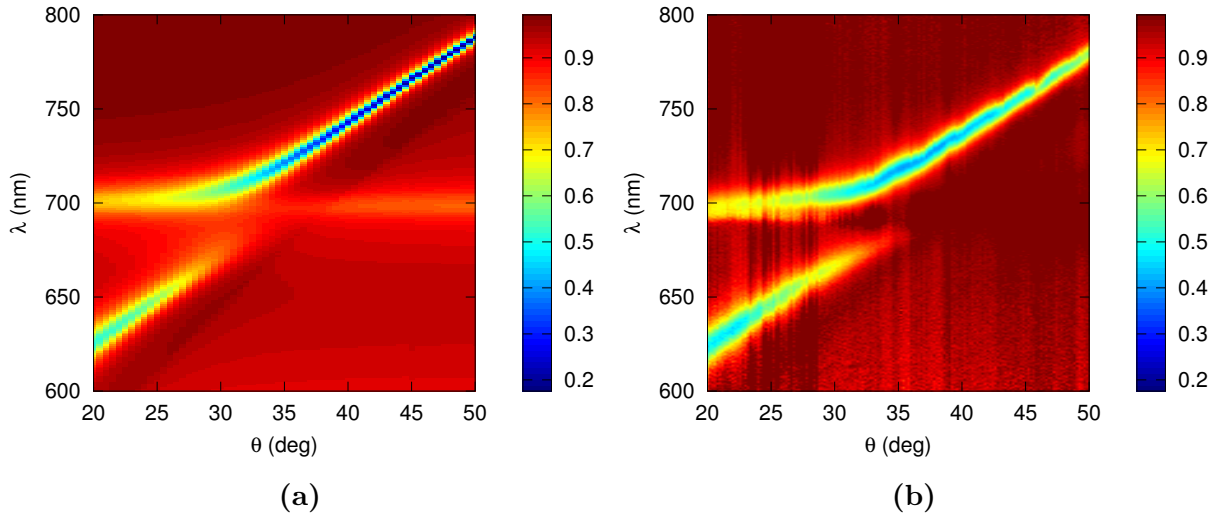


Figure 3.5: Panel (a) shows the calculated angle-dependent reflectivity spectrum for the dye-grating system. The experimental data is shown with the same color-scale in panel (b). The latter is the same data as shown in Fig. 3.2b but with a different color-scale.

flectivity (thicker layer  $\rightarrow$  more excitonic absorption). The film thickness also shifts the position of the SPP resonance. This is clear if one approximates the polymer-layer and the vacuum as an effective medium with some refractive index. This effective refractive index is higher if the layer is thicker. Since the background refractive index enters the SPP dispersion, the resonance is shifted.

In Fig. 3.4a, the imaginary part of the permittivity  $\epsilon$  deduced from the experiment is shown as circles. The sharp and high exciton-related absorption peak at 685 nm is obviously the dominant contribution. With the bare eye one can find that there are at least two side peaks. One shoulder at 670 nm manifests itself in an asymmetric shape of the line. Another broad shoulder is found near 610 nm.

Having these observations in mind, we modeled our  $\epsilon(\omega)$  as a superposition of three LORENTZian resonance functions and fitted them to the experimental data by non-linear curve fitting. The result of the superposition is shown as thicker black line in Fig. 3.4a which is hardly visible since it follows the experimental data very well. The three contributing peaks are shown as thin black lines and match the expectation. Note that the absolute value of the imaginary part of  $\epsilon$  still depends on an overall factor as discussed above.

Having the materials and the shape (see Fig. 3.3) of the system, the calculations quickly show the most important features, such as the avoided crossing in roughly the right position. In order to match the experiment also quantitatively, we had to fit our free parameters to the experiment. These parameters are in particular: the background refractive index for the dye solution, the thickness of the dye  $d$  and the factor describing the strength of the absorption.

On this purpose, we considered a single spectrum, namely that for  $\theta = 21^\circ$  and varied the free parameters until the calculated spectrum matched. The best fit we found is shown in Fig. 3.4b. Its parameters as indicated in Fig. 3.1b are the grating period  $a = 430$  nm, the depth of the slits  $h = 20$  nm and the thickness of the dye measured from the top of the nano-wires  $d = 25$  nm. Since we used rounded corners for the nano-wires, as can be seen in Fig. 3.3, we had also the curvature radius  $r = 8$  nm as parameter. The substrate made of gold was  $1 \mu\text{m}$  thick. On top of the dye, we had to calculate a  $3 \mu\text{m}$  thick layer of vacuum in order to collect far-field data. In the upper, direction we had two  $400$  nm PML areas on top of each other. The background refractive index for the dye solution was  $n = 1.3$ .

In Fig. 3.5, it can be seen that fixing the parameters at a single angle suffices to obtain a result which agrees very well with the experiment even quantitatively over the whole range of wavelengths and angles. Some differences occur due to various processes which were not considered in the modeling. In particular, there are nonlinear effects even in the so-called linear experiment. These effects are, e.g., the degeneration of the dye due to the laser and the difference of the thickness of the dye on a grating and flat metal. Such a difference is quite plausible since the grating may well have some influence on the spin-coating process.

### 3.3 Results with alternative geometries

The previous section presented results of calculations that are in excellent agreement with experiments. Of course, such results stand at the end of a development process with several intermediate model designs. The reader may find it entertaining to read this section about some intermediate models, the physical interpretation of their imperfections and how they inspired the modeling process.

In the first modeling, we used a perfectly rectangular shape. The angular-resolved reflectivity of such a system without the dye resonance is plotted in Fig. 3.6a. One can see a nice sharp SPP resonance at the correct position where it is also found in the experiment. For very short wavelengths one can also see the absorption cutoff of gold at  $550$  nm. Up to here, the calculation looks perfectly correct.

In Fig. 3.6b, the reflectivity of the same system is shown with the dye resonance implemented. For wavelengths longer than  $700$  nm, the result looks similar to the experimental findings. We see the lower polariton (LP) branch which is bend to avoid the crossing with the non-dispersive reflectivity dip at the dye resonance at  $\approx 700$  nm.

In the short wavelength range, the spectrum looks totally different. The upper polariton (UP) branch is almost invisible. Instead, there is an additional deep non-dispersive reflectivity dip. Our first speculation that something was wrong with the material model

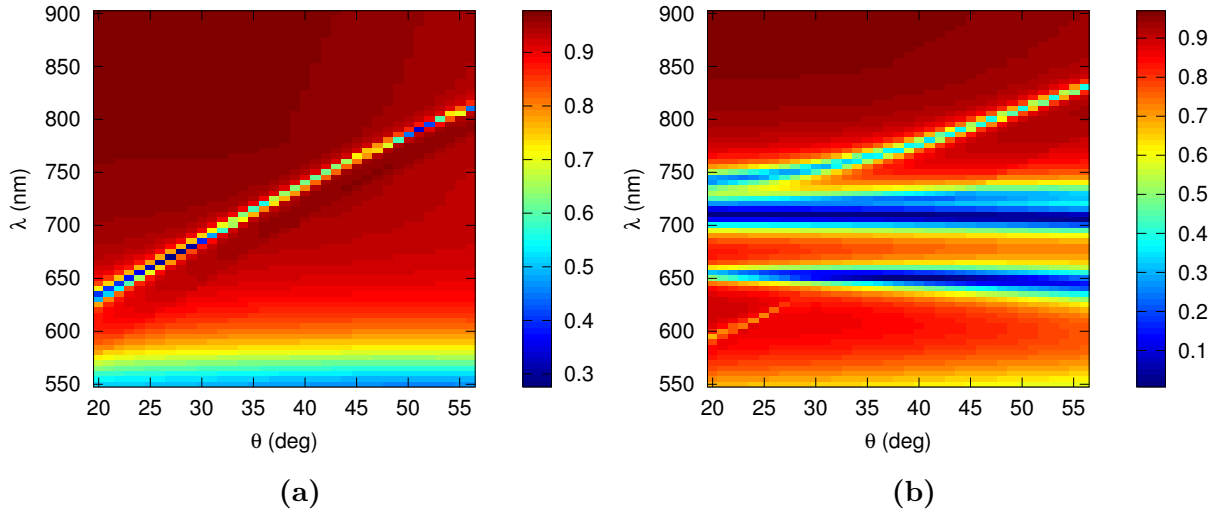


Figure 3.6: Angular resolved reflectivity spectrum in a system with perfectly rectangular slits but otherwise parameters from the experiment. **(a)** shows a grating without a dispersive coating. A nice sharp SPP can be seen that is in well accordance with the experiment. **(b)** shows the grating with the j-aggregate material model. Along with the SPP and the exciton line near 700 nm, a single slit localized surface plasmon mode is visible as non-dispersive broad reflectivity-dip at 650 nm. The latter mode is not found in the experiment where the slit-shape is also not perfectly rectangular.

for the dye could easily be ruled out by calculations with the dye on a flat surface. These looked perfectly correct.

Looking at the field distribution in the mysterious reflectivity dip, we found strong fields localized in the slits and not traveling along the surface. Conclusively, we are dealing with a standing-wave mode which is related to the single slits. Such a mode is comparable to the 0D plasmon modes found at metallic nano-particles sometimes called localized surface polaritons (LSPs). They differ qualitatively from SPPs which are waves transporting energy along a surface.

The mode “suddenly” occurs in Fig. 3.6b and is not found in Fig. 3.6a since the dye material changes the refractive index and thus dramatically influences modes whose mode volume almost completely overlaps with the dye-material. This holds still true for modes which are far off the dye-resonance. In contrast, the actual SPP as seen in Fig. 3.6a is only slightly influenced by a change in the refractive index of the dye-layer. An explanation is that dye-layer is very thin and most (in terms of volume) of the SPP-related near-field enhancement is in the vacuum anyway.

An interpretation is that we slightly changed the refractive index in a nearly perfect box-cavity resonator (the slit) and thereby brought one of its resonances into our view. The resonance energy and the quality factor of such a resonator sensitively depends on the dimensions of the rectangular slit. Thus, one could shift the resonance out of Fig. 3.6b

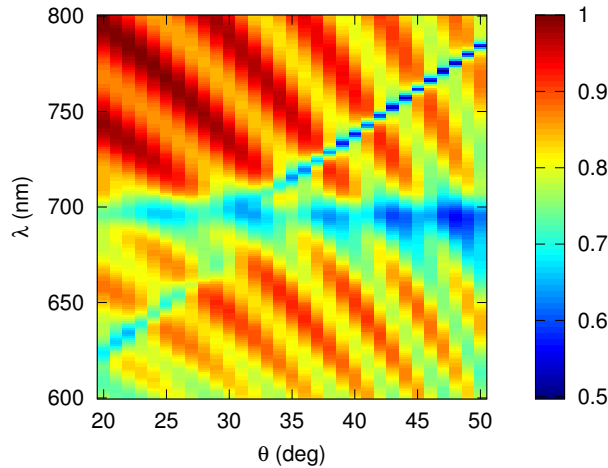


Figure 3.7: Spectrum of a dye-grating system overlaid with a Fabry-Perot artifact. The dye related reflectivity dip and the two plasmonic branches are still visible. The artifact is induced by a bad numerical mesh at an vacuum-vacuum interface.

at will. This would of course restrict us in our choice of the slit depth and width. Also, the fact that there is no such resonance in the experiment is a hint that this is the wrong way.

The quality factor, and thus the strength of the effect of the cavity resonance is only limited by the absorption and numeric errors in a theoretical calculation. The situation in an experiment is completely different. Here, the quality of the resonator also depends on how exact one is able to craft a rectangular slit.

Since the sample is a nano-structured device, we expect the slit-shape to be not perfectly rectangular. Thus, we tried different shapes in order to suppress the spurious mode. Triangular shapes gives similar slit modes as reported in Ref. [SB09]. Such resonances are also in disagreement with the experiment. Finally, we ended up with a rectangular shape with rounded corners as shown in Fig. 3.3 where the spurious resonance is completely suppressed.

Another kind of artifact is visible in Fig. 3.7. The whole spectrum is superimposed with a bunch of broad dispersive resonances. Their magnitude is much weaker than the magnitude of the SPP and exciton related reflectivity dips but still very annoying.

It quickly became clear that this artifact looks like the spectrum of a FABRY-PEROT (FP) interferometer, i.e., a resonator consisting of two parallel reflective planes. It remains the question which planes are to be blamed for the problem.

From the fact that the resonances are not very sharp and the magnitude is quite small, one can conclude that the FP interferometer creating the artifact has a quite small finesse. This means that either the reflectivity of the planes is small or the absorption between the planes is high.

The first idea was that one of the reflective planes is the gold surface and the other

plane is the perfectly conducting (PEC) boundary condition behind the PML layer. This is quite probable since the PML does absorb much but never everything. So we could have built a Fabry-Perot resonator with an absorbing material inside.

This thesis could easily be checked taking into account that one can easily tune a FP by changing the distance of the planes. In fact, this is what one usually does if one has bought a FP interferometer. Disappointingly, after making the PML thinner and consequently decreasing the Au-PEC distance, the spectrum did not change at all. At least, we learned that the PML is thick enough.

Another probably reflective plane to be ruled out is the vacuum-PML interface. Even though literature reports various problems with PML implementations, a reflective front face is not among them. Slightly shifting the vacuum-PML also gave no result at all.

Now there was only one plane remaining in the simulation area: an interface between two vacuum-layers. They remained from earlier convergence checking where multiple PML layers were tried. The lowest PML-layer ended up as an unsuspecting vacuum layer. In fact, shifting the vacuum-vacuum interface shifted the Fabry-Perot spectrum and was thus identified as the second reflector.

The reason it was reflective was a bad setting of the mesh at the boundary. The grid-points on both sides of the interface were not exactly adjacent. An additional line calling `meshinit(fem,'hmax',50e-9)` solved the problem in future versions of the COMSOL model.

These two subtle artifacts serve as typical examples of obstacles one is faced with during the process of modeling. Such errors are not as bad as getting no solution or a totally wrong solution but are quite hard to debug. This is due to the fact that not the numerics is wrong but the wrong physics is put in.



# Chapter 4

## Localization of light

### 4.1 Localization in wave physics

Motion and consequently transport is the heart of physics. The main objective of different branches of physics is the description of transport of different entities, most prominently energy and particles. Often, transport can be described in terms of waves such as sound waves, electromagnetic waves and SCHRÖDINGER waves. The observable quantity is often an intensity, i.e., the time-averaged squared absolute value of the field occurring in the wave equation.

#### 4.1.1 Interference

An interesting phenomenon related to waves is interference, i.e., the superposition of two or more waves. The superposition of coherent waves with different phases gives rise to interference patterns. In the case of two waves  $u_1$  and  $u_2$  the resultant intensity reads

$$\|u\|^2 = \|u_1 + u_2\|^2 = \|u_1\|^2 + \|u_2\|^2 + \underbrace{u_1^* u_2 + u_2^* u_1}_{\text{Interference}}. \quad (4.1)$$

Amplitudes sum up and it occurs a signed term that causes interference effects.

In actual physics, interference gives rise to such spectacular effects as the colors of soap bubbles or whispering galleries in cathedrals. Interference patterns such as NEWTON-rings make small length differences visible such that interferometry is today's standard for high-resolution length measurements.

The occurrence of interference is an important difference between wave-like and diffusion-like transport. Both, wave-functions and solutions to a diffusion equation (e.g., a concentration of a chemical substance) allow for linear superpositions. In contrast to the waves, nothing spectacular happens when two concentrations overlap. Only the “amounts” (amplitudes) sum up while there are no phases playing a role.

In wave-related physics, one is often interested in scattering, i.e., what happens when a wave hits an obstacle. The scattered wave can be thought as a superposition of plane waves traveling in different directions. Obviously, scattered waves can interfere with each other and with the incident wave and again form interesting patterns in the intensity.

If many waves are superimposed, the intensity reads

$$\|u\|^2 = \sum_i \|u_i\|^2 + \sum_{i,j>i} \Re(u_i^* u_j). \quad (4.2)$$

Here, the interference term is a sum over many signed numbers. If these numbers are independent random numbers, it is very likely that they add up to zero. In this case, interference effects vanish and the superposition becomes diffusive (in the sense that only amplitudes sum up). In everyday life, the effect can be seen in the “diffuse” light on cloudy days or the noise in a lecture hall before the lecture begins. In the first case, light from the sun is multiply scattered at droplets in a cloud and hits the ground from all directions with different phases. In the second case, the observer measures waves from many sources at different positions emitting independent signals. In both cases, the intensity distribution is quite homogeneous: there are no focal spots.

To appreciate the complexity of these phenomena, remember the difference of people chatting and a skilled choir singing in a lecture hall. In contrast, the background noise of chatting people can be pleasant compared to an unpracticed choir where all the emitters are slightly detuned and drifting out of phase. To conclude that: very different results can occur in closely related setups as soon as multiple scattering or many emitters enter the scene.

### 4.1.2 Focusing light: common and uncommon ways

In some cases, the interference term can become very high at certain positions. Well known examples are the focus of a parabolic mirror or a convex lens. Figure 4.1 shows the spatial intensity distribution created by point sources that are arranged on a parabola, i.e., an approximation to HUYGENS principle for the parabolic mirror. At the focus point, the interference term takes a very high value and dominates the intensity.

This technologically highly relevant effect is absolutely impossible for diffusive motion. There is no way to arrange sugar crystals (sources of concentration) in water such that the sugar concentration obtains a distinct maximum at a point outside the crystals.

Parabolic mirrors and convex lenses obviously have a very special geometry. The focusing effect can be easily understood in the limit of ray optics. The named techniques to focus light were known since the classical antiquity. It may be speculated that they were used to start fires by focusing sunlight. Intensity enhancements in certain geometries are very common in technologies such as directional microphones and antennas.



Figure 4.1: **(a)** Intensity of 51 spherical wave emitters (covered by gray circles) arranged on a parabola. The intensity of each emitter decays fast as  $1/r^2$ . The intensity in the parabola stems almost exclusively from the interference term. The frequency is chosen such that a nice interference pattern occurs. For high frequencies, the intensity concentration in the focus becomes much more pronounced such that the intensity becomes negligible everywhere except in this single spot. This can also be seen from comparison with **(b)**, where the same situation is shown with the interference terms left out.

Another particularly fascinating way to enhance the intensity at a certain point is a point defect in a so-called photonic crystal. A photonic crystal is a periodic arrangement of scatterers having a photonic band-structure, i.e., for given momentum only light with discrete energies can travel through the crystal[JVF97]. Even more important, there are energy regions where no modes are allowed to travel at all. These regions are called photonic band gaps[Yab93] due to their similarities to band gaps in solid-state physics. If one has a point defect with a point emitter such as a quantum dot, light at energies in the bandgap is trapped at the position of the defect[Yab87]. Photonic crystals play an important role in basic research such as cavity QED[YSH<sup>+</sup>] where light is trapped between BRAGG mirrors.

In addition to the named geometries, metal structures provide another way to concentrate electromagnetic waves. One well known example are lightning rods. With nano-structured metal, surface plasmons can be excited that were the topic of the previous chapters. The mobile electrons in the metal oscillate resonantly driven by the incoming field and serve themselves as a source of electromagnetic radiation. The very strong fields close to the metal surface can be used sensitively probe the chemical environment of the metal. On the one hand, the resonance frequency of the SPP sensitively depends on the refractive index of the surrounding. On the other hand, the strong near-fields promote strong light-matter interaction. The latter point makes it possible to detect single molecules in surface enhanced RAMAN spectroscopy[NE97] or to coherently couple them to excitons as discussed in the previous chapter.

All the named structures have in common that the wave has high intensity in small

spatial regions. On this reason, the wave is often said to be “localized”.

A very different approach to obtain high intensities in a small spot is localization of light by multiple scattering: Consider a wave-packet (e.g., an electron beam or a pulse of laser light) that travels through a medium containing scatterers in a homogeneous anisotropic matrix. Then parts of the wave-packet are scattered into all directions when they hit a scatterer. Such parts can then travel through the matrix and are again scattered into all directions.

From this argument, one would expect the probability density function of real wave vectors  $\phi(\mathbf{k})$  to spread with time. While all intensity in the initial beam was concentrated to a single  $\mathbf{k}$ , all allowed wave vectors are equally contributing to the field after infinite time. The magnitude of  $\mathbf{k}$  is restricted by the dispersion relation in the matrix. Consequently, this first approach predicts that after an infinite number of scattering events,  $\phi(\mathbf{k})$  is constant on a sphere defined by the dispersion relation and zero everywhere else. This means that the original narrow beam is equally scattered into all directions.

This can actually be seen in a simple experiment where laser light is shot into diluted milk. If the milk concentration is sufficiently high, the light is visible as a glowing ball and nothing remains of the original laser beam. It seems like the light is injected at some point and spreads out from there (like the concentration of a chemical). The directional information is lost, which is untypical for the beam of a laser pointer. The named points motivate the usage of the term “diffusion” for this sort of transport.

In similar situations, a surprising and counter-intuitive phenomenon occurs: the localization of waves by multiple scattering, that was first discussed by P.W. ANDERSON in 1958. In this seminal paper he describes “[...] a simple model for such processes as spin diffusion or conduction in the ”impurity band.””[And58, abstract] and proves that, under certain conditions, the diffusion completely breaks down. This means that there are circumstances where waves that are multiple scattered by randomly arranged scatterers stops to move. The waves becomes trapped in a certain region and exponentially vanish out of that region. Since the intensity is concentrated to small spatial regions, this effect is an uncommon way to focus waves. The rest of this chapter will discuss ANDERSON localization and, in particular, the localization of light in a specific nano-structure.

### 4.1.3 Examples of localization of classical waves

ANDERSON localization is well established for the motion of electrons in solids and there was great success in experimentally testing its predictions[Gan05, Sto01, LGP88]. As an example, a disorder-dependent metal-insulator transition can be observed in phosphorus doped silicon[RMP<sup>+</sup>83].

There are also several experiments in lower-dimensional systems. For example, it was found that the conductance of thin metal wires decreases exponentially as temperature

goes to zero[GWP79, Tho77]. It was ruled out that the effect is related to a bulk property of the metal or the KONDO effect. For one-dimensional systems such as thin wires, the theory predicts that all eigenfunctions are localized[AALR79]. The conductivity is given by hopping processes among the localized states. At low temperatures, there is not enough activation energy for hopping such that the conductance vanishes.

In order to observe localization of classical waves<sup>1</sup> in an experiment, one needs scatterers with a size scale around the wavelength[She90]. The scattering should be strong meaning that the propagation velocity in the matrix and the scatterers should be as different as possible. Also, the experiment has to be constructed such that the relevant quantities such as the intensity of the wave and transmission coefficients can be measured as directly as possible.

Microwaves are particularly well suited to study multiple scattering of classical waves. A main advantage is that the wavelength of the microwaves can easily be chosen in the range from millimeters to a meter. Thus, the whole experiment can be scaled to an easily manageable desktop size. The frequencies in the range of hundreds of MHz to hundreds of GHz allow to directly resolve the temporal evolution of the fields with contemporary electronics.

Microwaves can be excited and detected by small probes containing inductors and capacitors. Even in the earliest electrodynamic experiments, HERTZ had detectors much smaller than a wavelength at his disposal[Her88]. The scatterers can be made of dielectric materials or metal and can be easily placed at will.

In several 2D microwave experiments, cylindrical scatterers are placed between parallel (super-) conducting plates[DAS<sup>+</sup>91, LLS<sup>+</sup>07]. In Ref. [DAS<sup>+</sup>91], it is reported that the scatterers were randomly placed onto half of the sites of a square lattice. Thus, this experiment can be thought as a photonic crystal with point defects. In a transmission setup, a wave is excited at one front of the chamber and the transmission is detected at the opposite front.

In the transmission spectrum Fig. 4.2, a high number of sharp peaks can be seen along with a low-frequency modulation. The low-frequency modulation is a relic of the photonic band structure of the unperturbed photonic crystal. The occurrence of bands of strong/low reflectivity (stop/pass bands) can be easily understood as BRAGG reflexes. They occur where waves reflected by different crystal planes interfere constructively/destructively. The bands are washed out compared to the unperturbed crystal but can still be seen because the cylinder positions are restricted to the square lattice such that there is still some long-range order.

---

<sup>1</sup>Evidently, a phenomenon which is mostly explained by the wave character of the electrons can also be expected in other – non-electronic – systems. Some authors rigorously restrict the term “Anderson Localization” to electronic waves. However, we have the connotation of multiple independent scattering events leading to universal behavior as formalized by the single-scaling hypothesis.

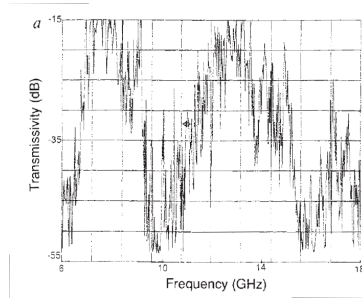


Figure 4.2: Transmission spectrum of microwaves scattered from a random distribution of dielectric cylinders. The low frequency modulation is attributed to the band structure of the unperturbed photonic crystal. The sharp peaks are the localized modes; from Ref. [DAS<sup>+</sup>91]

It is argued that few (3-4) localized modes contribute to each of the sharp peaks. These modes can be separated by selectively damping them by placing water filled capillaries at high intensity positions.

In a further setup, the frequency was locked to one of the smaller peaks and the spatial distribution of the electric energy was measured by rastering a microwave probe through the chamber. At one particular mode, it can be seen that most of the energy is concentrated in a cluster of few (6) peaks and the energy distribution is quickly decaying from this cluster. This finding is a major hallmark of a strongly localized mode. It was also found that the modes having their peaks in the center of the chamber are less attenuated from the damping of the chamber boundaries. At frequencies where multiple modes are found, each peak can be attributed to a certain mode by placing the water capillary into the peak position. Then, the other peaks of the same mode are also damped whereas peaks of other modes are unaffected.

In a similar experiment, dielectric cylinders are placed at random positions only restricted by a given filling fraction and minimum distance into a microwave cavity [LLS<sup>+</sup>07]. Consequently, no traces of photonic crystal physics can be found here. The inner in-plane boundaries consist of microwave absorbing foam in order to mimic an open system. In this setup, fields are excited by a point source and detected by a point detector. Transmission spectra can still be taken for a fixed source and detector position. The transmission spectrum clearly shows a stop band between 3.5 and 5.7 GHz. The stop band is found in between two single-cylinder MIE resonances.

Localized modes show up as sharp solitary peaks in the transmission spectrum. The sharpest peaks are found at the edges of the stop band. This is exactly the position where the MIE cross section changes fast. This is in well accordance with an argument discussed in the related paper Ref. [VS05]. Here, it is stated that strong localization is to be expected near the single scatterer resonances where the scattering cross section

is moderately enhanced. In contrast, at resonance, the scattering cross-section highly exceeds the physical size of the scatterers such that the optical volumes overlap. In this case, multiple scattering breaks down and the situation is better described in terms of propagation through an effective medium.

Intensity maps of various modes are shown and compared to FDTD calculations using the same scatterer distribution as the microwave[LLS<sup>+</sup>07, Fig.3]. All major modes from the experiment are also found in the calculated spectra. The intensity distributions are also very similar. This finding is somewhat surprising since the calculation disregards losses in the dielectric and small differences in the scatterer distribution. This shows that the localization effect including the spectral positions and spatial structure of the eigenmodes is quite robust against perturbations.

In Ref. [HSP<sup>+</sup>08], ANDERSON localization in a 3D elastic network is demonstrated. On this purpose, aluminum beads are brazed together such that the beads are in direct mechanic contact. Waves are excited by a point source on one end of the system and transmitted intensity is measured on the other end. The setup is chosen such that absorption is compensated in the results.

As in the microwave experiments, a succession of stop and pass bands is found in the transmission spectra. These bands are not attributed to periodicity but to eigenmodes of the individual scatterers.

In a time-resolved experiment, it is found that transmitted intensity decays exponentially at low frequencies. At high frequencies, the decay is significantly slower than exponential. The spatial intensity distributions show strong fluctuations with high distinct intensity peaks in the high frequency case. At low frequencies, the pattern shows much weaker fluctuations and follows a RAYLEIGH distribution as typical for diffusion<sup>2</sup>. The authors interpret their findings in the high frequency case as strong evidence for ANDERSON localization of ultrasound[HSP<sup>+</sup>08].

The scattering strength is often discussed in terms of a comparison of the mean-free path  $l$  and the wavelength  $\frac{2\pi}{k}$ . It is interesting to note that the authors give value of  $kl = 1.6$  for the low-frequency case and  $kl = 1.8$  for the high-frequency case. This is in contradiction with the often cited statement that the onset of ANDERSON localization occurs at values  $kl < 1$  or at least at small values of  $kl$ . Here, localization is found exclusively at the higher value of  $kl$ . The  $kl \approx 1$  criterion is also strange in the point that  $kl$  has the unit of an angle. However, it is clear that something interesting happens where wavelength and mean free path are on the same order of magnitude. The latter qualitative statement is exactly what is claimed in the often cited paper Ref. [IR60] by IOFFE and REGEL.

---

<sup>2</sup>The terminology concerning intensity distributions and their relation to diffusion is discussed in Appendix A.2

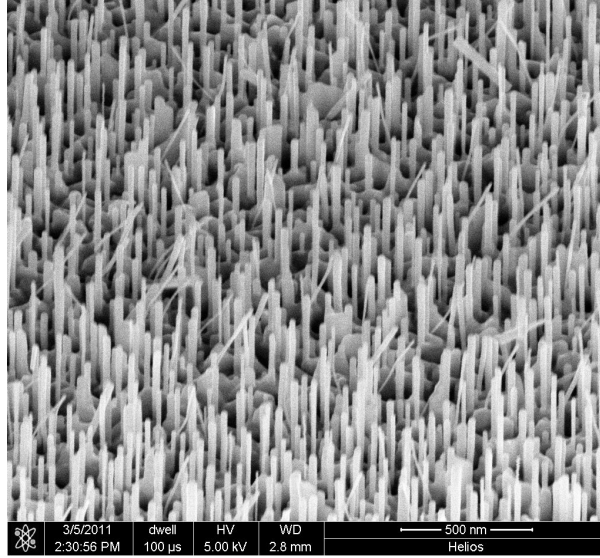


Figure 4.3: SEM image of the ZnO nano-needle sample used in the experiment. The needles are randomly distributed and vertically aligned. The needle-diameter is  $\approx 50$  nm. The needles are grown on a sapphire substrate. There is a rough layer of ZnO beneath the needles (mostly occluded in this image).

## 4.2 Localization of light in ZnO nano-needle arrays

In contrast to microwaves, localization of light is much harder to observe. In the optical range the wavelengths are on the scale of a micron. Consequently, optical experiments on multiple scattering need nano-structured samples. Temporal resolution can only be achieved with complicated interferometric setups. Near-field optical microscopy is a quite new technology and has several limitations.

Inspired by experiments in the LIENAU group, we discuss a sample of randomly distributed ZnO nano-needles that are densely packed but almost non-overlapping and vertically aligned. Since ZnO has a high index of refraction of  $n \approx 2$  one expects strong scattering and, in particular, multiple scattering in this system.

The needles are grown on a sapphire substrate using a metal-organic vapor-deposition method[KYOY08]. As shown in the SEM image Fig. 4.3, the needles have a diameter of  $\approx 50$  nm and a length of up to  $0.5 \mu\text{m}$ . It can also be seen from the SEM image, that there is a rough ZnO underground beneath the needles.

A major obstacle in observing wave localization is the localization itself. Localized waves are different from usual waves in the fact that they do not travel. Consequently it is impossible to project them onto a screen or other far-field detectors. As already mentioned, localization is often observed indirectly. One possible method are transmission experiments. The idea is that the localized waves are not transmitted and thus missing in transmission spectra. Transmission experiments are the natural way to observe local-



ization in electronic systems. The quantum mechanical wave function itself in the bulk of a material can hardly be observed. Instead the localization of electrons can be observed as “missing” conductance.

In microwave experiments, it is possible to measure the electromagnetic near-fields directly since probes are available that are very small compared to the wavelength and fast compared to the frequency. This is not the case for optical experiments. The smallest available optical probes are fiber tips in near-field scanning optical microscopes. They can be much smaller than a wavelength but have the inherent disadvantage that the tips are connected to relatively thick fibers. Thus, only the near-fields on a not too rough surface can be resolved. In more complicated structures, it is mechanically impossible to position the fiber tip to the region of interest.

The nano-needle forests discussed here are obviously three dimensional and the localization that is to be observed will occur in between the nano-needles. This is a region where one cannot place a probe, e.g., a fiber tip. On the other hand, the needles have the advantage that one can look into the structure from above. The interesting region is not occluded by the structure itself. This is a main advantage over the powders discussed in Ref. [WBLR97].

To detect the localized field, one could place luminescent molecules in between the needles or – more elegantly – use the ZnO rods themselves. The latter is possible by second-harmonic generation (SHG). It is well known that ZnO nano-structures have a high SHG efficiency[Mil64]. At positions where the light is localized, the field in between the needles is very strong and, consequently, the SHG is high. The fact that the SHG is proportional to the square of the field strength makes it a sensitive probe for intensity fluctuations. For the generated second-harmonic light, the conditions for localization are not fulfilled. Consequently, it is radiated into the far-field and can be detected there.

The LIENAU group utilized an ultrafast second-harmonic microscopy setup to collect the second-harmonic light and eventually to investigate the scattering properties of the sample.

As source, an ultrafast ultrabroadband laser was used. It created pulses of down to 6 fs FWHM centered around 800 nm. It spanned a bandwidth of more than 200 nm. The light was focused using an all-reflective CASSEGRAIN objective to a diffraction limited spot-size of 500 nm. The sample-surface was rastered through the focus of the objective in order to collect spatially resolved reflectivity spectra.

The reflected light was collected with the same objective and filtered such that only light with wavelengths around 400 nm can enter the further stages. This light, which is generated by nonlinear processes in the sample, is then analyzed with an interferometric frequency-resolved auto-correlation (IFRAC) setup[3]. The nonlinear emission consists of second-harmonic (SH), higher-harmonic and light emitted by other nonlinear processes

such as multi-photon-induced luminescence. How photo-luminescence and SH emission are distinguished in the experiment is discussed in Ref. [SMS<sup>+</sup>10].

As the name IFRAC indicates, the pulse is superimposed with a time-delayed copy of itself (interferometric auto-correlation (IAC)) to obtain information about the temporal evolution of the emitted field[SS05]. The resolution is mainly determined by the pulse length, i.e.,  $< 6$  fs. If the auto-correlation is performed spectrally resolved, not only the temporal evolution of the field, but also the temporal evolution of the spectrum of the emitted light can be observed. Having this setup, one can not only collect spatially resolved reflectivity spectra, but even analyze *when* the light is emitted and *how long* it remains in the sample.

The experimental result of such a measurement is an IFRAC trace. It contains the spectrally resolved count rates from the spectrometers CCD chip in dependence of the time-delay of the two excitation pulses. The count rate is proportional to the IFRAC intensity  $I_{IF}(\omega, \tau)$  where  $\hbar\omega$  is the energy and  $\tau$  is the time delay. It is the intensity of the FOURIER-transformed second harmonic electric field  $E_{SH}(t, \tau)$ :

$$I_{IF}(\omega, \tau) = \left| \int E_{SH}(t, \tau) e^{-i\omega\tau} dt \right|^2 . \quad (4.3)$$

The incident field consists of a pulse and its time-delayed copy  $E(t) + E(t + \tau)$ . The non-linear signal is emitted by the polarization of the material induced by this field. For a single monochromatic source, the polarization in frequency domain can be expanded into a series of powers of electric fields as

$$P_i = \epsilon_0(\chi_{i,j} E_j + \chi_{i,j,k}^{(2)} E_j E_k + \chi_{i,j,k,l}^{(3)} E_j E_k E_l + \dots) \quad [\text{Hec09}] . \quad (4.4)$$

The second term in the series gives rise to the second-harmonic generation. The susceptibility tensors  $\chi^{(n)}$  are material properties and inherit important symmetries from the material. Obviously, higher order terms only contribute for strong fields.

From MAXWELL's equation  $\nabla \times \mathbf{H} = \dot{\mathbf{D}} + \mathbf{j}$  and the definition of the electric displacement  $\mathbf{D} = \epsilon_0 \mathbf{E} + \mathbf{P}$ , it is obvious, that  $\dot{\mathbf{P}}$  mathematically acts as a source in the same way as a current  $\mathbf{j}$ : the second-harmonic polarization is the source of second-harmonic emission which can then be detected in the far-field. If we assume that the incident field oscillates at frequency  $\omega$  as  $\cos\omega t$ , we find that the first (linear) term in equation 4.4 oscillates at the fundamental frequency. In the second term, we obtain the two contributions  $\cos^2 \omega t = 1/2 + 1/2 \cos 2\omega t$ . The first does not oscillate at all and is known as optical rectification. The second oscillates at twice the fundamental frequency and is known as the second harmonic. Similarly, the third term  $\cos^3 \omega t = 3/4 \cos \omega t + 1/4 \cos 3\omega t$  gives a contribution at the fundamental and the third harmonic at three times the fundamental frequency. In our case, only the second harmonic light reaches the detector since everything else is filtered out by a band pass filter in the optical setup.

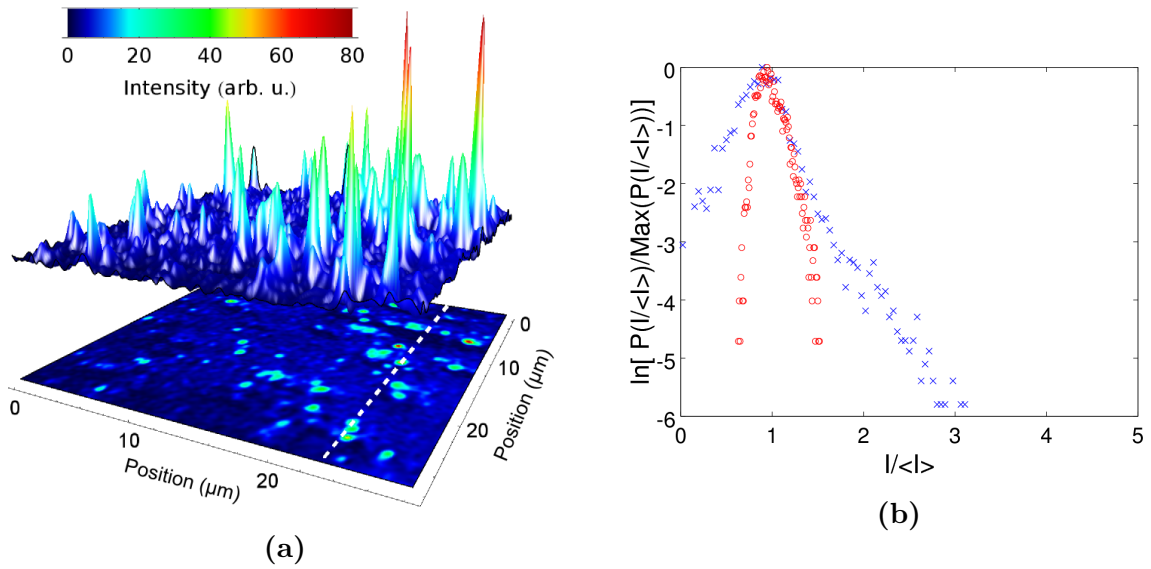


Figure 4.4: **(a)** The intensity of the second harmonic emission as measured by rastering a ZnO nano-needle sample with the second harmonic microscope. There are strong spatial fluctuations and, in particular, high peaks referred to as hot-spots. **(b)** Blue crosses: histogram of the intensity distribution indicated by the measurement presented in **(a)**. Red circles: histogram of the intensity distribution of a sample with rough ZnO without needles. The intensity distribution of the nano-needle array is highly asymmetric and has an extended tail at high intensities. This corresponds to the enhanced probability of exceedingly high intensities in a localized wave-function.

By carefully analyzing the IFRAC trace  $I_{IF}(\omega, \tau)$ , the temporal evolution of the fundamental field can be reconstructed[SS05, SMS<sup>+</sup>10]. In the experiments in the LIENAU group, this was used to obtain the lifetime of the near-field in between the needles at each position while rastering the ultrafast second-harmonic microscope over the sample.

The experiments with the named ZnO nano-forest samples and second-harmonic IFRAC microscopy reveal that the electromagnetic wave-functions in the sample share the following similarities with the electronic wave-functions known in ANDERSON localization:

- The experiment reveals strong spatial fluctuations of the second-harmonic emission. In particular, there are hot-spots, i.e., regions of enhanced emission which are smaller than the resolution of the experiment, i.e., smaller than 500 nm diameter. The spatially resolved SH emission is shown in Fig. 4.4a. This spatial distribution is quite similar to the wave-functions found in disordered 2D quantum-systems[Run03]. An example from a disordered quantum well discussed in Ref. [Run01] is shown in Fig. 4.5 for comparison.
- The intensity distribution is highly in-homogeneous. There are ridges of high in-

tensity accompanied by extended regions of low intensity. The spatial intensity distribution has no obvious relation to the underlying dielectric distribution. Particularly, the wave-functions look fractal-like.

- To quantify the last point, one can look at the statistics of the wave-function amplitudes. In Ref. [Mir00, Chap. 4], the distribution of the amplitude in a localized 2D quantum system is predicted to be log-normal ( $P(u)$  like  $e^{-\ln^2 u}$ ) whereas it is exponential-log-cube ( $P(u)$  like  $e^{-\ln^3 u}$ ) in 3D systems. In all cases, the amplitudes of the localized wave-functions are distributed highly asymmetric with extended tails at high amplitudes. These tails correspond to the fact that there is a finite probability to find points with a very high amplitudes, i.e., hot-spots. Thus, the statistics of the amplitude distribution is a sensitive tool to evaluate the hot-spot density and strength. Figure 4.4b shows the amplitude histogram for a sample with a rough base layer of ZnO and a sample with ZnO nano-needles. It can clearly be seen that there are extended high intensity tails only for the system with nano-needles. These tails correspond to the fact that there is a finite probability to find points with very high amplitudes, i.e., hot-spots.
- The lifetime of the near-field at the hot-spot positions is significantly enhanced over average positions. This is an indication that the light is trapped in the sample and multiply scattered for a surprisingly long time[3].

These findings indicate that, indeed, the light is localized in the ZnO nano-forest.

### 4.3 Calculations

Even with the strong experimental indications, the interpretation that we deal with localized light can be questioned. To provide further evidence, we performed theoretical calculations for model systems. Counterarguments could be that the experimental findings might be induced by dirt particles or in-homogeneously grown nano-structures. These can be fended if calculations show that there are strongly localized electromagnetic near-fields. In theoretical models, one has perfectly clean materials and controlled nano-structures.

To calculate the electromagnetic field distribution in the ZnO nano-forest, we first had to model the geometry. For the most important part, namely the placement of the individual nano-needles, we created dense, random arrangements of (almost) non-overlapping circles. On this purpose, two approaches were implemented. First, a simple molecular dynamic code of repelling hard-circles was implemented and run to minimize the overlap of a given number of circles in a given volume. A totally random distribution of circles was chosen as initial arrangement. With this approach, we obtained very high

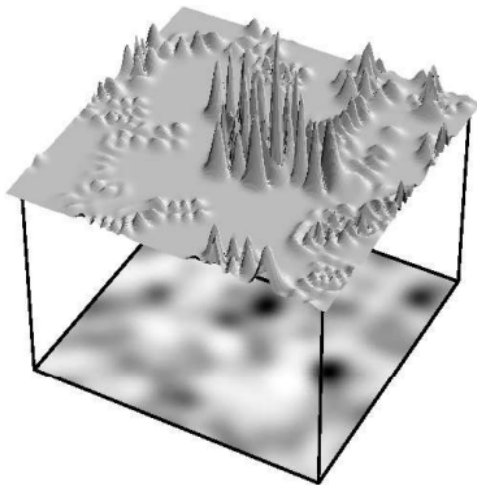


Figure 4.5: Two dimensional wave-function of electrons in a disordered quantum well. The probability amplitude  $\Psi^*\Psi$  is depicted as surface plot and the random potential is indicated by a gray-scale map. Distinct maxima in the probability amplitude form a ridge-like structure surrounded by extended regions of vanishing probability amplitude; from Ref. [Run01]

quality arrangements on high numeric cost. In particular, this approach yields densely packed 2D crystals if the density of circles is chosen very high. However, we rated this approach as too expensive.

Our second, much faster choice is the following method: First we create a matrix of random numbers. These random numbers are convoluted with a (GAUSSIAN) filter function which gives a random surface having a correlation length given by the bandwidth of the filter-function. The result is smooth random landscape with a typical distance of hilltops. By the size of the matrix and the variance of the filter, we can control the number of hills in the resulting matrix. We then take the positions of the hilltops as centers of our circles. Given the number of hilltops and the desired density of circles, we finally calculate the real-space volume the circle-array corresponds to.

This second approach guarantees a typical distance of circles but does not exclude the possibility of overlapping circles. This fact is not a disadvantage of this approach since we find in SEM images that there are also some overlapping needles in the actual sample.

A second important ingredient into electromagnetic field calculations is the material model. ZnO is a wide-bandgap semiconductor ( $E_g \approx 3.3$  eV) having very interesting optical properties in the ultraviolet range. At excitation energies higher than the bandgap, ZnO becomes strongly absorptive since an electron-hole plasma can be excited. The absorption edge is very steep, even at room-temperature. As a particularly interesting effect, (random) lasing in the ultraviolet was reported in various ZnO nanostructures[KWH11, CZH<sup>+</sup>99, FDS<sup>+</sup>09, HMF<sup>+</sup>01, ZDY<sup>+</sup>06].

In our case, the excitation, as well as the modes which are to be observed, exist in the red to near-infrared spectral range. Here, the absorption is very small and the dispersion relation is flat and a commercial ZnO wafer looks as transparent as glass to the bare eye. Taking this into account, we model the ZnO as a dielectric material with a constant refractive index  $n = 2.0$  and no absorption at all. These assumptions are further justified by the fact that the light will only travel through the ZnO for a very small distance.

### 4.3.1 Challenges

Since the computational capacity is limited, it is not feasible to calculate a system with a size comparable to the actual sample (several  $\text{mm}^2$ ). The fact that the experiment utilizes a focused laser beam gives a hint on which size scales the interesting physics happens. The focal spot has a radius of  $\approx 0.25\mu\text{m}$ . In consequence, a calculation of this size should be sufficient to reproduce the experimental results. However, the major point of the experiment are the fluctuations from laser shot to laser shot while rastering the focus over the sample. Thus, we need many calculations of the focus size in order to compare them as in the experiment. The most natural way to achieve this is to choose a region bigger than the focus size. The alternative would be to perform many calculations of independent regions of the focus size.

We can also see from the experiment, that there are regions of  $\approx 5 \times 5\mu\text{m}^2$  that contain only weak field enhancements (see blue regions in Fig. 4.4a). To make it likely to find strong enhancements in the calculations, we need calculations on this scale. If we chose much a smaller region, we could be in a region without hot-spots by bad luck.

In all cases, we can not compare the number or height of hot-spots in the calculation with some region in the experiment. Such quantities are not well defined due to the random nature of the system. Even averages of these quantities are not of high reliability since we only have on the order of 10 hot-spots in the experimental region.

Instead, we can compare distributions of the near-field intensities producing histograms as Fig. 4.4b. These distributions are close to ensemble averages and are similar for different realizations of the random system.

The system considered in this chapter is huge in the in-plane directions due to its random nature. The sample wafer has a size of (several  $\text{mm}^2$ ) which is very large compared to the scale of the individual structures ( $\approx 10\text{ nm}$ ). Taking the small focal spot size into account, it is reasonable to consider the in-plane extension as infinite: the boundaries of the sample have no influence on the experimental results. From a computational point of view, we have to restrict ourselves to finite systems. At the boundaries, we have to impose boundary conditions to solve MAXWELL equations. This is a basic principle in solving partial differential equations where a well posed problem has to be constructed. Well posed means that the solution exists, is unique and stable with respect to small

perturbations[BSMM01, Sect. 9.2.3.1]. If one of these conditions is not fulfilled, the system is ill posed and there is little hope to find a sensible numeric solution.

The list of boundary conditions that are well suited for MAXWELLS equations is quite short: The simplest are perfect electric conductors (PEC) where  $\mathbf{n} \times \mathbf{E} = \mathbf{0}$  and perfect magnetic conductors (PMC) where  $\mathbf{n} \times \mathbf{H} = \mathbf{0}$  and  $\mathbf{n}$  is the boundary normal vector. There are several approaches to construct open boundaries and, last but not least, periodic boundary conditions.

A choice for boundary conditions that mimic infinite domains with a finite computational cell are periodic boundary conditions. Since our random system is not periodic, such conditions do not look very natural at a first glance. However, if we use unit cells that are large enough, i.e., contain many needles, periodic boundary conditions are a very good choice compared to other realizations.

Perfect conductors are reflective and light cannot leave the calculation area in the in plane directions, which is very different from the experimental situation. Open boundaries allow such in plane propagation, but light leaving the calculation area is lost. In the experiment, a portion of the light leaving a reference area can be scattered back from needles that do not belong to that area. With periodic boundaries, light scattered out of the calculation cell “sees” randomly arranged needles as in the experiment.

Such an approach of using huge unit cells in conjunction with periodic boundary conditions is called a super-cell approach. We can learn a lot about the artifacts we have to expect by making a detour to computational material physics where super-cells are very popular[Dro05]. Here, materials are considered in the technologically highly relevant case where the crystal periodicity is broken by (very few) defect atoms. It is easily understood that a calculation with a super-cell that is much larger than the extension of the defect states makes good predictions for a single defect. If the super-cell is too small, electrons feel the presence of the defect in the neighboring cell which is obviously an artifact. In this case, the defect states delocalize and form a band-structure in contrast to the discrete defect levels that are to be expected at a single defect. The formation of the defect band-structure is closely related to the fact that the super-cell ansatz makes the defects periodic, which is in contrast to the random nature of the placement of defect atoms.

Similarly, in the case of light, the super-cell approach may introduce artifacts since some randomness is lost and replaced by periodicity. This can be even worse compared to electronic systems since light is known to be more difficult to localize. As in the electronic system, a photonic band structure forms. The good news is that the artifact modes can easily be identified since they are extended all over the super-cell. One argument for this statement is that they have a well defined momentum  $\mathbf{k}$  since they belong to a band-structure. It follows from the uncertainty principle of FOURIER-transformation, that they are widely spread in real space. A second distinction is that these are modes traveling in

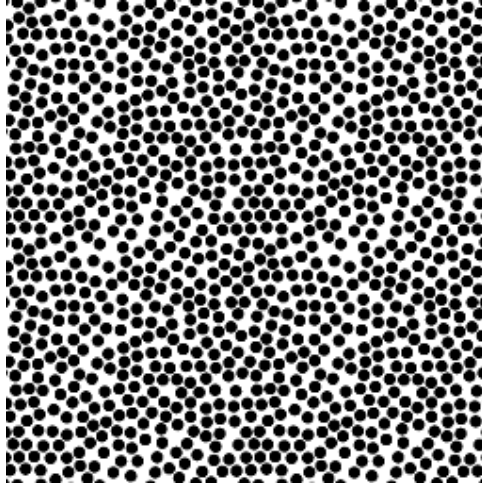


Figure 4.6: Four tiled unit cells including many cylinders to illustrate the super-cell approach applied in the calculations. The fact that the pattern is repeated is hardly visible even though humans are known to be extremely good in pattern recognition. This is an intuitive indication that periodicity related artifacts are negligible in our system.

a certain direction from cell to cell. Thus, they do not have nodes in their time-averaged intensity along their traveling direction.

In contrast, modes expected to occur due to the randomness do not necessarily travel in a certain direction (in particular they may travel along loops) and do not need to have a well defined momentum. Consequently, they are very different from the traveling modes. In the results of all calculations presented in this chapter, such artifact modes were not observed at all. A possible reason for this is that we have analyzed time-averaged intensities where traveling modes only contribute to a homogeneous background.

If we make the unit cell large enough, the field in most of the volume of the unit cell is so far away from the boundary that it is only weakly influenced by details of the surrounding [JJWM08, Appendix D].

A more intuitive but quite impressive argument for the weakness of the periodicity-related artifacts is found by taking a look at some tiles of the super-cells used in the calculations. Fig. 4.6 shows 4 tiles of a relatively small super-cell. If one would not know that there are 4 identical tiles depicted, one would hardly find it out: the 4 tiles are not very different from the whole area filled with circles of the same size and density.

Calculations with periodic boundary conditions are naturally performed in reciprocal (momentum) space. The unit cell in momentum space is the BRILLOUIN zone (BZ). Momenta outside the BZ boundaries are physically identical with momenta folded back into the BZ according to  $\mathbf{k}' = \mathbf{k} \pm m\mathbf{G}$ ,  $m \in \mathbb{Z}$ , where  $\mathbf{G}$  is a reciprocal lattice vector. Typically, one is interested in the band structure, i.e., eigenenergies corresponding to a given momentum  $\epsilon_n(\mathbf{k})$  along with the corresponding wave functions.



In our case of a super-lattice calculation, the BZ is very small, since the real-space unit-cell is huge. For this reason, there are many back-folded low-energy modes. We are only interested in a certain energy range, namely the experimental energies in the far-red. Solving for all eigenvalues up to a certain cut-off energy looks like a waste of computational effort in this case. There are eigenvalue solvers that solve only for eigenvalues in a certain energy range. In particular, eigensolvers using ARNOLDI iterations such as ARPACK[LSY09].

The mode expansion calculations presented below were performed with the freely available MIT Photonic Bands (MPB) software package[JJ01]. The MPB reference[Joh13] states that the “targeted” solver converges more slowly than an ordinary eigensolver and is generally an experimental feature. In testing with moderately sized unit-cells ( $2 \times 2 \mu\text{m}^2$ ), we found that the targeted solver did not converge at all. Direct solvers that solve for all modes up to a certain energy pose the problem that they quickly run into memory limitations.

Due to these facts, we gave up the eigenmodes decomposition calculations at quite an early stage. We found that faster progress to direct comparison to experimental far-field measurements can be achieved with 3D FDTD calculations. We could easily adopt the work from the MPB calculations by using the MIT Electromagnetic Equation Propagation (MEEP) software package for the FDTD calculations[ORI<sup>+</sup>10] which has the advantage to be mostly source-code compatible to MPB. However, eigenmode expansions are the most efficient way to find the bandstructure of photonic crystals. In the next section, bandstructure calculations for radomly placed dielectric circles are presented.

### 4.3.2 2D Mode-Expansion

The system provided by the sample is obviously three dimensional. In the direction along the needles (referred to as axial direction), there is a substrate layer, the actual needle-array and an air layer. In the plane normal to the axial direction, the system is also structured with a nontrivial distribution of a dielectric, i.e., the ZnO-needles and air. However, in the limit of high aspect-ratios, i.e., long needles, it becomes reasonable to approximate the system as translationally invariant in the axial direction.

In such a system, one can compress the inherently 3-dimensional MAXWELL’s equations into a much easier to solve 2-dimensional system, where the fields are  $z$  invariant and  $k_z = 0$  can be chosen. The equations simplify further, if we assume a dielectric, non-magnetic material. In this case, we can set  $\mathbf{B}(x, y, \omega) = \mu_0 \mathbf{H}(x, y, \omega)$  and  $D_i(x, y, \omega) = \epsilon_0 \sum_j \epsilon_{ij}(x, y, \omega) E_j(x, y, \omega)$  with the dielectric tensor  $\epsilon$ . Also in the absence of conductive materials, the current  $\mathbf{j} = 0$ . If we choose the coordinate system such that  $\epsilon$  is diagonal, the electric displacement simplifies even further to  $D_i = \epsilon_0 \epsilon_{ii} E_i$ . In this

case we find

$$\begin{aligned} \partial_y H_z &= i\omega\epsilon_0\epsilon_{xx}E_x \\ -\partial_x H_z &= i\omega\epsilon_0\epsilon_{yy}E_y \\ \partial_x E_y - \partial_y E_x &= -i\omega\mu_0 H_z \\ \partial_y E_z &= -i\omega\mu_0 H_x \end{aligned} \tag{4.5}$$

$$-\partial_x E_z = -i\omega\mu_0 H_y \tag{4.6}$$

$$\partial_x H_y - \partial_y H_x = i\omega\epsilon_0\epsilon_{zz}E_z . \tag{4.7}$$

The first three contain only electric-x, electric-y and magnetic-z while the second three contain only magnetic-x, magnetic-y and electric-z which is a manifestation of the fact that MAXWELL's equations decouple into 2 independent polarizations (sometimes called modes). The first is called p- (*p*-parallel electric) and the second is s- (*s*-senkrecht electric) polarization.

It is an invaluable simplification over the original MAXWELL's equations that we now have two uncoupled sets of three coupled partial differential equations, each describing a two-dimensional vector-field of three components.

A further manipulation, which is not necessarily a simplification is to derive a wave equation. The procedure is similar and simpler than the one presented in App. A.3. We put the right-hand sides of Eq. 4.5 and 4.6 into the left-hand side of Eq. 4.7 and obtain

$$-\frac{\partial_x^2 + \partial_y^2}{\epsilon_{zz}} E_z = \left(\frac{\omega}{c}\right)^2 E_z . \tag{4.8}$$

This is a single scalar PDE but, in contrast to the system of PDEs. 4.5-4.7, of second order. This fact can be a disadvantage in direct numerical methods, where it is common to split higher order equations into first order systems. Here, we want to apply a spectral, i.e., analytic method where this is no problem. Note that the other polarization gives a slightly more complicated equation containing the operator  $\partial_x \frac{1}{\epsilon_{yy}} \partial_x + \partial_y \frac{1}{\epsilon_{xx}} \partial_y$ . The derivations presented here can be applied to the other polarization in a straightforward manner and are thus left out.

In order to solve equation 4.8, we have to impose boundary conditions to obtain a well posed problem. The actual sample consists of a large area (several  $\mu\text{m}^2$ ) covered with billions of tiny nano-needles. Thus, it is not feasible to do calculations for the whole system. On the other hand, the laser focus used in the experiment only has a size of  $\approx 500 \text{ nm}^2$ . The important physics happens on the order of that size and calculations for an area of that size are sufficient. As mentioned earlier, we mimic the boundary condition in the experiment, i.e., "the region is surrounded by billions of other independently arranged nano-needles", by periodic boundary conditions.

In a first step, imposing periodic boundary conditions implies that  $\epsilon(\mathbf{r}) = \epsilon(\mathbf{r} + \mathbf{G}_{n,m})$ , where  $\mathbf{G}_{n,m} = n\mathbf{g}_1 + m\mathbf{g}_2$ ,  $n, m \in \mathbb{Z}$  and  $\mathbf{g}_1$  and  $\mathbf{g}_2$  are the primitive lattice vectors. Note

that the linear operator  $\frac{\partial_x^2 + \partial_y^2}{\epsilon_{zz}}$  of our equation is also invariant under translations by  $\mathbf{G}_{n,m}$ . Such operators are exactly the topic of solid-state physics[AM07] from where we can adopt the whole tool-set needed to solve the present problem.

An important ingredient is BLOCH's theorem which states that our eigenfunction  $E_{n\mathbf{k}}(\mathbf{r})$  consists of a yet unknown function  $u_{n\mathbf{k}}(\mathbf{r})$  having the same periodicity as our operator and a phase factor

$$E_{n\mathbf{k}}(\mathbf{r}) = e^{i\mathbf{k}\cdot\mathbf{r}} u_{n\mathbf{k}}(\mathbf{r}) \quad [\text{AM07, Eq. 8.3}]. \quad (4.9)$$

Here,  $n$  is the index of the eigenfunction and  $\mathbf{k}$  is a vector describing the momentum (direction) of the wave.

From these few points, conclusions can be drawn which provide the basis of the topic of photonic crystals[JVF97, Yab93, Yab87, JJWM08]. In particular, as in solid-state physics, one finds that  $\omega_n(\mathbf{k})$  consists of a band structure. As a consequence, phase velocities in a photonic crystal  $v_i = \frac{\partial\omega}{\partial k_i}$  can be very different from the speed of light in a usual material. In addition, there can occur bandgaps, i.e., ranges of energies with no matching  $\mathbf{k}$ -values. In such gaps, wave propagation is impossible. In contrast to solid-state physics, there are complete and incomplete band gaps where both respectively only one polarization is forbidden.

These considerations provide an interpretation of a possible approach to the localization of light. In Ref. [CF08] it is discussed that localized modes occur in a photonic crystal with a complete bandgap where disorder is introduced by slight displacements of the individual scatterers. Remembering that a single missing scatterer introduces a strong point-defect mode, which is strongly localized in the cavity, one may be less surprised that localized light modes can be observed in perturbed photonic crystals.

Our case is quite different from that discussed in Ref. [CF08] since there is no long-range order in our chemically grown ZnO nano-needles. Thus, our theory does not take perfect photonic crystals as a starting point. Instead, we make our unit cell at least as big as the focus in the experiment and use the periodicity just as a tool to formulate sensible boundary conditions, which is technically essential in solving a PDE.

For the further discussion, we exploit the fact that the functions  $u_{n\mathbf{k}}(\mathbf{r})$  are periodic and have the same periodicity as the lattice. Thus, we can expand them into FOURIER series

$$u_{n,\mathbf{k}}(\mathbf{r}) = \sum_{l,m} c_{n,\mathbf{k},\mathbf{G}_{l,m}} e^{i\mathbf{G}_{l,m}\cdot\mathbf{r}}. \quad (4.10)$$

In the same way, we can expand  $1/\epsilon_{zz}$  into the FOURIER series

$$1/\epsilon_{zz}(\mathbf{r}) = \sum_{l,m} \epsilon_{\mathbf{G}_{l,m}} e^{i\mathbf{G}_{l,m}\cdot\mathbf{r}}. \quad (4.11)$$

Putting these expansions into Eq. 4.8, we obtain

$$\sum_{i,j} \epsilon_{\mathbf{G}_{i,j}} e^{i\mathbf{G}_{i,j}\cdot\mathbf{r}} \sum_{k,l} |\mathbf{k} + \mathbf{G}_{k,l}|^2 c_{n,\mathbf{k},\mathbf{G}_{k,l}} e^{i(\mathbf{k}+\mathbf{G}_{k,l})\cdot\mathbf{r}} = \left(\frac{\omega_n}{c}\right)^2 \sum_{p,q} c_{n,\mathbf{k},\mathbf{G}_{p,q}} e^{i(\mathbf{k}+\mathbf{G}_{p,q})\cdot\mathbf{r}} \quad (4.12)$$

We can safely divide this by  $e^{i\mathbf{k}\cdot\mathbf{r}}$ . Multiplication by  $e^{-i\mathbf{G}_{\mu,\nu}\cdot\mathbf{r}}$  and integration over the unit cell yields

$$\sum_{k,l} \epsilon_{\mathbf{G}_{\mu,\nu}-\mathbf{G}_{k,l}} |\mathbf{k} + \mathbf{G}_{k,l}|^2 c_{n,\mathbf{k},\mathbf{G}_{k,l}} = \left(\frac{\omega_n}{c}\right)^2 c_{n,\mathbf{k},\mathbf{G}_{\mu,\nu}}. \quad (4.13)$$

This is an infinite eigenvalue equation containing an operator that looks like a convolution over  $1/\epsilon$  and  $|\mathbf{k} + \mathbf{G}|^2$ . Equations of such type can effectively be solved numerically by exploiting the convolution theorem of FOURIER transforms[JJWM08].

### 4.3.3 Results

The MPB solver delivers eigenenergies and the corresponding fields at each k-point. As mentioned before, the lowest modes are quite trivial eigenmodes of a box. The lowest modes are also those with the lowest energy and lowest momentum such that their corresponding wavelength is much longer than the needle diameter. These modes can be described in terms of a so-called effective medium, i.e., they are almost the same as the eigenmodes in a calculation with a homogeneous material with an intermediate refractive index.

The effect can be seen in Fig. 4.7a. The calculated band structures (points) are very close to the analytical band-structure of a homogeneous medium (lines). The fact that the shape of the band-structure matches that of a homogeneous medium means that an effective medium description is reasonable in this energy range. The effective index enters the slope of the bands as a factor, e.g., in  $\omega = ck = \frac{c_0}{n}k$  for the simplest band. The effective permittivity for a mixture of vertically aligned needles in a homogeneous matrix is derived in the App. A.1. The author felt the necessity to use a theory that at least accounts for the anisotropy that is to be expected for aligned needles. The fact that the numerical calculations scaled by the effective permittivities for *both* polarizations match the analytical bands so well indicates that the approximations entering the mixing rule in App. A.1 are justified in this energy range.

It can also be seen from the low-energy band-structure that almost none of the earlier mentioned super-cell artifacts occur. This means that a cell size of several hundred cylinders is sufficient to obtain reasonable results with periodic in-plane boundary conditions. In a too small super-cell, e.g., the extreme of a single cylinder in the cell, strong deviations from the homogeneous band-structure would occur: such a structure supports two incomplete photonic band gaps for the s-modes[JJWM08] which is qualitatively very different from the black lines in Fig. 4.7.

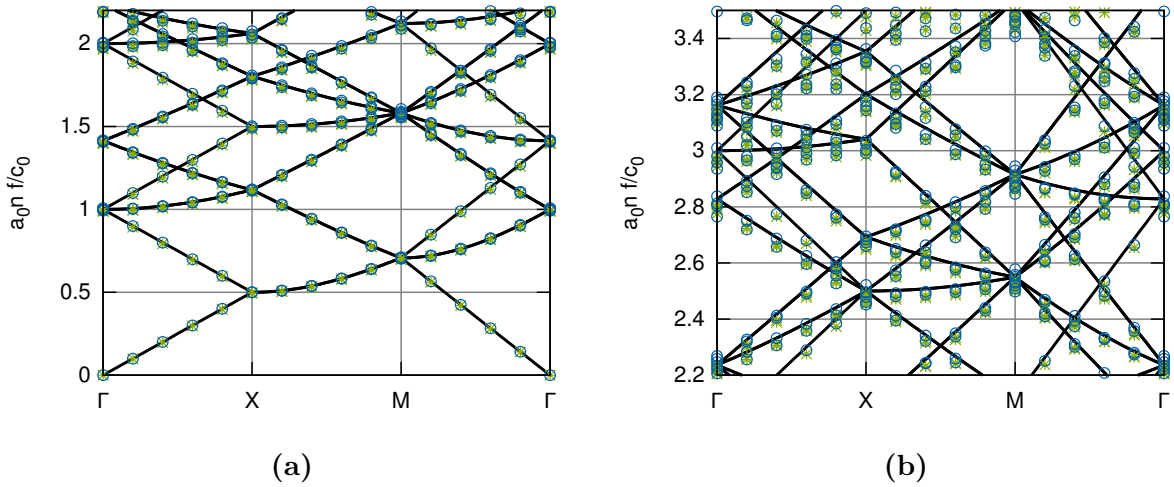


Figure 4.7: Photonic band-structure of a super-cell containing 494 cylinders with a radius of 80 nm and an refractive index of 2. The filling factor is 31.75%. Blue circles show s-, green crosses p-polarization. Black lines are the analytic expression for a homogeneous medium. All values were multiplied by the lattice constant  $a_0$  and the effective refractive index  $n_{\text{eff}}$  (different for s and p) such that a dimensionless quantity is plotted. For the low frequencies in panel (a), the points follow the analytic expression very well while considerable deviations occur at the high frequencies in panel (b).

A very sensitive measure for the deviations from a homogeneous material is whether the degeneracy of the bands is lifted or not. Most of the bands (black curves in Fig. 4.7) are degenerate. If one puts an in-homogeneous material into the unit cell, the propagation conditions for the degenerate bands become different and the bands split. By taking a very close look at Fig. 4.7a, one finds that the circles and crosses are only almost degenerate. The lifting of the degeneracy becomes stronger for higher frequencies. This can most clearly be seen by looking at the band crossings at the X-point. The difference in frequencies at the lowest crossing point can only be seen from the raw data but is too small to see in the image. At the second crossing point, it can be guessed from the figure that there are several overlapping circles and at even higher crossing points the degeneracy is clearly lifted. At reduced frequency values above unity, the lifted degeneracy can even be observed along the bands and not only at the symmetry points.

It can be concluded that the material is well described as an effective medium with an an-isotropic effective permittivity at low frequencies. This also means that there are no effects of interaction among the individual scatterers such as multiple scattering.

The opposite is true for the more interesting higher energy modes. It can clearly be seen in Fig. 4.7b that the degeneracy is lifted for all modes. This means that we now deal with an in-homogeneous material. In addition, the shape of the bands increasingly differs from the homogeneous band-structure. This means that we deal with very different

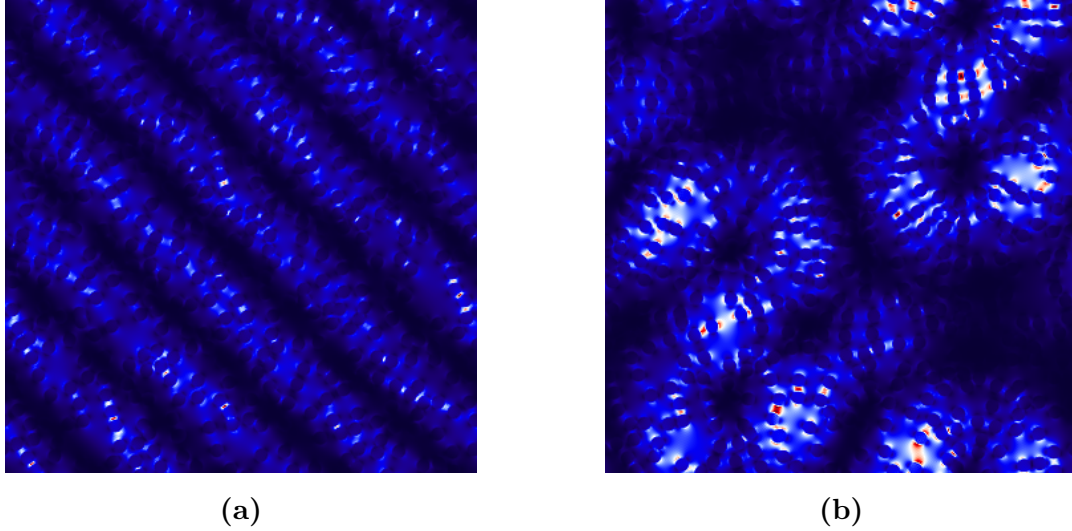


Figure 4.8: Intensity distribution of selected p-polarized eigenmodes in two-dimensional super-cells of dielectric needles. The color-scale goes from dark blue (low intensity) via white to dark red (high intensity). All modes show more or less obvious regular patterns for low intensities. These are remainders of the unperturbed plane wave solutions in a box. The high intensity values (red in the figures) are distributed in an irregular way. Note that there are only few red regions while most of the figures is blue. This means that there are very few points with exceedingly high intensities.

modes with different propagation characteristics. In this region, the limit of an effective medium becomes more and more invalid. Instead, scattering at individual scatterers, propagation to the next scatterer and scattering again becomes more plausible.

Two selected eigenmodes of a 2-dimensional array of ZnO nano-needles are shown in Fig. 4.8. A regular pattern for low intensities can clearly be seen. These patterns are close to the unperturbed plane waves in an effective medium. In addition to this background, high intensity values occur in positions that are quite ordinary in terms of needle arrangement. The highest intensities are always found in the gap in between two adjacent needles in p-polarization and in the center of a needle in the s-polarized case. The regions of high intensities always consist of a very high intensity peak and a surrounding of enhanced intensities including several subsidiary peaks.

In general, the intensity distribution is very in-homogeneous compared to what one would obtain by simple superposition of the scattered fields of the individual needles. This clearly indicates that the observed patterns are a result of the interaction among many cylinders. This is exactly the sort of effect we are looking for in the present study.

## 4.4 3D FDTD calculations

All two dimensional models with periodic boundary conditions have in common, that there are no radiative losses. Light leaving the calculation area at a boundary reenters at the opposite boundary. Thus, all the electromagnetic energy emitted by the sources remains in the calculation area forever. Obviously, this is in contradiction with the experiment, where radiation in the axial direction is very important. Here, the laser pulse enters and leaves the nano-structure via transmission and reflection in the axial direction.

As already mentioned, the experimental setup allows to probe the temporal evolution of the electromagnetic field. The finite lifetime of the mode is governed by three different processes. These are: absorption, diffusion and propagation in the in-plane direction and radiation into the out-of-plane direction. In order to reproduce the temporal aspects of the experiment, 3D calculations are mandatory.

The calculations performed here have the following setup in common. The calculation area is a cuboid with a square base aligned along the  $\hat{\mathbf{x}}$  and  $\hat{\mathbf{y}}$  axes. The size  $x_{\max}$  of the base is given by the number of randomly distributed cylinders  $N$  and the desired needle density  $\rho$ :

$$x_{\max} = \sqrt{\frac{N}{\rho}}. \quad (4.14)$$

A wide range of needle diameters and needle densities were investigated.

In the third ( $\hat{\mathbf{z}}$ ) direction, a solid block of dielectric material with the refractive index of sapphire or ZnO of  $0.4 \mu\text{m}$  was followed by the ZnO needles. This block is henceforth referred to as substrate. The needle lengths were chosen to be  $0.3 \mu\text{m}$  to match the experiment. A layer of vacuum of  $1 \mu\text{m}$  thickness followed the needles. In the evolution of the setup, an additional layer of frusta between the substrate and the needles was added. The overlap of these randomly positioned frusta is an approximation of the surface roughness seen in SEM images of the actual sample. The calculation area was enclosed by strongly absorbing PML layers in the  $\hat{\mathbf{z}}$  directions.

In the  $\hat{\mathbf{x}}$  and  $\hat{\mathbf{y}}$  directions, BLOCH-periodic boundary conditions were applied. One may wonder whether these boundary conditions allow for oblique plane-waves as source of the excitation as it was argued for the 2D mode-expansion above. It turns out that a complication occurs in time-domain calculations: The BLOCH boundary conditions enforce the field on one side of the boundary to differ from the field on the opposing boundary only by a phase factor given by  $e^{i(k_x R_x + k_y R_y)}$ . Here,  $\mathbf{k}$  is the wave-vector of the incident plane wave and  $\mathbf{R}$  a lattice vector, i.e., the size of the unit cell. An important fact to note is that  $\mathbf{k}$  is a fixed value for the whole calculation.

If a very short pulse is to be modeled, the problem illustrated in Fig. 4.9 arises.

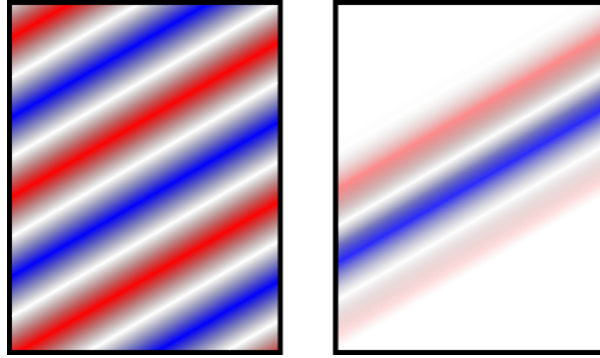


Figure 4.9: Schematic view of waves to illustrate the problem of BLOCH boundary conditions in time-domain calculations. For the very long pulse in the left panel, the fields at the left and right boundary only differ by a phase factor and obey the BLOCH condition. In contrast, the very short pulse in the right panel violates the BLOCH condition because the fields at the boundaries also differ in their amplitude.

Assume that such a pulse is emitted from current source such in a  $\hat{\mathbf{x}} - \hat{\mathbf{y}}$  plane given by

$$A_{src}(x, y, t) = e^{i(k_x x + k_y y)} e^{-i\omega t} e^{-\frac{(t-t_0)^2}{2\sigma^2}}. \quad (4.15)$$

This function obviously obeys the BLOCH boundary conditions in this particular plane. In contrast, its emitted field also has a GAUSSIAN envelope in space along its traveling direction. This obviously contradicts the BLOCH condition which state that the elongation is equal at opposing boundaries. The only exception is the trivial case where planes of constant phase and planes of corresponding BLOCH boundaries are equal, i.e.,  $\hat{\mathbf{k}} = \hat{\mathbf{z}}$  in the present case.

From another point of view, the pulse is composed of plane waves of different frequency. If one chooses  $k_x = \frac{\omega_{center}}{c} \sin \theta$  for the BLOCH boundaries, only the central component travels in the direction given by the angle  $\theta$ . The other components will travel under different angles of incidence because the dispersion relation will force them to have an  $\omega$ -dependent  $k_y$ .

A spectral-width – angle-of-incidence uncertainty relation in linear approximation can be derived as follows: the spectral-width  $\Delta\omega$  and the uncertainty in  $k$  are related by  $\Delta\omega = c\Delta k$ . In the calculation a fixed value for the Bloch-vector  $k_x$  is given. It is related to the angle of incidence  $\theta$  by  $k_x = k \sin \theta$ . From that we obtain  $\Delta k = k \frac{\cos \theta}{\sin \theta} \Delta \theta$  and finally

$$\Delta \Theta = \frac{\Delta \omega}{ck} \tan \theta. \quad (4.16)$$

The full width at half maximum (FWHM) of a GAUSSIAN pulse in frequency ( $\Delta\omega$ ) and time ( $\Delta t$ ) domain are related by

$$\Delta \omega \cdot \Delta t = \left(2\sqrt{2 \ln 2}\right)^2. \quad (4.17)$$



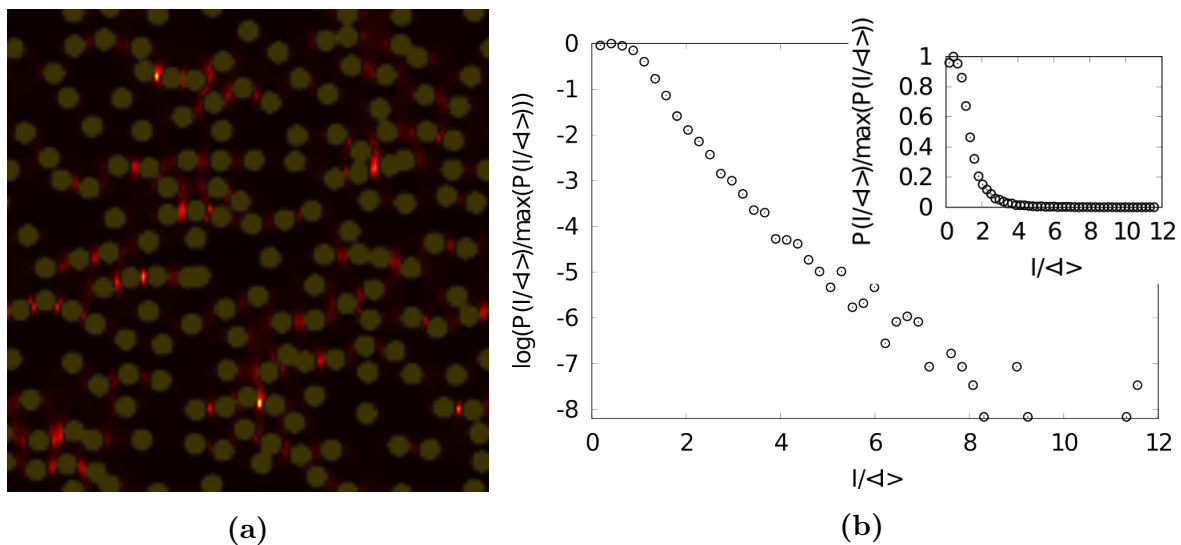


Figure 4.10: **(a)** The time-integrated squared intensity of the electromagnetic field  $|E|^2$  in an array of needles with  $0.1 \mu\text{m}$  diameter. The positions of the needles are overlaid as dark yellowish dishes. The localization manifests itself as bright hot-spots. **(b)** Semi-logarithmic plot of the histogram of the intensities. The same histogram is plotted on a linear scale in the inset.

From these considerations, it can be concluded that pulsed plane wave sources with a well defined direction are only possible for long pulses, where a single frequency dominates or for steep angles of incidence, where the  $\mathbf{k}$  component normal to the boundary is almost zero. One may consider the angle more important because of the tangent function. We use an ultrashort pulsed source with 7 fs FWHM as in the experiment but a steeper angle of incidence of  $30^\circ$  (experiment  $60^\circ$ ).

Typical values of the in-plane extension ranged up to  $5 \mu\text{m}$  with several thousand needles. As in the calculations presented in Chap. 2, this value is mostly limited due to the enormous amount of memory needed to store the fields in 3 dimensions. In the present study, a distributed memory compute cluster was used to overcome the memory limitation. In this case, the limiting factor is the network bandwidth of the inter-node communication.

## 4.5 Results

Our first FDTD calculations considered a smooth substrate and cylinders of  $0.1 \mu\text{m}$  diameter and densities of  $\approx 60 \text{ needles}/\mu\text{m}^2$ . These calculations were motivated by the SEM figures in Ref. [KYOY08]. This paper describes a two-temperature method which allows to grow fine needles  $17.7 \text{ nm}$  diameter on top of thicker needles. The paper mentions a diameter of  $100 \text{ nm}$  for the thicker needles.

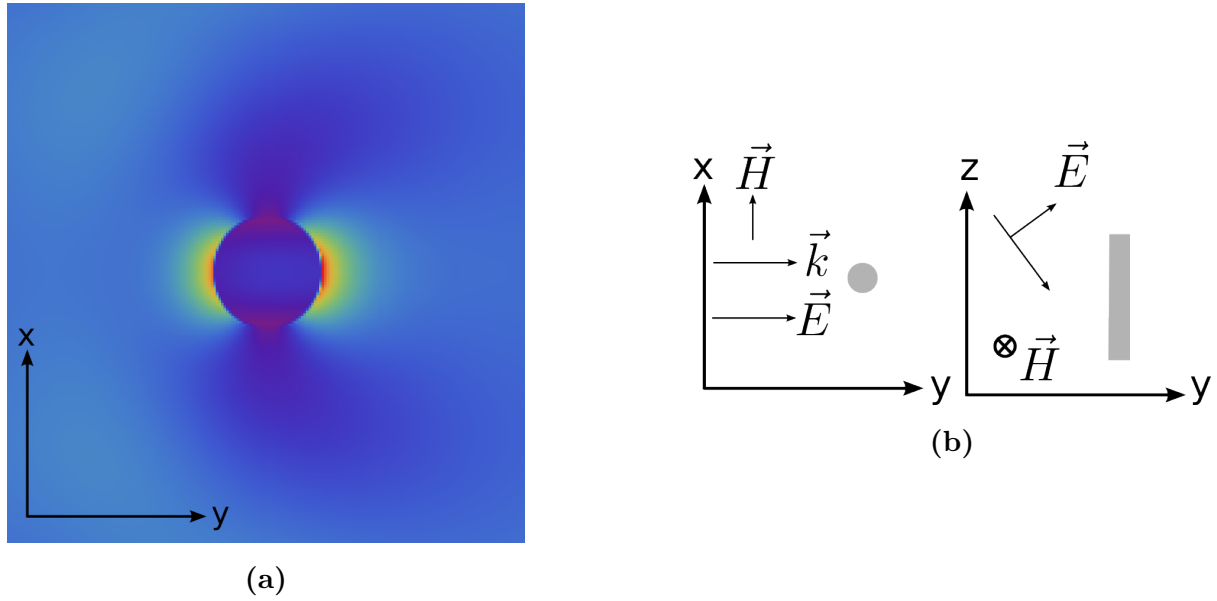


Figure 4.11: **(a)** Time-averaged intensity  $|E|^2$  around a single cylinder with a plane wave incident from the left. **(b)** Incidence and polarization setup for the calculation resulting in panel **(a)**. The cylinder is schematically depicted as shaded area.

With this geometry, we found hot-spots in the intensity as can be seen from Fig. 4.10a. Regions of high intensity with a radius of approximately 5 needle diameters occur. Each of these regions is dominated by few distinct maxima surrounded by a characteristic ridge structure connecting several needles. These ridges seem to form chains of high intensity along the direction of the source polarization vector projected onto the plane (from left to right in Fig. 4.10a).

This aspect can be understood with a simple argument arising from the boundary conditions of MAXWELL's equations. The tangential component of the electric field has to be continuous along a dielectric interface whereas the normal component jumps by the value of the difference of the permittivities. This enforces a certain form of the near-field of a cylinder with incident plane waves as plotted in Fig. 4.11a. At the upper and lower (with respect to the image) boundary of the cylinder, the electric field is tangential to the interface and thus continuous (the field vectors are given in Fig. 4.11b). In contrast, at the left and right boundaries the field is normal and has a jump. Naturally,  $|E|^2$  is enhanced where the field is discontinuous, i.e., in the direction where the field is normal to the cylinder interface which is identical with the direction of the polarization.

This quite trivial argument does not explain the height of the field enhancements but already most of the shape: the near-fields of single cylinders are directed along the polarization and the near-fields of many cylinders add up to chains along this direction. In addition, there is a complicated interaction of the near-fields that can be called multiple scattering or formation of collective modes.

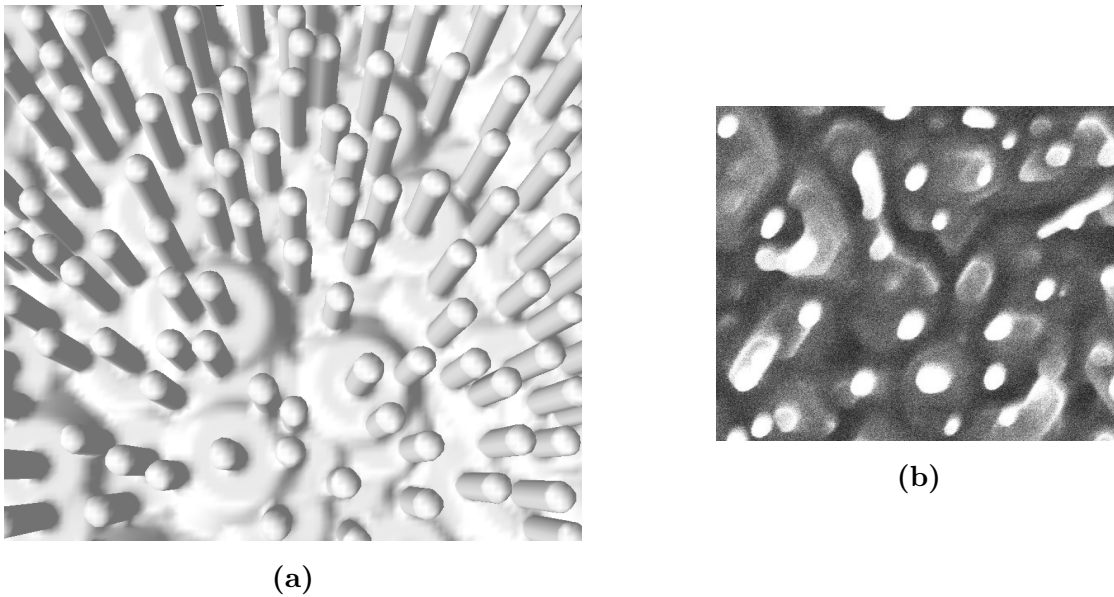


Figure 4.12: **(a)** Surface of the ZnO structure used in the calculations. In this example, the needles have a length of 300 nm, a diameter of 45 nm and a density of 120 needles per  $\mu\text{m}^2$ . Overlapping frusta model the roughness which is found under the needles in the SEM images of the actual samples. **(b)** SEM image from a similar perspective for comparison; from Ref. [3]

The size of the regions of high intensity is also in good agreement with the experimental findings. In the experiment, the hot-spot size is found to be smaller than the microscope focus of  $0.5 \mu\text{m}$ .

In order to quantify similarities in experimental field distributions deduced from the SHG microscopy and computational field distributions, we studied histograms of the intensities. As mentioned earlier, the intensity of localized fields is expected to be distributed non-GAUSSIAN and in particular to have sub-exponential tails at high intensities. These tails correspond to the few intensity peaks (hot-spots) of the localized wave.

The histogram in the inset of Fig. 4.10b looks almost like a (half) GAUSSIAN profile. The logarithmic plot reveals that the distribution decays slower than GAUSSIAN (which would look like a parabola) for higher intensities. This part is exactly the sub-exponential part which is induced by the localization related intensity concentrations.

The calculated distribution is much broader compared to the experimental histogram, e.g., in Fig. 4.4b. It is evident from the SEM images of the sample, e.g, Fig. 4.3 used in the actual experiment that the needle diameter is smaller ( $\approx 45 \text{ nm}$ ) and the needle density is higher ( $\approx 100 \mu\text{m}^{-2}$ ). These SEM images became available only after the first calculations were performed. Later calculations for needles with 50 nm diameter and a density of  $90 \mu\text{m}^{-2}$  match the experiment much better (compare Figs. 4.4b and 4.13c).

The experimental histograms have, in contrast to the calculations presented up to

here, an almost GAUSSIAN background. In these histograms, the localization induced deviations from the GAUSSIAN shape are only apparent at high intensities where they form sub-exponential tails. It was speculated that the background stems from trivial scattering off the rough underground beneath the needles. This underground can be seen in the SEM images Fig. 4.3 and even better in Fig. 4.12b. In order to check this hypothesis, we implemented a roughness in the calculation by randomly placing frusta with varying height and radius and the refractive index of ZnO onto the substrate layer underneath the needles. As can be seen by comparison of Fig. 4.12b and 4.12a, this model reproduces the shape of the background quite reasonably.

Figure 4.13c shows that this setup shows a mostly GAUSSIAN intensity distribution with tails at high intensities as in the experimental data. We can conclude that a lot of the intensity detected in the experiment was just emitted from the rough background. The actual localization contributes the high intensity values.

Later, a broad range of needle diameters and densities was studied numerically in order to gain more insight into the various dependencies. Figure 4.13 shows the near-fields for two examples having a similar overall ZnO density. The thick needles in Fig. 4.13a have near-fields that mostly look like those of single cylinders. However, taking a very close look to the background it can be seen that the system is right at the onset of forming collective modes: there are some intensity maxima in between the needles (cyan areas surrounded by blue in the image). On the contrary, the thin needles in Fig. 4.13b show strong intensity fluctuations. On a coarse scale of several cylinders, there are fluctuations in the low-intensity background (blue vs. cyan areas). On a size scale of single cylinders we note that few distinct cylinders are surrounded by very strong near-fields (hot-spots). This is in contrast to Fig. 4.13a where all cylinders have nearly the same near-field intensity.

In general, there is only a small window of needle size – density combinations that allows for the existence of localized modes. A lower limit for the needle-size and needle-density is given by the requirement of overlapping near-fields of the individual scatterers. The extension of the near-fields is given by the scattering cross-section of the cylinders<sup>3</sup>. An upper limit for the needle-density is the point where the scattering cross-sections of the individual cylinders overlap. In this case the theory of multiple-scattering becomes invalid and a description in terms of an effective-medium becomes more appropriate.

Another argument for the upper density limit can be explained in the spirit of BABINET'S principle: a very dense collection of cylinders is a sparse collection of holes. From this point of view all arguments for the lower limit can be turned around: the near-fields

---

<sup>3</sup>The scattering cross-section of a nano-structure can be much larger than its geometrical cross-section and is a non-trivial function of the needle diameter. The infinite circular cylinder which is relevant here is discussed in detail in Ref. [BH98, Chap. 8.4]

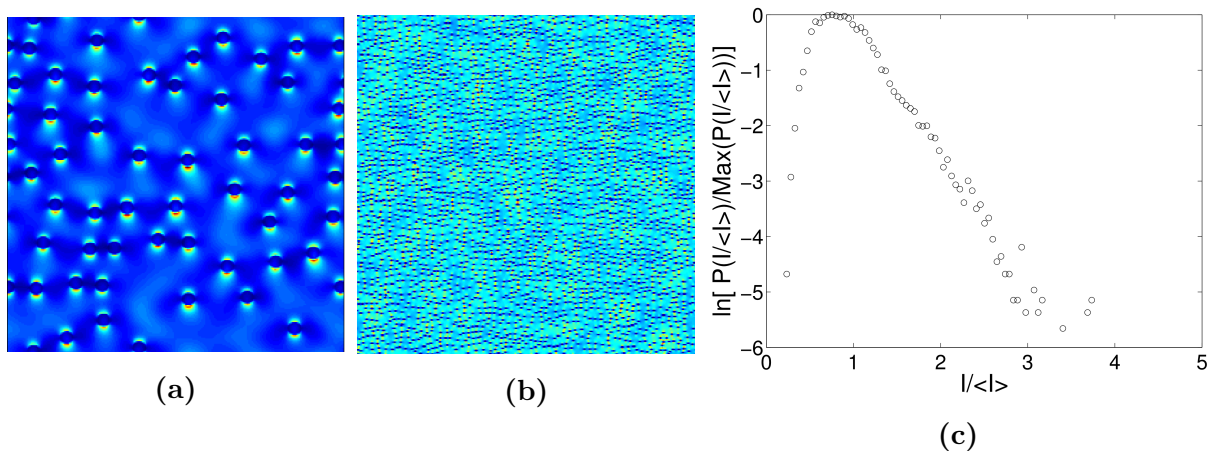


Figure 4.13: Images of the intensity as function of position in the needle-array for two very different situations with similar areal density of ZnO. Both images show an area of  $5 \times 5 \mu\text{m}^2$ . **(a)** Shows needles of 200 nm diameter and  $2 \text{ Needles}/\mu\text{m}^2$ . The near-fields of the cylinders look mostly like those of single cylinders. **(b)** Needle diameter: 30 nm,  $120 \text{ Needles}/\mu\text{m}^2$ . Collective multi-cylinder modes are formed: the intensity is in-homogeneous, the weak intensities show a “cloudy” irregular pattern (note the blue-cyan distribution) with a size-scale of many needles. Very few needles are surrounded by very intense near-fields: hot-spots start to occur (tiny red spots in the image). Panel **(c)** shows an intensity histogram for needles with 50 nm diameter and a density of  $90 \mu\text{m}^2$  on top of a rough background.

of the individual holes have to overlap to result in a collective effect such as localization. We conclude that nano-structures with intermediate filling factors have to be chosen in order to observe localization of light.

### 4.5.1 Dynamics

The FDTD calculations yield the electric and magnetic fields at discrete points in space and time. In order to obtain dynamical properties of the fields, one usually starts a calculation with all fields set to zero as initial value. After some time, fields are excited by a source. Typically the source emits only a short pulse. The calculation is run until the fields have decayed below some threshold. As in a real system, fields will eventually decay due to radiative losses and absorption.

Often, one is not directly interested in the fields as a function of space and time, but on the frequencies and lifetimes of the contributing eigenmodes. An obvious way to obtain eigenfrequencies and lifetimes is to FOURIER transform the field with respect to time. One can, in principle, fit the spectrum with damped LORENTZ-oscillators.

Practically, such a fitting approach will quite probably fail for two reasons: first, a

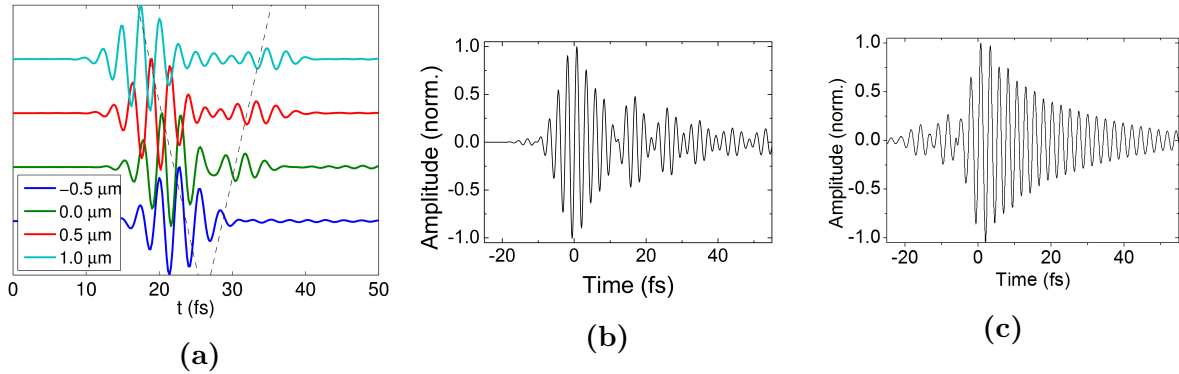


Figure 4.14: **(a)** Temporal evolution of the electric-field at different heights above the equal-length needles in the center of the calculation area. The speed of light is indicated by dashed lines. **(b)** Temporal evolution of the electric field above the needle array with randomized lengths. The directly reflected pulse is suppressed. **(c)** Temporal evolution of the near-field as reconstructed from IFRAC measurements at a hot-spot.

fit with several LORENTZians is a non-linear high-dimensional optimization problem. As such, it is complicated and there is no guarantee to obtain a meaningful solution. Second, the signal contains cutoff errors that obfuscate the spectrum.

Both problems are solved by filter diagonalization methods[MT97, Man01]. Here, additional knowledge about the functions is exploited. Namely, it makes use of the fact that we know that the function is a linear combination of exponentially decaying sinusoidals which are cutoff, before they have decayed to zero. This method can distinguish even close lying modes that occur as a single peak in the spectrum[Man03]. Using this method, the `harminv`[MT97] software package reliably yields eigenfrequencies and lifetimes from the decaying part of a given time-series.

Figure 4.14a shows the temporal evolution of the electric field at different heights relative to the needle-apex at an arbitrarily chosen in-plane position. One can mainly see the incoming pulse and a directly reflected pulse, both traveling at the speed of light as indicated by the dashed lines. There were no traces of the directly reflected contribution in the experimental data. The origin of this contribution are the flat tips of the needles, which obviously only exist in the theoretical model and not in the actual samples. As can be seen from the SEM images in Ref. [3], the tips of the needles are rounded. In addition all the needles had the same length in the model system used in Fig. 4.14a. The directly reflected contribution originates from the flat meta-material vacuum interface between the needle-tips.

In order to suppress this contribution the modeling was updated such that a small signed random number was added to the length of each needle. This way, the vacuum – meta-material interface is rough and reflection becomes much weaker. The directly

No.	relative amplitude	vacuum wavelength (nm)	lifetime (fs)
1	0.435	889.64	10.8
2	0.230	687.08	74.0
3	0.207	671.04	23.2
4	0.096	914.04	68.1

Table 4.1: Table of the most intense modes calculated from the signal plotted in 4.14b.

reflected contributions from the individual needles interfere with random phases and eventually cancel each other out.

Figure 4.14b shows the temporal behavior of the field near the tips in a hot-spot. It can be seen that the directly reflected pulse was successfully suppressed. In addition, a rapidly decaying part that was concealed in Fig. 4.14a can now be seen. This contribution comes from light which was trapped in multiple-scattering processes in the nano-needle-array for a substantial time. The modes contributing a relative amplitude of more than 5% and lifetimes (defined as  $\tau$  in  $e^{-t/\tau}$ ) as calculated by harminv are given in Table 4.1.

The experimental signal deduced from the IFRAC measurements is shown in Fig. 4.14c for comparison. It can be seen with the bare eye that this result is quite similar to the calculations. The overall decay rates are the most important aspect of these images and are comparable. The major difference is the beating pattern occurring in the calculated signal which is absent in the experiment. This difference can be explained as follows: in the experiment the system is excited by a laser tightly focused to a hot-spot. On this reason, only a single localized mode overlaps with the focal region (diameter  $\approx 500$  nm) and is observed in the experiment. On the contrary, in the calculation we excite a region of  $5 \times 5 \mu\text{m}^2$  and observe a few modes which evolve independently and eventually contribute to the beating. It can nicely be seen that the beating pattern in Fig. 4.14b is formed by modes No. 2 and 3 in table 4.1. At the beginning the beating is very strong (note the strong modulation from 5 – 25 fs in Fig. 4.14b). Later (30 – 45 fs), the beating becomes weaker since the short living mode No. 3 fades away and only mode No. 2 and the weak mode No. 4 contribute.

The extended lifetime that is evident from Fig. 4.14b and also from the experimental results deduced from the IFRAC measurements are a major hallmark for the localization of light in the nano-needle system. The electromagnetic fields are enhanced at certain spatial positions and the field stays in these position for a finite time.

This finding is one of the most astonishing points in the present work. Light stays in a certain position for a certain time which is in contradiction with the common sense that light is always traveling at the speed of light and can not be caught. In a ray optics picture, the light is still traveling but scattered multiple times at the needles. Some of the possible scattering paths are closed loops on which the light circles for a significant

time. In a wave optics picture, there are eigenmodes having intensity maxima at certain points where waves interfere constructively. Not surprisingly, such modes have a long lifetime.

In both pictures, the lifetime of the localized field is limited by radiative losses in the out-of-plane direction and diffusion in the plane. If the in-plane diffusion is diminished due to localization, one loss path is blocked and the overall lifetime is enhanced. In contrast, the out-of-plane losses are not suppressed such that the overall lifetime is still quite short. This also implies that we cannot excite and observe a wave-function completely localized in the needle-array since there is still propagation to an interface and eventually to the far-field. However, one can expect those modes that are most localized to have the smallest overlap with the air-interface and consequently to have the longest radiative lifetimes. Furthermore, generally speaking, small modes couple less effectively to outgoing plane waves. As a consequence, the long-living localized modes will dominate the physics after the short-living delocalized modes have decayed.

## 4.6 Ultrafast dynamics of localized 2D light modes

The 3D FDTD calculations reproduce important aspects of the experimental findings, such as the intensity fluctuations and prolonged lifetimes. A surprising point is that localized wave-functions are found in a system with strong radiative losses. Localization and losses contradict each other since localization depends on multiple scattering. Of course, light that leaves the system after few scattering events can not contribute to multiple scattering.

In order to further examine the influence of radiative loss onto the localization of light, calculations on a similar model with very different boundary conditions were performed[2]. Translation invariance in the axial dimension was assumed. In that model, dynamics in the axial direction is trivial and can be omitted from the calculations. In the other two dimensions, the area covered with nano-needles was surrounded by a vacuum layer which is followed by PML absorbing boundaries. In contrast to the system discussed in the previous section, radiative losses occur only in the radial directions here.

In the 2D calculation, waves were excited by a point-dipole source near the center of the needle-covered area. The aim of this procedure is to observe how the light travels through the needle covered area and is emitted into the vacuum region. Of course, we are again interested in the question whether modes showing localization are excited during this process and how they decay.

Figure 4.15 shows the electric field snapshots at two times, one at the time right after the source intensity reaches its maximum and one 5 fs later right after the pulse maximum leaves the needle covered area. Taking a coarse view on the Figure, one notes that the



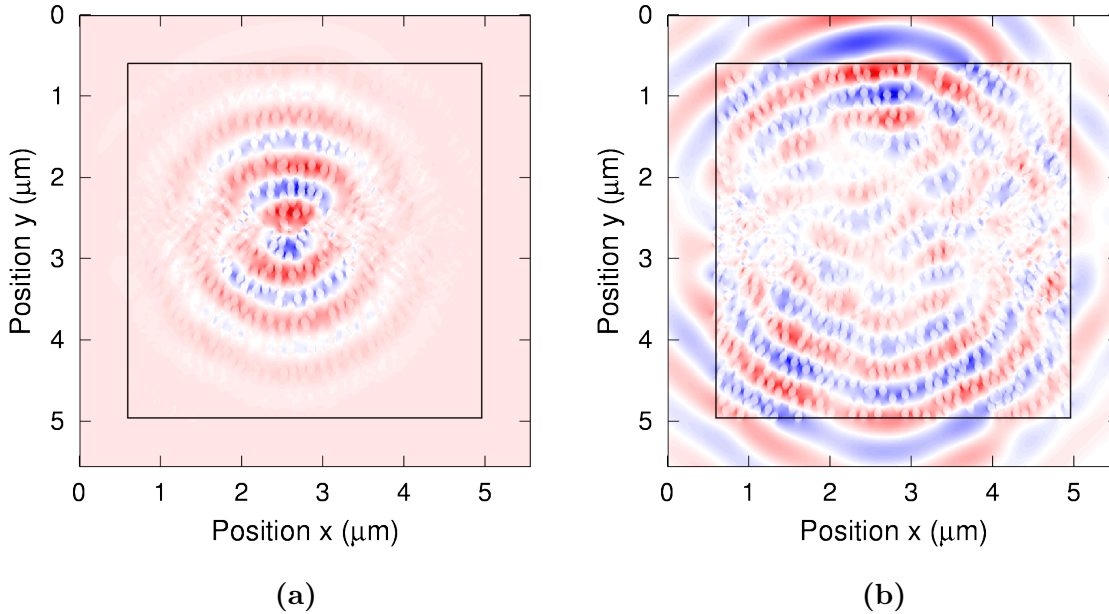


Figure 4.15: Snapshots of the  $E_y$  electric field component. The thin black square marks the region covered with nano-needles (inside) and the vacuum region (outside). **(a)** shows the field 5 fs after the intensity has reached its maximum at the source position. **(b)** shows the field another 5 fs later. This is right after the time when the maximum would have left the needle-region if it had traveled at  $0.3 \frac{\mu\text{m}}{\text{fs}}$  (speed of light in the absence of ZnO needles).

fields almost look like those of an unperturbed dipole source. In particular, the field in the vacuum region in Fig. 4.15b is almost perfectly dipolar with a small deviation that can be attributed to a square dielectric region. Such behavior can well be explained in a model where the needle region is a dielectric meta-material with some refractive index in between that of air and ZnO.

Taking a finer look into the needle region, one can see that there are some points at which the field is stronger than on average points. This holds true even for very early times such as in the snapshot Fig. 4.15a. Such points of high intensity would not be surprising if they would travel along with the pulse at the speed of light. As can be seen from time-integrated images such as Fig. 4.16b, these points are not moving at all. Otherwise they would appear as lines or at least be washed out. Instead, they are still sharp points even after time-integration.

This means that the formation of the localized modes begins at very early times. Thus we find both, extended traveling modes that are almost unperturbed by the random material and modes having strong field enhancements at certain positions at the same time in the same energy region. The coexistence of localized and extended modes

was also found in the context of ultrasound waves in a random network of aluminum beads[FSP<sup>+</sup>09] and random lasing of ZnO powders[FDS<sup>+</sup>09].

The coexistence of localized and extended modes in the current system has an interesting implication on the dynamics of the fields. Namely, the extended modes have a higher overlap with the vacuum region. This induces higher radiative loss rates as those of the localized modes. Consequently, at late times, the intensity is concentrated in localized modes whereas the extended modes already have decayed.

This effect can well be seen in Fig. 4.16a. Here, the intensity in a slice through the needle array is plotted versus time. The source has its maximum at 0 fs. Note that the dark horizontal stripes in the needle region are the positions of those cylinders that are located in the slice by incidence. As discussed earlier, the field is low in the needles and high at interfaces right outside a needle.

At very early times, a light-cone can be seen: the light generated at the source in the center travels outwards up and down in Fig. 4.16a and forward in time (from left to right) and eventually enters the vacuum region. The opening angle of this cone directly related to the speed of light. The opening angle is slightly smaller in the needle region which can be attributed to an effective reflective index of a ZnO-vacuum meta-material. The effective permittivity for a meta-material consisting of vertically aligned cylinders is calculated in Appendix A.1. The electromagnetic field traverses the needle region at velocities with an upper limit given by the speed of light in the meta-material.

After the source has decayed at approximately 30 fs, a (sub-) exponential decay can be observed. Here the highest intensities are still found in the needle region. At even later times of around 130 fs, the intensity is almost exclusively concentrated near the center of the needle region. This observation also fits well with the interpretation that there are long living modes that are mostly localized in the needle array and have few overlap with the vacuum region.

Furthermore, the findings presented in Fig. 4.16a can also exclude some alternative interpretations. First, it is not the case that the pulse is traveling out of the needle region as a whole. In this case, one would see two distinct maxima traveling outwards along the surface of the light-cone. In the discussed figure, it can clearly be seen that a non-negligible fraction of light stays near the source: the light cone is filled. The intensity is quickly spread all over the needle region. This fits well with the interpretation that the pulse is completely dispersed due to multiple scattering events even after traveling through the needle array for a very short path.

A second interpretation that can be excluded is that the needle-region / vacuum interface acts as a reflector such that cavity modes of the whole needle region become excited. Such modes would show up as a time-independent patterns of regularly spaced nodes and anti-nodes. Since the central energy of the pulse corresponds to a vacuum

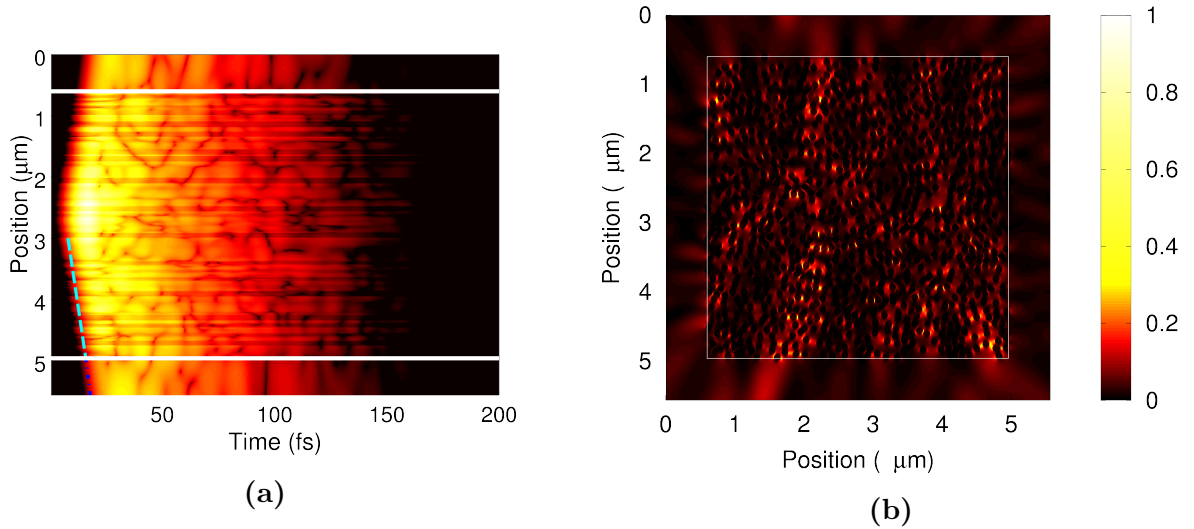


Figure 4.16: **(a)** Logarithmic intensity as color-scale plot along a slice through the needle-array versus time. The interface of needle covered and vacuum region is marked by white lines. The source at a position near the center of the needle-array has its maximum at 0 fs. The blue dash-dotted line has a slope of  $0.3 \frac{\mu\text{m}}{\text{fs}}$  and marks the vacuum speed of light, the cyan dashed line has a slope of  $0.3/\sqrt{1.472} \frac{\mu\text{m}}{\text{fs}}$ : the speed of light in an effective medium as calculated in App. A.1. **(b)** Intensity  $\|E\|^2$  versus position integrated over time after the main pulse has left the simulation area; from Ref. [2]

wavelength of 800 nm, there would typically be several nodes and anti-nodes on a slice of  $5 \mu\text{m}$ . Such characteristic patterns can not be seen in Fig. 4.16b.

Third, a purely diffusive transport process can be ruled out. In the diffusive case, the light-cone would also be filled because the speed of light would pose an upper limit but slower transport would also be allowed. However, one could not observe interference patterns in this case. In our case, there are intensity dips that form curly dark stripes in Fig. 4.16a. These stripes have a surprisingly long lifetime on the order of 25 fs and move very slow. They are a typical signature of destructive interference and of long-living coherences.

In conclusion, the intensity patterns observed in the present 2D calculations are best described by multiple scattering at the nano-needles. This way, some modes are formed that are localized in the nano-needle region and only have a small overlap with the vacuum region. These modes have surprisingly long lifetimes and form standing wave patterns. At some positions, the intensity is enhanced by constructive interference and forms distinct long-living intensity peaks. These peaks form very quickly at the time of the excitation pulse apex and thus have not only a high time-integrated intensity but also a very high overall intensity. In addition, there are extended modes that have a strong overlap with the vacuum region. These modes have a homogeneous intensity distribution

in the needle array such that they contribute to a background. Consequently, they are easily excited by a source in the needle region. The extended modes have a short lifetime such that at longer times after the excitation apex only the localized modes survive.

# Chapter 5

## Summary and Outlook

In the present work, recent research in three important topics in ultrafast nano-optics was presented by means of examples. Namely, these topics are the excitation and propagation of surface plasmon polaritons (SPPs), coupling of plasmons and excitons in non-linear materials and the localization of light by multiple scattering.

Each of these topics plays a major role in the development of future nano-optical devices. In particular, integrated all-optical nano-circuits are a candidate to replace or at least complement contemporary semiconductor microchips. The slow speed of the electrons and, even more important, the parasitic inductance and capacitance of high-frequency currents in nano-structured devices are a major challenge for the further development of electronic microchips. Today, we can observe that the operation frequency in semiconductor based microchips (that is acceleration of the electrons and eventually the electromagnetic radiation) has saturated. The clock-rate of a high-end computer was at around 4 *GHz* in the mid 2000s and is still at this value in the mid 2010s. In contrast, the clock-rate grew by 3 orders of magnitude from 1985 to 2005.

Today, advances in operation speed of semiconductor microchips are achieved by parallelization: many operations are performed in each cycle while the duration of an individual operation remains constant. However, the information transport (bandwidth) among the different operation units is limited and is the major bottleneck in modern computing.

A promising candidate to bring the next real breakthrough in computing (comparable to the invention of the integrated circuit) is computing with light.

For long-range information transport, light is already a well established information carrier. For on-chip applications, visible light is not very useful due to its comparably long wavelength and huge resulting structures. In contrast, SPPs are a promising candidate for optical information transport in microchips. An SPP is a collective excitation of light and the electron gas in a metal. Consequently, the light is confined to a metal-dielectric interface. The spatial extension of such an excitation is mostly limited by the size of

the metal-structure. This way, information can be carried along a plasmonic wave-guide with a size much smaller than the wavelength of the corresponding visible light. The SPP travels with (almost) the speed of light and inherits the weak interaction among photons. The absence of induction or capacity and the extremely high-frequency of light as the carrier wave allows for operation frequencies that are orders of magnitude higher than those of electric-current based systems.

The first topic discussed in the present work deals with the excitation of SPPs at a nano-structured metal surface. In order to communicate to peripherals, a plasmonic device has to couple SPPs to far-field light (e.g., an optical fiber). Metallic gratings are one realization of such a coupler. In the present work, the symmetry of the grating is incompatible with the symmetry of the individual nano-scatterers. Experiments in ZERULLA's group at UC Dublin show that the minima and maxima of some far-field reflection orders are shifted away from the most symmetric polarization.

In order to shed light on the origin of these shifts, the optical near fields were calculated. For this purpose, the three-dimensional fully coupled MAXWELL's equations were solved by the FDTD method. These calculations are challenging due to the high accuracy demand. Here we investigate a small polarization dependent shift in the SPP related reflectivity extremum in various refraction orders. In addition, the complicated, manifestly three-dimensional nano-structure along with the strong field gradients around the metal-air interface require a high spatial resolution. While the FDTD method allows to obtain a complete spectrum per calculation, it is still necessary to perform calculations for many angles of incidence and polarizations of the incident light.

With these calculations, it was possible to reproduce the experimental polarization shifts. In addition, it is found that there are shifts in some refraction orders while others remain unaffected. It was also found that the near field intensity always has its maximum at the most symmetric polarization. By trying various different geometries and sizes of the individual scatterers, it was found that the shifts depend on several aspects of the geometry. Thus, it could be ruled out that the suggestive values of  $30^\circ$  of the shift are directly related to the  $C_3$  symmetry and the special role of  $30^\circ$  angles therein.

From the calculated near fields, it could clearly be seen that the SPPs mostly travel along the flat metal in between the individual scatterers. On the one hand, this explains that the SPP propagation is almost unaffected by the broken symmetry. On the other hand, this implies that the coupling of SPPs to various far-field diffraction orders can be sensitively controlled by the choice of the geometry of the individual nano-scatterers. In particular multiple fibers in different angles of incidence (here: diffraction orders) could be coupled to the same SPP. In addition, the differences in the polarization dependence of various diffraction orders could be utilized to distinguish several signal channels on the same nano-antenna.

---

The second topic of the present work discusses the coupling of SPPs to excitons in an organic dye. Strong coupling to a non-linear material is another major step-stone in optical circuitry. In a combined optical-electronic microchip that uses SPPs for information transport, it would be desirable to perform at least simple operations on the purely optical side because opto-electronic coupling is a suspect bottleneck as any signal conversion. Such simple operations could be multiplexing and demultiplexing of signals as well as amplification and switching. For an all-optical microchip, an applicable (in contrast to simple) operation is obviously vitally important. To be precise, it has to be much faster (likely) or much cheaper (unlikely) than a corresponding electronic device. An example of such a device is an all-optical network switch: today optical fibers carry signals in and out and the logic inside is performed by electronics. Tomorrow, the logic could be performed by photonic devices.

The smallest building block of a logic gate is a three-port device where two signals go in and a result comes out. In linear optics, only one such operation is possible: linear superposition which is also the least useful operation. For any operation beyond that, a non-linear process is necessary. In the present work, the non-linear material is a  $j$ -aggregated organic dye. It is coupled to an SPP that is excited on a metal grating. It is known from experiments that SPPs and excitons can be strongly coupled and form new quasi-particles called excimons or plexcitons. A main experimental signature of strong coupling is that avoided crossing can be observed. This means that two resonances can clearly be distinguished for each value of the crossing parameter: the angle of incidence in this case. In particular, the line-width of the coupled modes is smaller than their RABI-splitting. In strong coupling there is coherent (phase conserving) energy transfer among SPP and exciton. In contrast, if the line-width is so broad that the resonances are washed out and cannot be distinguished, the lifetime of the modes is short and coherence is lost. For signal processing, coherence and consequently strong coupling is vital since information is lost otherwise.

In the system presented in this work, an SPP was tuned by the angle of incidence in experiments in LIENAU's group in Oldenburg. This way, the SPP was brought into or out-of resonance with the exciton at will. Two coupled SPP-exciton branches could clearly be observed in the far-field reflectivity. In the theoretical contributions of the author, the near fields were calculated by an FEM method in the frequency domain. On this purpose, a standard model for the metal and a multi-LORENTZian model for the dye was implemented. In order to reproduce the experimental findings, a detailed modeling of the grating geometry was necessary. Several parameters that were only approximately known from the experiment had to be determined by fitting procedures. Finally, the calculations reproduced the experimental far-field spectrum surprisingly well.

The experimental collaborators also performed a non-linear pump-probe experiment

where the dye was pumped by an off-resonant additional laser. It was found that the pump increasingly saturates the dye-exciton with increasing pump power. The saturation of the dye leads to a diminished coupling strength to the SPP. The SPP cannot excite excitons that already are in their excited state. In consequence, the splitting in the spectra becomes smaller and eventually vanishes at high pump powers.

Important aspects of this nonlinear process can be modeled from the inherently linear calculations presented in this work in a very simple way. By lowering the oscillator strength in the dye material model, the decrease and eventually vanishing of the splitting can be reproduced. An obvious extension of the calculation scheme is to express not only the oscillator strength but also its spectral position a function of the pump intensity. The parameters for such a material model could be obtained in a straightforward way from either the experiment or a steady state theory of the few-level quantum system. Calculations as those presented in the present work can be used to optimize the geometry in future active devices with plasmon-exciton coupling. The good consistency of calculations and experiment promises a good predictive quality for other geometry-material combinations. Particularly interesting nonlinear materials for future research are quantum dots[AB10, RDSF<sup>+</sup>10] and organic-inorganic hybrid semiconductors[PBP09]. Such systems combine the high quantum yield and simple processing of organic dyes with room temperature operation of semiconductors.

A very different geometry was considered in the third topic of the present work. In the first two parts regular arrays of scatterers were used to provide well-defined SPP modes. Here, randomly placed nano-scatterers are discussed. It is a highly surprising fact that modes with distinct spatial intensity maxima and well defined energy can be created by multiple scattering in many branches of wave-related physics. These modes are called *localized*. Localization by multiple scattering at randomly distributed scatterers was first discussed by P.W. ANDERSON for electronic waves in solid state physics. In this part, we seek for localized light modes in random arrays of vertically aligned ZnO nano-needles.

In fact strong intensity fluctuations are found in experiments with second-harmonic microscopy. Since the second harmonic signal is proportional to the squared fundamental intensity, this method is highly sensitive to near field intensity fluctuations. This means that in this random system, intensity is concentrated to few distinct hot-spots. In time resolved experiments, it was shown that the modes forming these hot-spots also have an extended lifetime. These findings match well with the interpretation that light is trapped in a certain position due to multiple scattering at the individual needles. A hand-waving description is that light bounces from needle to needle to form a two dimensional random walk. Surprisingly some light does not find the way out of the system but stays within some radius (localization length).

It is well known that localization of light is particularly hard to achieve. In order to



---

provide more evidence for the interpretation of the findings as localization of light, the author performed calculations on model systems to compare with the experiment. On this end, random distributions of dielectric cylinders were considered. The geometrical parameters such as needle diameter and needle density were inspired by available SEM images but also varied over a broad range. To calculate electromagnetic near fields, two main approaches were followed. First, two dimensional eigenmode expansions were calculated for super-cells containing hundreds of needles. Second, three dimensional FDTD calculations were performed to take the scattering into the third direction into account.

Both types of calculations unveil a combination of localized and delocalized modes that are found in the same energy region. The intensity statistics from the calculation and from the measured second-harmonic microscopy signal are quite comparable for similar geometry parameters. In particular, intensity histograms of both, experiment and calculation show asymmetric distributions with so called *fat tails* – very high intensities are surprisingly probable.

The similarity of these histograms is a main evidence for our interpretation of the peaks found in the experiment. Particularly, it can be excluded that the intensity peaks found in the experiment are induced by contamination of the sample, e.g., with dust particles or inhomogeneities in the needle distribution such as clustering of needles. Such contamination sites could also lead to intensity peaks but contribute to a normal (Gaussian) intensity distribution.

Localization of light or SPPs in disordered systems can be another ingredient in future nano-optical devices. The field enhancements in localization induced hot-spots along with nonlinear materials provide interesting effects while such systems are presumably cheap to produce in comparison to ordered systems. In addition, some disorder is always unavoidable in any device such that the understanding of localization might help to predict and circumvent unwanted effects.

For all topics discussed in the present work, the author provided theoretical calculations in close collaboration with experimental groups that reproduced important aspects of the experimental findings. Such calculations give insight to the dynamics of the electromagnetic near fields with spatial resolution of nano-meters and sub-femtosecond temporal resolution. This information is hardly available from experiments. Experimental techniques typically deliver either high temporal resolution (such as IFRAC) or high spatial resolution (such as PEEM). At the time of writing, these techniques are still in their development process and consequently inaccessible to most researchers due to high cost and complicated setup.

In contrast, electrodynamic calculations are widely available and the contemporary cost of computing power makes such calculations feasible even for complicated systems. However, some effort is necessary in order to use these tools to predict properties of

devices that do not yet physically exist. The predictive power of the calculations has to be proven by direct comparison of as many aspects as possible to experimental findings. This is exactly what the author did in the present work.

It was not only shown that electrodynamic calculations can reproduce experimental findings and consequently describe the physical reality. On the way, it was also gained experience in how to set up such calculations. One aspect is the choice of a suitable method since different methods give different types of answers that are nontrivial to convert into each other. This is closely related to the extraction of data: typically calculations give fields or eigenmodes whereas an actual device is better described by transmission coefficients quantifying the flow of signals through the device. Another aspect is the choice of boundary conditions that is at the very heart of solving partial differential equations. While an experimentalist typically imposes open boundaries by placing the device into a lab, the choice is much more difficult in a calculation. The combination of data extraction and choice of boundary conditions has implications on the kind of information obtained from the calculation. This choice can be compared to the complicated tricks that can be played with experimental techniques in order to suppress less important information or extract obfuscated information. Finally, material models have to be chosen that describe those aspects of the physics that actually contribute.

# Appendix A

## Derivations

### A.1 Effective Permittivity for Nano-Needle – Vacuum Mixtures

The effective indices were calculated analytically by a MAXWELL-GARNETT type of approach as proposed for spheres in Ref. [Sih01]. The idea is that the effective permittivity connects the average fields as  $\langle \mathbf{D} \rangle = \epsilon_{\text{eff}} \langle \mathbf{E} \rangle$ . With the volume fraction  $f$ , the averages are calculated by the self-evident formulas

$$\langle \mathbf{D} \rangle = f\epsilon \mathbf{E}_i + (1 - f)\epsilon_0 \mathbf{E}_e \quad (\text{A.1})$$

$$\langle \mathbf{E} \rangle = f\mathbf{E}_i + (1 - f)\mathbf{E}_e \quad (\text{A.2})$$

where  $\mathbf{E}_i$  and  $\epsilon$  are the field and permittivity in the inclusions and  $\mathbf{E}_e$ ,  $\epsilon_0$  are the respective values in the matrix. A less obvious ingredient is to take approximate fields in the inclusions from electrostatics. An electrostatic approximation is valid in the limit of inclusions that are very small compared to the wavelength. For infinite dielectric cylinders, one finds two different values for the s-polarization (where  $\mathbf{E}$  points along the cylinder axis) and the p-polarization (where  $\mathbf{E}$  is in the plane normal to the cylinders). By applying the boundary conditions for tangential and normal electric components one finds trivially for s-polarization (where  $\mathbf{E}$  has only one component: tangential):

$$E_i = E_e \quad (\text{A.3})$$

and after a tedious but straightforward calculation for the p-polarized case:

$$\mathbf{E}_i = \frac{2\epsilon_0}{\epsilon + \epsilon_0} \mathbf{E}_e . \quad (\text{A.4})$$

Putting these results into the averaging formulas A.1 + A.2 one finds the nice expressions

$$\epsilon_{\text{eff}}^{\text{s}} = f\epsilon + (1 - f)\epsilon_0 \quad (\text{A.5})$$

$$\epsilon_{\text{eff}}^{\text{p}} = \epsilon_0 \frac{(1 + f)\epsilon + (1 - f)\epsilon_0}{(1 - f)\epsilon + (1 + f)\epsilon_0} \quad (\text{A.6})$$

It can be seen from the band-structures discussed in Section 4.3.3 that this approximation works very well up to frequencies where multiple scattering becomes dominant. In Fig. 4.7a the calculated frequencies for both polarisations are scaled by the 2 different effective indices such that they match the trivial band-structure of a homogeneous medium within the numerical accuracy.

## A.2 Intensity Distributions

Intensity distributions obtained from experiments and calculations are often discussed in the literature on localization and in Chap. 4 of the present work. It is often argued that “unusual” intensity distributions and, more specific, distributions with sub-exponential tails at high intensities are manifestations of localization. In order to emphasize what is so special about such findings and to give a quantitative meaning to our diction we derive “usual” intensity distributions in this appendix.

In the literature, intensity distributions are often compared to the RAYLEIGH distribution[SG99, CSG00, HSP<sup>+</sup>08]. RAYLEIGH discussed the intensity distribution of random superpositions of sound waves very early[Ray80]. His theory can serve as standard for “usual”, non-localized waves. It is interesting to note that RAYLEIGH discusses the problem in terms of what is called a random walk nowadays. This point connects the problem of random superpositions of waves to transport by diffusion. For this reason, RAYLEIGH distributions are referred to as typical for diffusion in contrast to localization.

An intensity  $I(\mathbf{r})$  is calculated as the squared modulus of a (more fundamental) field. In electrodynamics in vacuum,  $I(\mathbf{r}) \propto \|\mathbf{E}(\mathbf{r})\|^2$  where  $\mathbf{E}$  is the electric field vector. In quantum mechanics in position-space representation  $I(\mathbf{r}) \propto \|\Psi(\mathbf{r})\|^2$ , with the complex valued wave-function  $\Psi$ , can be interpreted as the probability density to find a particle at  $\mathbf{r}$ . The rule to calculate the intensity can be generalized to

$$I = \sum_{n=1}^d x_n^2 \tag{A.7}$$

where the  $x_n$  are the components of the electric field vector or real and imaginary part of  $\Psi$ .

By saying “usual” we mean the following assumption: the  $x_n$  are independent normally distributed real random numbers with mean value  $\mu$  and variance  $\sigma^2$ . It is sufficient to discuss  $\mu = 0$  and  $\sigma = 1$  since other choices are related by a trivial substitution. Their joint probability density<sup>1</sup> is then

$$p(x_1, \dots, x_d) \sim e^{-\frac{1}{2} \sum_{n=1}^d x_n^2} . \tag{A.8}$$

---

<sup>1</sup>Normalization factors are left out in this section because they would obfuscate the important point: the shape of the functions. The symbol  $\sim$  is explicitly used in lines where a factor is dropped.

This assumption is the most naive guess a physicist may find for the problem of multiple scattering: the field at some point consists of a sum of retarded field contributions from many independent scattering events at different positions and times. Ignoring all the complications arising from polarization and coherence, the named distribution follows from the central limit theorem.

We may now calculate the distribution  $p_I(I = \sum_{n=1}^d x_n^2)$  of the intensity with the formula

$$p_I(I) = \int_{\mathbb{R}^d} p(x_1, \dots, x_d) \delta(I - \sum_{n=1}^d x_n^2) d^d x. \quad (\text{A.9})$$

Thanks to the special shape of the integrand, we can conveniently evaluate the integral in  $d$ -dimensional spherical coordinates

$$p_I(I) \sim \int_0^\infty e^{-\frac{r^2}{2}} \delta(I - r^2) r^{d-1} dr \quad (\text{A.10})$$

which evaluates to

$$p_I(I) \sim I^{\frac{d}{2}-1} e^{-I/2}. \quad (\text{A.11})$$

This is the family of chi-squared distributions including the PORTER-THOMAS distribution ( $d = 1$ ). All the distributions are governed by a power-law factor for small intensities and by an exponential decay for high intensities.

The distribution of amplitudes  $p_A(A)$  is

$$p_A(A) \sim \int_0^\infty e^{-\frac{r^2}{2}} \delta(A - r) r^{d-1} dr = A^{d-1} e^{-\frac{A^2}{2}} \quad (\text{A.12})$$

which is for  $d = 2$  the result given in Ref. [Ray80] and hence known as the RAYLEIGH distribution.

In logarithmic histograms such as those shown in Chap. 4, these intensity distributions look like

$$\ln(p_I(I)) = \left(\frac{d}{2} - 1\right) \ln I - I. \quad (\text{A.13})$$

Obviously, they show up as linearly decaying tail in such histograms. In contrast, intensity histograms of our localized systems show non-linearly and, in particular, slower decaying tails at high intensities.

Intensity distributions are often referred to as GAUSSIAN if vanishing skewness is to be emphasized even though intensities are purely positive numbers and can never actually be GAUSSIAN distributed.

## A.3 Surface Plasmon Polaritons

### A.3.1 Basics

To understand the SPP modes one can solve MAXWELL's Equations for an interface of a dielectric described by  $\epsilon(\omega)$  and a metal described by  $\epsilon'(\omega)$  and a conductivity  $\sigma(\omega)$ . Surface plasmon polaritons are solutions that travel along the metal-dielectric interface and, in particular, do not travel in the directions normal to the interface. The time-harmonic MAXWELL's Equations with the convention that the time-dependence of all fields and sources is given by the factor  $e^{-i\omega t}$  are

$$\nabla \times \mathbf{H}(\mathbf{r}, \omega) = -i\omega \mathbf{D}(\mathbf{r}, \omega) + \mathbf{j}(\mathbf{r}, \omega) \quad (\text{A.14})$$

$$\nabla \times \mathbf{E}(\mathbf{r}, \omega) = i\omega \mathbf{B}(\mathbf{r}, \omega) . \quad (\text{A.15})$$

One can replace  $\mathbf{D}$  and  $\mathbf{B}$  with the material equations and  $\mathbf{j}$  with OHM's law resulting in

$$\nabla \times \mathbf{H}(\mathbf{r}, \omega) = -i\omega \epsilon_0 \epsilon(\omega) \mathbf{E}(\mathbf{r}, \omega) + \sigma(\omega) \mathbf{E}(\mathbf{r}, \omega) \quad (\text{A.16})$$

$$\nabla \times \mathbf{E}(\mathbf{r}, \omega) = i\omega \mu_0 \mu(\omega) \mathbf{H}(\mathbf{r}, \omega) . \quad (\text{A.17})$$

The classic trick to obtain the HELMHOLTZ equation is to take the curl of the second equation and put the result into the first. We assume  $\nabla \mu = \mathbf{0}$  and  $\epsilon = \epsilon(\mathbf{r})$  to be piece-wise constant which is the case in all applications in the present work. This gives

$$\nabla(\nabla \cdot \mathbf{E}) - \Delta \mathbf{E} = (\omega^2 \mu_0 \mu \epsilon_0 \epsilon + i\sigma \omega \mu_0 \mu) \mathbf{E} \quad (\text{A.18})$$

$$= \frac{\omega^2}{c^2} n^2 \mathbf{E} \quad (\text{A.19})$$

introducing the vacuum speed of light  $c^2 = (\mu_0 \epsilon_0)^{-1}$ , the complex permittivity including the conductivity

$$\tilde{\epsilon} = \epsilon + i \frac{\sigma}{\omega \epsilon_0} \quad (\text{A.20})$$

and the complex refractive index  $n^2 = \mu \tilde{\epsilon}$ . In the absence of free charges, the divergence term vanishes in each area where  $\nabla \epsilon = \mathbf{0}$  and we have:

$$\left( \Delta + \frac{\omega^2}{c^2} n^2 \right) \mathbf{E} = 0 . \quad (\text{A.21})$$

Depending on the convention on the sign in the time-dependence ( $e^{-i\omega t}$  often used in physics or  $e^{i\omega t}$  often used in engineering) one obtains either a plus or a minus sign in Eq. A.20. This is important to note since one often wants to put a measured or modeled  $\tilde{\epsilon}(\omega)$  into computational MAXWELL solvers. Here, one has to study the solver documentation carefully. For example, there is a plus (as above) in FDTD Solutions[lum08] and a minus in COMSOL[com11].

Since we want to expand the fields into plane wave components, we put a plane wave traveling in  $\mathbf{k}$  direction and obtain the dispersion relation

$$k = n \frac{\omega}{c} . \quad (\text{A.22})$$

Now we assume a plane wave  $\mathbf{E}e^{i\mathbf{k}\cdot\mathbf{r}}$  in the dielectric and a wave in the metal  $\mathbf{E}'e^{i\mathbf{k}'\cdot\mathbf{r}}$ . We find that the continuity equations like  $\mathbf{n} \times (\mathbf{E}' - \mathbf{E}) = 0$  can only be fulfilled for all positions in the plane of the interface when the in-plane components of the wave-vectors are conserved, i.e.,  $\mathbf{k}_{\parallel} = \mathbf{k}'_{\parallel}$ .

We seek for waves traveling along the surface which means that  $\mathbf{k}_{\parallel}$  is mostly real. If we take a look at Eq. A.22 we see that  $k'$  is a complex number with a big imaginary part since  $n' \propto \sqrt{\Re(\epsilon') + i\Im(\epsilon')}$  where  $\Re(\epsilon')$  is a big negative number in a metal. Since the in-plane components of  $\mathbf{k}'$  are conserved,  $\mathbf{k}_{\perp}$  is mostly imaginary. Consequently the field is a wave traveling along the surface but exponentially decaying in the out-of plane direction into the metal. Such a field is often called an evanescent field. This is in well accordance with the experience that metals are non-transparent except for layers thinner than some decay-lengths.

First, we try to construct a s-polarized wave with these properties:

$$\begin{aligned} \mathbf{H} &= (H_x, 0, H_z) \exp(i(k_x x + k_z z)) \\ \mathbf{E} &= (0, E_y, 0) \exp(i(k_x x + k_z z)) . \end{aligned}$$

The boundary conditions for MAXWELL's equations [Jac06, Chap. I.5] state that tangential components of  $\mathbf{E}$  and  $\mathbf{H}$  are conserved along the interface, thus,  $E'_y = E_y$  and  $H'_x = H_x$  while the normal components of  $\mathbf{D}$  and  $\mathbf{B}$  are conserved. Here, we obtain  $\mu H_z = \mu' H'_z$ . If, as presumed,  $\mu' = \mu$ ,  $H_z = H'_z$ . From the divergence freedom  $\nabla \cdot \mathbf{B} = 0$ , we find  $H_x = -\frac{k_z}{k_x} H_z = -\frac{k'_z}{k_x} H'_z$  completing a  $2 \times 2$  linear system of equations:

$$\begin{pmatrix} 1 & -1 \\ k_z & -k'_z \end{pmatrix} \cdot \begin{pmatrix} H_z \\ H'_z \end{pmatrix} = \mathbf{0} . \quad (\text{A.23})$$

This system has non-vanishing solutions if its determinant is zero, i.e.,  $k_z = k'_z$ . This is in contradiction with MAXWELL's Equations since Eq. A.22 states that  $k$  depends on  $\epsilon$ . In order to fulfill  $\hbar\mathbf{k}_{\parallel}$  momentum conservation this dependency has to be exclusively in  $k_z$ . Consequently, we find no plasmon mode in the s-polarization.

In the p-polarization, we have the magnetic field  $\mathbf{H} = (0, H_y, 0) \exp(i(k_x x + k_z z))$  and the electric field  $\mathbf{E} = (E_x, 0, E_z) \exp(i(k_x x + k_z z))$  and obtain  $H_y = H'_y$ ,  $E_x = E'_x$  and  $\epsilon E_z = \epsilon' E'_z$ . From the divergence freedom  $\nabla \cdot \mathbf{D} = 0$  we can find  $E_x = -\frac{k_z}{k_x} E_z = -\frac{k'_z}{k_x} E'_z$ . Thus, we have a homogeneous linear system

$$\begin{pmatrix} \epsilon & -\epsilon' \\ k_z & -k'_z \end{pmatrix} \cdot \begin{pmatrix} E_z \\ E'_z \end{pmatrix} = \mathbf{0} . \quad (\text{A.24})$$

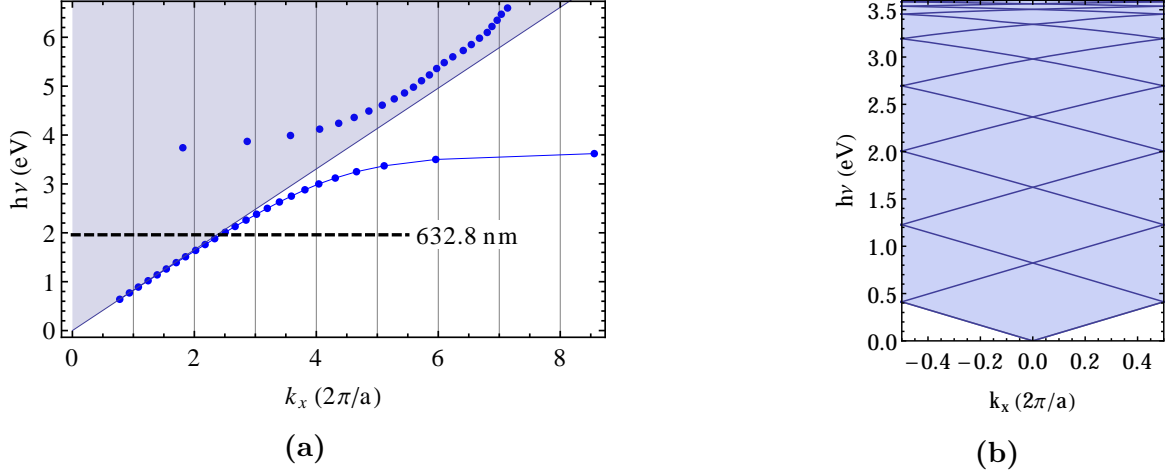


Figure A.1: **(a)** Dispersion Eq. A.25 plotted for a silver-vacuum interface (blue dots). The dispersion clearly shows two branches: the lower one with the SPPs and one for higher energy where volume-plasmons can be excited. The shaded area marks the light-cone, i.e., the area where propagating light can fulfill the vacuum dispersion relation. There are no points of the SPP branch in the light-cone – SPPs on flat metal interfaces can not be excited with propagating light. **(b)** SPP branch folded into the irreducible BRILLOUIN zone for a grating with a lattice-constant  $a = 1.5 \mu\text{m}$ . On a grating, many modes fall in the light-cone (shaded) and can be excited at matching angle-of-incidence – energy pairs.

Its determinant is zero if  $-\epsilon k'_z + \epsilon' k_z = 0$ . Using this together with Eq. A.22 and expressing all components of the wave-vector in terms of the in-plane momentum with the help of  $k'_z = \sqrt{\frac{\omega^2}{c^2} n'^2 - k_x^2}$ , one obtains the plasmon dispersion relation

$$k_x = \sqrt{\frac{\omega^2}{c^2} \mu \frac{\epsilon \epsilon'}{\epsilon + \epsilon'}}. \quad (\text{A.25})$$

Note that only the squared values of  $k_i$  enter the dispersion relation Eq. A.22. This means that the physics presented on this page is invariant if square roots are replaced by negative square roots. In case of Eq. A.25 this has the nice consequence that all physics is mirror symmetric, i.e., invariant under  $x \rightarrow -x$  transformations, which is what one has to expect from the global symmetry of the system.

For the  $\hat{z}$  direction, the signs of the  $k_z$  have no such freedom since  $\epsilon k'_z = \epsilon' k_z$  from the determinant condition above. In particular, if  $\epsilon'$  is that of a metal, its real part is negative and quite large (see, e.g., Fig. 2.5a). If  $\epsilon$  is a usual dielectric, it has a smaller positive real part. Thus, the imaginary parts of  $k_z$  and  $k'_z$  have opposite signs, meaning that the fields decay in opposite directions away from the interface. Also, their magnitude is different such that the decay length in the metal is smaller than the decay length in the dielectric.



### A.3.2 Excitation of SPPs with gratings

The dispersion relation can conveniently be plotted in energy versus in-plane momentum plots such as Fig. A.1a. From such plots, we can see under which circumstances SPPs can be excited. If we have, e.g., a He-Ne laser and a flat metal sample, we can investigate modes along the dashed line in the shaded region. With a given non-tunable laser, we are restricted to a given energy but can change the in-plane momentum  $k_x = \frac{\omega}{c} \sin \theta$  by changing the angle of incidence  $\theta$ . At normal incidence, the in-plane momentum is zero, at grazing incidence it is  $\frac{\omega}{c}$ . Higher values can not be achieved with in this setup. For this reason, the shaded area is often called the light-cone: it is the region in  $\mathbf{k}$  space where propagating light modes exist.

A grating can provide additional in-plane momentum. It is known from solid-state physics that BLOCH waves differing by a integer multiple of a reciprocal lattice vector (here  $G_x = \frac{2\pi}{a}$ ) are identical. For this reason, all the modes in a periodic system can be discussed in the first irreducible BRILLOUIN zone (here from  $k_x = -\frac{\pi}{a}$  to  $k_x = \frac{\pi}{a}$ ). Modes with higher  $k_x$  are folded back as shown in Fig. A.1b. Now, many SPP modes fall into the light cone and can eventually be excited by propagating light.

This method to overcome the momentum mismatch was used in the systems discussed in Chap. 2 and 3.

# Appendix B

## Bibliography

### B.1 References - own publications

- [1] D. Leipold, S. Schwieger, B. Ashall, D. Zerulla, and E. Runge, *Surface plasmon polaritons on square-lattice arrays of three-fold symmetric nanostructures*. Photonics and Nanostructures - Fundamentals and Applications **8**(4), 297 (2010).
- [2] D. Leipold, M. Silies, M. Mascheck, C. Lienau, and E. Runge, *Ultrafast dynamics of localized light modes*. Annalen der Physik Special Issue “Ultrafast Phenomena at the Nanoscale” **525**, 199 (2013).
- [3] M. Mascheck, S. Schmidt, M. Silies, T. Yatsui, K. Kitamura, M. Ohtsu, D. Leipold, E. Runge, and C. Lienau, *Observing the localization of light in space and time by ultrafast second-harmonic microscopy*. Nature Photonics **6**, 293 (2012).
- [4] S. Schwieger, D. Leipold, B. Ashall, M. Berndt, D. Zerulla, and E. Runge, *Surface plasmon polaritons on arrays of nanostructures with three-fold symmetry*. AIP Conference Proceedings **1176**(1), 81 (2009).
- [5] P. Vasa, R. Pomraenke, G. Cirmi, E. De Re, W. Wang, S. Schwieger, D. Leipold, E. Runge, G. Cerullo, and C. Lienau, *Ultrafast Manipulation of Strong Coupling in Metal-Molecular Aggregate Hybrid Nanostructures*. ACS NANO **4**(12), 7559 (2010).
- [6] P. Vasa, R. Pomraenke, G. Cirmi, E. De Re, W. Wang, S. Schwieger, D. Leipold, E. Runge, G. Cerullo, and C. Lienau, *Ultrafast manipulation of the Rabi splitting in metal-molecular aggregate hybrid nanostructures*. physica status solidi (c) **8**(4), 1113 (2011).
- [7] A. Williamson, Éadaoin McClean, D. Leipold, D. Zerulla, and E. Runge, *The design of efficient surface-plasmon-enhanced ultra-thin polymer-based solar cells*. Applied Physics Letters **99**(9), 093307 (2011).

## B.2 References - other publications

- [AALR79] E. Abrahams, P. W. Anderson, D. C. Licciardello, and T. V. Ramakrishnan, *Scaling Theory of Localization: Absence of Quantum Diffusion in Two Dimensions*. Phys. Rev. Lett. **42**, 673 (1979).
- [AB10] R. D. Artuso and G. W. Bryant, *Strongly coupled quantum dot-metal nanoparticle systems: Exciton-induced transparency, discontinuous response, and suppression as driven quantum oscillator effects*. Phys. Rev. B **82**, 195419 (2010).
- [ABB<sup>+</sup>99] E. Anderson, Z. Bai, C. Bischof, S. Blackford, J. Demmel, J. Dongarra, J. Du Croz, A. Greenbaum, S. Hammarling, A. McKenney, and D. Sorensen, *LAPACK Users' Guide* (Society for Industrial and Applied Mathematics, Philadelphia, PA, 1999), 3rd edn..
- [ABC<sup>+</sup>12] M. Aeschlimann, T. Brixner, S. Cunovic, A. Fischer, P. Melchior, W. Pfeiffer, M. Rohmer, C. Schneider, C. Strüber, P. Tuchscherer, and D. Voronine, *Nano-Optical Control of Hot-Spot Field Superenhancement on a Corrugated Silver Surface*. IEE J. Sel. Topics Quantum Electron. **18**(1), 275 (2012).
- [ABZ07] B. Ashall, M. Berndt, and D. Zerulla, *Tailoring surface plasmon polariton propagation via specific symmetry properties of nanostructures*. Appl. Phys. Lett. **91**(20), 203109 (2007).
- [AM07] N. W. Ashcroft and D. N. Mermin, *Festkörperphysik* (Oldenbourg Verlag München Wien, 2007), 3rd edn..
- [And58] P. W. Anderson, *Absence of Diffusion in Certain Random Lattices*. Phys. Rev. **109**, 1492 (1958).
- [Aue11] S. Auer, *Coupled exciton-plasmon modes in metal-dye hybrid systems*. Bachelorarbeit, Technische Universität Ilmenau (2011).
- [AVBZ09] B. Ashall, B. Vohnsen, M. Berndt, and D. Zerulla, *Controlling polarization twisting of light resulting from surface plasmon interactions with threefold symmetric nanostructures*. Phys. Rev. B **80**, 245413 (2009).
- [BDE03] W. L. Barnes, A. Dereux, and T. W. Ebbesen, *Surface plasmon subwavelength optics*. Nature **424**, 824 (2003).
- [Ber94] J.-P. Berenger, *A perfectly matched layer for the absorption of electromagnetic waves*. J. Comput. Phys. **114**(2), 185 (1994).

## BIBLIOGRAPHY

---

- [Ber09] P. Berini, *Long-range surface plasmon polaritons*. Adv. Opt. Photon. **1**(3), 484 (2009).
- [BH98] C. Bohren and D. Huffman, *Absorption and scattering of light by small particles* (John Wiley & Sons, 1998).
- [BKN11] K. Busch, M. König, and J. Niegemann, *Discontinuous Galerkin methods in nanophotonics*. Laser Photon. Rev. **5**(6), 773 (2011).
- [BSMM01] I. Bronstein, K. Semendjajew, G. Musiol, and H. Mühlig, *Taschenbuch der Mathematik* (Verlag Harry Deutsch, 2001), 5th edn..
- [CF08] C. Conti and A. Fratalocchi, *Dynamic light diffusion, three-dimensional Anderson localization and lasing in inverted opals*. Nature Phys. **4**, 794 (2008).
- [com08] *Comsol Multiphysics Users Guide* (COMSOL AB, 2008), 3rd edn..
- [com11] *RF Module User's Guide* (COMSOL, 2011), 4th edn..
- [CSG00] A. Chabanov, M. Stoytchev, and A. Genack, *Statistical signatures of photon localization*. Nature **404**, 850 (2000).
- [CZH<sup>+</sup>99] H. Cao, Y. Zhao, S. Ho, E. Seelig, Q. Wang, and R. Chang, *Random Laser Action in Semiconductor Powder*. Phys. Rev. Lett. **82**, 2278 (1999).
- [DAS<sup>+</sup>91] R. Dalichaouch, J. Armstrong, S. Schultz, P. Platzmann, and S. McCall, *Microwave localization by two-dimensional random scattering*. Nature **354**, 53 (1991).
- [Dro05] R. Dronskowski, *Computational Chemistry of Solid State Materials* (Wiley-VCH, 2005).
- [ELG<sup>+</sup>98] T. Ebbesen, H. Lezec, H. Ghaemi, T. Thio, and P. Wolff, *Extraordinary optical transmission through sub-wavelength hole arrays*. Nature **391**, 667 (1998).
- [EMR90] G. Engeln-Müllges and F. Reutter, *Formelsammlung zur numerischen Mathematik mit C-Programmen* (BI Wissenschaftsverlag, 1990).
- [FDS<sup>+</sup>09] J. Fallert, R. Dietz, J. Sartor, D. Schneider, C. Klingshirn, and H. Kalt, *Co-existence of strongly and weakly localized random laser modes*. Nature Photon. **3**, 279 (2009).

- 
- [FSP<sup>+</sup>09] S. Faez, A. Strybulevych, J. H. Page, A. Lagendijk, and B. A. van Tiggelen, *Observation of Multifractality in Anderson Localization of Ultrasound*. Phys. Rev. Lett. **103**, 155703 (2009).
- [Gan05] V. Gantmakher, *Electrons and Disorder in Solids* (Oxford University Press, 2005).
- [GE07] C. Genet and T. Ebbesen, *Light in tiny holes*. Nature **445**, 39 (2007).
- [GM12] R. Gross and A. Marx, *Festkörperphysik* (Oldenbourg Wissenschaftsverlag, 2012).
- [GMDL10] M. C. Gather, K. Meerholz, N. Danz, and K. Leosson, *Net optical gain in a plasmonic waveguide embedded in a fluorescent polymer*. Nature Photon. **4**, 457 (2010).
- [GWP79] N. Giordano, W. Wilson, and D. Prober, *Experimental study of Anderson localization in thin wires*. Phys. Rev. Lett. **725** (1979).
- [hdf10] The HDF Group, *Hierarchical data format version 5* (2010), <http://www.hdfgroup.org/HDF5>.
- [Hec09] E. Hecht, *Optik* (Oldenbourg Verlag München, 2009), 5th edn..
- [Her88] H. Hertz, *Ueber elektrodynamische Wellen im Luftraume und deren Reflexion*. Wiedemanns Ann. **34**, 610 (1888).
- [HL11] M. Hilbert and P. López, *The World's Technological Capacity to Store, Communicate, and Compute Information*. science **322**, 60 (2011).
- [HMF<sup>+</sup>01] M. H. Huang, S. Mao, H. Feick, H. Yan, Y. Wu, H. Kind, E. Weber, R. Russo, and P. Yang, *Room-Temperature Ultraviolet Nanowire Nanolasers*. Science **292**(5523), 1897 (2001).
- [HSP<sup>+</sup>08] H. Hu, A. Strybulevych, J. H. Page, S. E. Skipetrov, and B. A. van Tiggelen, *Localization of ultrasound in a three-dimensional elastic network*. Nature Phys. **4**, 945 (2008).
- [HW08] J. S. Hesthaven and T. Warbuton, *Nodal Discontinuous Galerkin Methods*. Texts in Applied Mathematics (Springer, 2008).
- [IR60] A. Ioffe and A. Regel, *Non-crystalline, amorphous, and liquid electronic semiconductors*. Prog. Semiconduct. **4**, 237 (1960).
- [Jac06] J. D. Jackson, *Klassische Elektrodynamik* (de Gruyter, 2006), 4th edn..

## BIBLIOGRAPHY

---

- [JC72] P. B. Johnson and R. W. Christy, *Optical Constants of the Noble Metals*. Phys. Rev. B **6**, 4370 (1972).
- [JJ01] S. G. Johnson and J. D. Joannopoulos, *Block-iterative frequency-domain methods for Maxwell's equations in a plane-wave basis*. Opt. Express **8**(3), 173 (2001).
- [JJWM08] J. D. Joannopoulos, S. G. Johnson, J. N. Winn, and R. D. Meade, *Photonic Crystals – molding the flow of light* (Princeton University Press, 2008), 2nd edn..
- [Joh13] S. G. Johnson, *MPB User Reference*. [http://ab-initio.mit.edu/wiki/index.php/MPB\\_User\\_Reference](http://ab-initio.mit.edu/wiki/index.php/MPB_User_Reference) (2013), accessed: 03/21/2013.
- [JVF97] J. D. Joannopoulos, P. R. Villeneuve, and S. Fan, *Photonic crystals: putting a new twist on light*. Nature **368**, 143 (1997).
- [KWH11] S. Kalusniak, H. Wünsche, and F. Henneberger, *Random Semiconductor Lasers: Scattered versus Fabry-Perot Feedback*. Phys. Rev. Lett. **106**, 013901 (2011).
- [KYOY08] K. Kitamura, T. Yatsui, M. Ohtsu, and G.-C. Yi, *Fabrication of vertically aligned ultrafine ZnO nanorods using metal-organic vapor phase epitaxy with a two-temperature growth method*. Nanotechnology **19**, 175305 (2008).
- [LGP88] I. Lifshits, S. Gredeskul, and L. Pastur, *Introduction to the theory of disordered systems* (John Wiley & Sons, 1988).
- [LLS<sup>+</sup>07] D. Laurent, O. Legrand, P. Sebbah, C. Vanneste, and F. Mortessagne, *Localized Modes in a Finite-Size Open Disordered Microwave Cavity*. Phys. Rev. Lett. **99**, 253902 (2007).
- [LSY09] R. B. Lehoucq, D. C. Sorensen, and C. Yang, *Arpack User's Guide: Solution of Large-Scale Eigenvalue Problems With Implicitly Restarted Arnoldi Methods (Software, Environments, Tools)* (Soc for Industrial & Applied Math, 2009).
- [lum08] *FDTD Solutions user's manual* (Lumerical Solutions, Inc, 2008), 6th edn..
- [Mai07] S. Maier, *Plasmonics: Fundamentals and Applications* (Springer, 2007).
- [Man01] V. Mandelshtam, *FDM: the filter diagonalization method for data processing in NMR experiments*. Prog. Nucl. Mag. Res. Sp. **38**, 159 (2001).

- 
- [Man03] V. Mandelshtam, *On harmonic inversion of cross-correlation functions by the filter diagonalization method*. J. Theor. Comput. Chem. **2**, 497 (2003).
- [mat10] *Mathematica* (Wolfram Research, Inc., 2010), 8th edn..
- [Mil64] R. C. Miller, *Optical second harmonic generation in piezoelectric crystals*. Appl. Phys. Lett. **5**, 17 (1964).
- [Mir00] A. D. Mirlin, *Statistics of energy levels and eigenfunctions in disordered systems*. Phys. Rep. **326**(5–6), 259 (2000).
- [MT97] V. Mandelshtam and H. Taylor, *Harmonic inversion of time signals*. J. Chem. Phys. **107**, 6756 (1997), see also erratum, *Ibid.* **109**, 4128 (1998).
- [NE97] S. Nie and S. R. Emory, *Probing Single Molecules and Single Nanoparticles by Surface-Enhanced Raman Scattering*. Science **275**(5303), 1102 (1997).
- [ORI<sup>+</sup>10] A. F. Oskooi, D. Roundy, M. Ibanescu, P. Bermel, J. D. Joannopoulos, and S. G. Johnson, *MEEP: A flexible free-software package for electromagnetic simulations by the FDTD method*. Comput. Phys. Commun. **181**, 687 (2010).
- [Pal85] E. Palik, *Handbook of optical constants of solids* (Academic Press, 1985).
- [PBP09] K. Pradeesh, J. Baumberg, and G. Prakash, *In situ intercalation strategies for device-quality hybrid inorganic-organic self-assembled quantum wells*. Appl. Phys. Lett. **95**(3), 033309 (2009).
- [Rae88] H. Raether, *Surface plasmons : on smooth and rough surfaces and on gratings* (Springer, Berlin [u.a.], 1988).
- [Ray80] L. Rayleigh, *On the resultant of a large number of vibrations of the same pitch and of arbitrary phase*. Phil. Mag. S. 5 **10**(60), 73 (1880).
- [RDSF<sup>+</sup>10] A. Ridolfo, O. Di Stefano, N. Fina, R. Saija, and S. Savasta, *Quantum Plasmonics with Quantum Dot-Metal Nanoparticle Molecules: Influence of the Fano Effect on Photon Statistics*. Phys. Rev. Lett. **105**, 263601 (2010).
- [Rit57] R. H. Ritchie, *Plasma Losses by Fast Electrons in Thin Films*. Phys. Rev. **106**, 874 (1957).
- [RMP<sup>+</sup>83] T. F. Rosenbaum, R. F. Milligan, M. A. Paalanen, G. A. Thomas, R. N. Bhatt, and W. Lin, *Metal-insulator transition in a doped semiconductor*. Phys. Rev. B **27**, 7509 (1983).

## BIBLIOGRAPHY

---

- [RSE<sup>+</sup>09] C. Reinhardt, A. Seidel, A. B. Evlyukhin, W. Cheng, and B. N. Chichkov, *Mode-selective excitation of laser-written dielectric-loaded surface plasmon polariton waveguides*. J. Opt. Soc. Am. B **26**(12), B55 (2009).
- [RSL<sup>+</sup>04] J. P. Reithmaier, G. Sek, A. Löffler, C. Hofmann, S. Kuhn, S. Reitzenstein, L. V. Keldysh, V. D. Kulakovskii, T. L. Reinecke, and A. Forchel, *Strong coupling in a single quantum dot-semiconductor microcavity system*. Nature **432**(7014), 197 (2004).
- [Run01] E. Runge, *Optical Properties of Localized Excitons in Semiconductor Nanostructures*. Habilitationsschrift, Humboldt-Universität zu Berlin (2001).
- [Run03] E. Runge, *Excitons in Semiconductor Nanostructures*. vol. 57 of *Solid State Physics*, 149 – 305 (Academic Press, 2003).
- [SB09] T. Søndergaard and S. I. Bozhevolnyi, *Surface-plasmon polariton resonances in triangular-groove metal gratings*. Phys. Rev. B **80**, 195407 (2009).
- [SG99] M. Stoytchev and A. Genack, *Observations of non-Rayleigh statistics in the approach to photon localization*. Opt. Lett. **24**(4), 262 (1999).
- [She90] P. Sheng (editor), *Scattering and localization of classical waves in random media* (World Scientific, 1990).
- [Sih01] A. Sihvola, *Two main avenues leading to the Maxwell Garnett mixing rule*. J. Electromagnet. Wave **15**, 715 (2001).
- [SMS<sup>+</sup>10] S. Schmidt, M. Mascheck, M. Silies, T. Yatsui, K. Kitamura, M. Ohtsu, and C. Lienau, *Distinguishing between ultrafast optical harmonic generation and multi-photon-induced luminescence from ZnO thin films by frequency-resolved interferometric autocorrelation microscopy*. Opt. Express **18**(24), 25016 (2010).
- [SS05] G. Stibenz and G. Steinmeyer, *Interferometric frequency-resolved optical gating*. Opt. Express **13**(7), 2617 (2005).
- [Sto01] P. Stollmann, *Caught by Disorder* (Birkhäuser, 2001).
- [TH05] A. Taflove and S. C. Hagness, *Computational Electrodynamics - The finite-difference time-domain method* (Artech House, 2005).
- [Tho77] D. Thouless, *Maximum metallic resistance in thin wires*. Phys. Rev. Lett. **39**, 1167 (1977).



- [VGM<sup>+</sup>05] A. Vial, A.-S. Grimault, D. Macías, D. Barchiesi, and M. L. de la Chapelle, *Improved analytical fit of gold dispersion: Application to the modeling of extinction spectra with a finite-difference time-domain method*. Phys. Rev. B **71**, 085416 (2005).
- [VPS<sup>+</sup>08] P. Vasa, R. Pomraenke, S. Schwieger, Y. I. Mazur, V. Kunets, P. Srinivasan, E. Johnson, J. E. Kihm, D. S. Kim, E. Runge, G. Salamo, and C. Lienau, *Coherent Exciton-Surface-Plasmon-Polariton Interaction in Hybrid Metal-Semiconductor Nanostructures*. Phys. Rev. Lett. **101**, 116801 (2008).
- [VRPL09] P. Vasa, C. Ropers, R. Pomraenke, and C. Lienau, *Ultra-fast nano-optics*. Laser Photon. Rev. **3**(6), 483 (2009).
- [VS05] C. Vanneste and P. Sebbah, *Localized modes in random arrays of cylinders*. Phys. Rev. E **71**, 026612 (2005).
- [WBLR97] D. S. Wiersma, P. Bartolini, A. Lagendijk, and R. Righini, *Localization of light in a disordered medium*. Nature **390**, 671 (1997).
- [WKSM11] F. Würthner, T. E. Kaiser, and C. R. Saha-Möller, *J-Aggregates: From Serendipitous Discovery to Supramolecular Engineering of Functional Dye Materials*. Angew. Chem. Int. Ed. **50**(15), 3376 (2011).
- [WWB<sup>+</sup>13] G. Weick, C. Woollacott, W. L. Barnes, O. Hess, and E. Mariani, *Dirac-like Plasmons in Honeycomb Lattices of Metallic Nanoparticles*. Phys. Rev. Lett. **110**, 106801 (2013).
- [Yab87] E. Yablonovitch, *Inhibited Spontaneous Emission in Solid-State Physics and Electronics*. Phys. Rev. Lett. **58**, 2059 (1987).
- [Yab93] E. Yablonovitch, *Photonic band-gap structures*. J. Opt. Soc. Am. B **10**(2), 283 (1993).
- [Yee66] K. S. Yee, *Numerical solution of initial boundary value problems involving Maxwell's equations in isotropic media*. IEEE Trans. Antennas Propagat. (1966).
- [YSH<sup>+</sup>] T. Yoshie, A. Scherer, J. Hendrickson, G. Khitrova, H. M. Gibbs, G. Rupper, C. Ell, O. B. Shchekin, and D. G. Deppe, *Vacuum Rabi splitting with a single quantum dot in a photonic crystal nanocavity*. Nature **432**, 200.
- [ZDY<sup>+</sup>06] C. F. Zhang, Z. W. Dong, G. J. You, S. X. Qian, and H. Deng, *Multiphoton route to ZnO nanowire lasers*. Opt. Lett. **31**(22), 3345 (2006).

# Appendix C

## Acknowledgements

The present work was only possible thanks to the support of many colleagues.

I want to thank my supervisor Erich Runge for introducing me into the interesting area of ultrafast nano-optics and his continuous support and advice.

I thank Christoph Lienau, Martin Silies and Manfred Mascheck as well as Dominic Zerulla and Brian Ashall and all other collaborators for sharing their experimental data and for inspiring discussions.

I also thank my friends and family for their general support and their great patience.

Last but not least, I want to thank the DFG and its priority program 1391 for financial support.